UNSPLIT NUMERICAL SCHEMES FOR HYPERBOLIC SYSTEMS OF CONSERVATION LAWS WITH SOURCE TERMS

Thesis by
Miltiadis V. Papalexandris

In Partial Fulfillment of the Requirements
for the Degree of
Doctor of Philosophy

California Institute of Technology
Pasadena, California

1997
(Submitted May 9, 1997)

To my parents

Στους γονείς μου

Acknowledgements

I would like to thank my advisor, Professor Anthony Leonard, for his continuous guidance, support, and encouragement during my research. I am especially grateful for his patience and understanding, and for being ready to help me anytime I asked. Working with Prof. Leonard has been a joy and an honor.

I am grateful to Professor Paul Dimotakis for his support and insightful suggestions. Our discussions resulted to many significant improvements of this work. I would also like to express my gratitude towards Dr. Tasso Lappas, one of Prof. Leonard's former students, who has served as an inspiration for me. Tasso was the one to introduce me to the subject of hyperbolic conservation laws, and he continued to help me and support me as a teacher and as a friend throughout this work.

I would also like to thank Professor Shepherd for his suggestions and our discussions about detonation physics, Professor Meiron and Professor Colonius for their comments and suggestions, and Dr. Quirk for providing me with his adaptive gridding software.

Thanks are also due to my advisor's secretary, Jean Gill, and to all the staff of GALCIT for their assistance, especially Katie Gross.

This effort was sponsored by the Air Force Office of Scientific Research, under grants No. F49626-93-100338 and F49620-94-10353, whose support is gratefully acknowledged.

Abstract

In this thesis, a new method for the design of unsplit numerical schemes for hyperbolic systems of conservation laws with source terms is developed. Appropriate curves in space-time are introduced, along which the conservation equations decouple to the characteristic equations of the corresponding one-dimensional homogeneous system. The local geometry of these curves depends on the source terms and the spatial derivatives of the solution vector. Numerical integration of the characteristic equations is performed on these curves.

In the first chapter, a scalar conservation law with a stiff, nonlinear source term is studied using the proposed unsplit scheme. Various tests are made, and the results are compared with the ones obtained by conventional schemes. The effect of the stiffness of the source term is also examined.

In the second chapter, the scheme is extended to the one-dimensional, unsteady Euler equations for compressible, chemically-reacting flows. A numerical study of unstable detonations is performed. Detonations in the regime of low overdrive factors are also studied. The numerical simulations verify that the dynamics of the flow-field exhibit chaotic behavior in this regime.

The third chapter deals with the development and implementation of the unsplit scheme, for the two-dimensional, reactive Euler equations. In systems with more than two independent variables there are one-parameter families of curves, forming manifolds in space-time, along which the one-dimensional characteristic equations hold. The local geometry of these manifolds and their position relative to the classical characteristic rays are studied. These manifolds might be space-like or time-like, depending on the local flow gradients and the source terms.

In the fourth chapter a numerical study of two-dimensional detonations in performed. These flows are intrinsically unstable and produce very complicated patterns, such as cellular structures and vortex sheets. The proposed scheme appears to be capable of capturing many of the the important details of the flow-fields. Unlike traditional schemes, no explicit artificial-viscosity mechanisms need to be used with the proposed scheme.

Table of Contents

List of Figures

CHAPTER 1

Scalar Conservation Laws with Source Terms

A variety of efficient numerical schemes for hyperbolic systems of conservation laws has been developed in the recent past. These schemes evolved following the understanding of fundamental concepts from the theory of nonlinear hyperbolic PDE's, such as characteristic surfaces, existence, uniqueness, and solution of the Riemann problem, *etc.* See, for example, Courant & Hilbert (1963), Lax (1957), (1973), and Yee (1987) for an extensive review of the literature. The main field of application of these schemes was compressible, non-reacting flow.

Higher-order schemes, such as the ENO schemes, Harten *et al.* (1987), the MUSCL scheme, van Leer (1979), the PPM of Colella & Woodward (1984), and Roe's approximate Riemann solver, Roe (1981), can be viewed as extensions of Godunov's original scheme to second-order accuracy. These are achieved by making use of the theory of characteristics for systems of hyperbolic PDE's in one space dimension. They employ the characteristic decomposition of the equations into a set of scalar fields, locally (at each computational cell), to evaluate the flux terms at the cell interfaces. Discontinuous solutions can be computed by supplementing the characteristic equations with the appropriate jump relations, *i.e.*, by solving the corresponding Riemann problem.

The traditional approach for the extension of these schemes to equations with source terms is to use time-splitting, that is integration of the gas dynamic terms of the equations first, and integration of the appropriate ODE for the source term in an intermediate step. This decoupling can be done in an optimal way using Strang-type splitting, Strang (1968). Bounds for the $\mathcal{L}_1$ errors of splitting methods have been established for scalar conservation laws by Crandall & Majda (1980) for dimensional splitting in multi-dimensional homogeneous equations, and by Tang & Teng (1995) for time splitting in one-dimensional scalar laws with source terms. Nevertheless, this decoupling introduces numerical errors. The decomposition of

the equations into scalar fields is not straightforward, *i.e.*, the quantities known as Riemann invariants are now not constant along characteristic trajectories. This error can be significant in systems with multi-mode instabilities and multiplicity of spatial and temporal scales, such as the Euler equations for reacting flows.

An alternate approach was recently introduced by Lappas *et al.* (1995) who developed an unsplit MUSCL-type scheme for the two-dimensional compressible Euler equations. The equations of motion of a compressible, non-reacting fluid, along the characteristics in two and three space dimensions, are not homogeneous. They include a kinematic, source-like term that is proportional to the in-plane divergence of the velocity field, *i.e.*, the two-component divergence in the plane locally perpendicular to the classical characteristic. As a consequence, the classical characteristics do not serve as paths for Riemann invariants in more than one space dimension. In the analysis by Lappas *et al.*(1995), a general methodology is developed that defines manifolds in space-time, dubbed *Riemann Invariant Manifolds*, along which the equations are decomposed into the same scalar fields as in the one-dimensional case and solved numerically. These manifolds may appear to be space-like, or time-like, in the classical description, depending on the flow-velocity gradients, but embed the paths along which the characteristic equations apply (exactly).

In the present work, the work of Lappas *et al.* (1995) is extended to systems of hyperbolic conservation laws with source terms, such as compressible, reacting flows. This chapter deals with the development of these ideas for a scalar conservation law with a nonlinear source term. Extensive numerical experimentation has been conducted. The results are compared with approximate solutions, or exact solutions whenever possible. The role of the stiffness of the source term has also been examined.

1.1 General Formulation

Consider the following initial value problem for the scalar $u(x,t)$:

$$\frac{\partial}{\partial t}u + \frac{\partial}{\partial x}f(u) = g(u)\,, \qquad x \in [0,\infty)\,, \tag{1.1a}$$

$$u(x,0) = u_0(x) \in [0,1]\,. \tag{1.1b}$$

The corresponding homogeneous law is associated with a convex entropy pair, *i.e.*, the entropy function: $\phi(u)$, and the entropy flux: $\psi(u)$, satisfying

$$\psi_u = \phi_u f_u .$$

The entropy pair is subject to the following entropy condition:

$$\frac{\partial}{\partial t}\phi(u) + \frac{\partial}{\partial x}\psi(u) \leq 0 . \tag{1.2}$$

Furthermore, the source term $g(u)$ is assumed to satisfy

$$g(u) \in \mathcal{C}^2([0,1], \Re) , \tag{1.3a}$$

$$g(0) = g(1) = 0 . \tag{1.3b}$$

Let $\Omega = [0,\infty) \times [0,T]$. A bounded measurable function, $u(x,t)$, is a weak solution of (1.1) if $\forall \xi \in \mathcal{C}^1(\Omega)$ with compact support in $([0,\infty) \times [0,T))$

$$\int\int_{\Omega} (u\,\xi_t + f(u)\,\xi_x)\,\mathrm{d}x\,\mathrm{d}t + \int_0^{\infty} u_0(x)\,\xi(x,0)\,\mathrm{d}x = -\int\int_{\Omega} \xi\, g\,\mathrm{d}x\,\mathrm{d}t . \tag{1.4}$$

Existence and uniqueness of weak solutions for this problem was given by Kruzkov (1970). The source term $g(u)$ is constructed to possess two equilibrium values at $u = 0$ and $u = 1$. The large-time solution of the above initial value problem may approach one equilibrium value or another, depending on the nature of the source term. The decay estimates for the corresponding homogeneous law, Lax (1957), (1973), do not hold for the above problem.

The characteristic decomposition of the problem yields:

$$\frac{\mathrm{d}u}{\mathrm{d}t} = g(u) , \qquad \text{along} \qquad \frac{\mathrm{d}x}{\mathrm{d}t} = f_u . \tag{1.5}$$

Motivated by the fact that for the corresponding homogeneous law, u remains constant along characteristics, someone could ask the question: Along which curve in space-time does u remain constant? The answer is that, at smooth parts of the flow,

$$\frac{\mathrm{d}u}{\mathrm{d}t} = 0 , \qquad \text{along} \qquad \frac{\mathrm{d}x}{\mathrm{d}t} = f_u - \frac{g(u)}{\partial u/\partial x} . \tag{1.6}$$

The geometry of this curve depends locally on the spatial derivatives of the solution. These derivatives are known for any time the solution itself is known, *i.e.*, all the necessary elements to construct this curve in space-time are available, without extra cost.

1.2 Description of the Algorithm and Numerical Results

Consider the initial value problem formulated as above, for $f(u) = u^2/2$:

$$\frac{\partial}{\partial t}u + \frac{\partial}{\partial x}\left(\frac{u^2}{2}\right) = g(u)\,, \qquad x \in [0,\infty)\,, \tag{1.7a}$$

$$u(x,0) = u_0(x) \in [0,1]\,. \tag{1.7b}$$

A typical nonlinear term satisfying (1.3a) and (1.3b) is

$$g(u) = \frac{1}{\varepsilon}u(1-u)\,, \tag{1.8}$$

where ε is a coefficient measuring the stiffness of the system. An entropy pair associated with the corresponding homogeneous law is given by:

$$\phi(u) = u^2 \qquad \psi(u) = \frac{2}{3}u^3\,. \tag{1.9}$$

In the case where the source term is given by (1.8), and for smooth $u_0(x)$, the equation of the characteristic decomposition yields:

$$u(x,t) = u_0\,\frac{e^{t/\varepsilon}}{1+(e^{t/\varepsilon}-1)u_0}\,, \tag{1.10a}$$

along the curves

$$x = x_0 + \varepsilon\log\left[1+(e^{t/\varepsilon}-1)u_0\right]\,. \tag{1.10b}$$

Given this relation, one can deduce the following shock-formation criterion: For the initial value problem given by relations (1.7) and (1.8), a shock is formed if the following inequality is satisfied:

$$u_0(x) + \varepsilon u_0'(x) < 0\,, \qquad \text{for some } x\,, \tag{1.11}$$

where $u_0'(x)$ is the derivative of $u_0(x)$. The shock-formation time is given by:

$$t_{\text{s.f.}} = \varepsilon\log\left(\frac{A(x)-1}{A(x)}\right)\,; \qquad A(x) \equiv (u_0(x) + \varepsilon u_0'(x))_{\min}\,. \tag{1.12}$$

The equation of the constant-u curves is given by

$$\frac{\mathrm{d}x}{\mathrm{d}t} = u - \frac{g(u)}{\partial u/\partial x} \equiv v(x,t)\,. \tag{1.13}$$

The issue of the limiting case $\partial u/\partial x \to 0$ has to be addressed. First it should be noted that at the points in the (x,t)-plane where the spatial derivative of the solution approaches zero, there is no singularity of the equation. The curve defined by (1.13) becomes locally parallel to the $x-$axis at those points. Then, it can not be used for the computation of the fluxes at the interfaces. Additionally, a non-zero but very small value of u_x (it can occur, say, in the cells neighboring the one where $u_x = 0$) might lead to a large value of $v(x,t)$. Then a small time-step would be necessary when equation (1.13) is to be integrated numerically, to maintain the desired level of accuracy. For these isolated cases it would be better to find the fluxes at the interfaces by employing a Taylor expansion. In the following, it is shown how these ideas can be combined in a simple and uniform manner.

A similar phenomenon can occur in the application of shock-capturing schemes for the numerical solution of Hamilton-Jacobi type equations. A well-known example is the computation of moving fronts whose speed is curvature-dependent; see, Osher & Sethian (1988), and Sethian (1990). The equivalent situation there arises when the speed of the front is locally zero. No serious difficulties have been reported in the computations at these points.

The algorithm proposed for the numerical integration of the above problem belongs to the class of second-order accurate MUSCL-type schemes and is described below. Consider uniform spacing in the $x-$direction of length Δx and let u_j^n be the average of u in the j^{th}-cell at time $t = n\,\Delta t$, *i.e.*,

$$u_j^n \;=\; \frac{1}{\Delta x}\int_{(j-1/2)\Delta x}^{(j+1/2)\Delta x} u(x,\, n\,\Delta t)\;\mathrm{d}x\;. \tag{1.14}$$

Assume linear interpolation of $u(x,\, n\Delta t)$ in each cell:

$$u(x,\, n\Delta t) \;=\; u_j^n \;+\; (u_x)_j\, x\;, \qquad x \;\in\; \left[-\frac{\Delta x}{2}\;,\; \frac{\Delta x}{2}\right]\;. \tag{1.15}$$

The slope of $u(x,t)$ on each cell, $(u_x)_j$, can be computed using a standard TVD limiter. In the present algorithm, van Albada's limiter is chosen, van Leer (1984):

$$(u_x)_j \;=\; \mathrm{ave}(u_x^-\;,\; u_x^+)\;, \tag{1.16a}$$

where

$$u_x^- \;=\; \frac{u_j^n - u_{j-1}^n}{\Delta x}\;, \qquad u_x^+ \;=\; \frac{u_{j+1}^n - u_j^n}{\Delta x}\;, \tag{1.16b}$$

$$\text{ave}(a,b) \equiv \frac{a+b}{2}\left(1 - \frac{(a-b)^2}{a^2+b^2+c^2}\right), \tag{1.16c}$$

and c is a small number, ($c^2 \ll 1$).

The conservation law (1.7) is approximated by the following explicit finite-difference scheme:

$$u_j^{n+1} = u_j^n - \frac{\Delta t}{\Delta x}\left(\frac{(u_{j+1/2}^{n+1/2})^2}{2} - \frac{(u_{j-1/2}^{n+1/2})^2}{2}\right) + \frac{\Delta t}{2}\left(g\left(u_{j+1/2}^{n+1/2}\right) + g\left(u_{j-1/2}^{n+1/2}\right)\right). \tag{1.17}$$

In this relation $u_{j+1/2}^{n+1/2}$ denotes the value of u at the right interface of the j^{th}-cell at a time $t = (n+1/2)\,\Delta t$. It is evaluated by tracing the constant-u curve forward in time, as given by (1.13). This is done by locating the point x_p that lies on that curve and satisfies $u(x_p, n\Delta t) = u_{j+1/2}^{n+1/2}$:

$$\frac{\Delta x}{2} - x_p = \frac{\Delta t}{2}u(x_p, n\Delta t) - g(u(x_p, n\Delta t))\int_{n\Delta t}^{(n+1/2)\Delta t}\frac{\mathrm{d}t}{u_x}.$$

Assuming linear interpolation of both $u(x,t)$ and $g(u)$ at each cell, this relation gives:

$$\frac{\Delta x}{2} - x_p = \frac{\Delta t}{2}(u_j^n + (u_x)_j x_p) - \left(g(u_j^n) + g_u(u_j^n)\,(u_x)_j x_p\right)\int_{n\Delta t}^{(n+1/2)\Delta t}\frac{\mathrm{d}t}{u_x}. \tag{1.18}$$

The integral appearing on the right-hand side of (1.18) can be evaluated by the forward Euler method. Numerical experiments, however, showed that the accuracy of the algorithm can be improved by using a trapezoidal rule with the right end-point approximated by a Taylor series:

$$\int_{n\Delta t}^{(n+1/2)\Delta t}\frac{\mathrm{d}t}{u_x} = \frac{\Delta t}{2}h(u_j^n, (u_x)_j), \tag{1.19}$$

where

$$h(u_j^n, (u_x)_j) \equiv \frac{1}{2}\left(\frac{1}{(u_x)_j} + \frac{1}{(u_x)_j + \frac{\Delta t}{2}(u_{xt})_j}\right) \equiv \frac{\omega(u_j^n, (u_x)_j)}{(u_x)_j}, \tag{1.20}$$

and

$$(u_{xt})_j = (u_x)_j\left(g_u(u_j^n) - (u_x)_j\right). \tag{1.21}$$

Equation (1.19) must be supplemented with the appropriate jump relations that take care of discontinuities, *i.e.*, an appropriate Riemann problem has to be solved locally at the interface. The Riemann problem for the corresponding homogeneous law (inviscid Burgers equation) admits a self-similar solution, depending on x/t only; see, for example, Lax (1973). For the non-homogeneous conservation law, the Rankine-Hugoniot relation remains the same, but the rarefaction wave no longer admits a self-similar representation. As $x \to 0$ and $t \to 0$, the solution of the non-homogeneous case approaches the self-similar solution of the corresponding homogeneous problem.

Furthermore, the process of solving the discretized version of the ODE that holds along the curve (1.13) is sufficient, for locally smooth solutions, because it gives second-order accurate results. The solution of the Riemann problem has to be employed only if discontinuities are present. These discontinuities, however, are due to the convective terms of the conservation laws and not the source terms, hence the inclusion of the source terms gives just a higher-order correction (for a detailed discussion on this subject, see Pember (1993)). Therefore, the self-similar solution can be used for computational purposes without loss of accuracy. For the conservation law under consideration, and given the fact that $u(x,t) > 0$ (thus only shocks that propagate to the right are admissible), the numerical solution of the Riemann problem reduces to the following procedure.

Let u_L , u_R the solution at the left and right side of the j^{th} interface:

$$u_L = u_j^n + \frac{\Delta x}{2}(u_x)_j \,,$$

$$u_R = u_{j+1}^n - \frac{\Delta x}{2}(u_x)_{j+1} \,,$$

and let $\Delta u = u_R - u_L$. Let $u(x_p, n\Delta t)$ be the value evaluated by tracing the invariant curve (1.13) in time, as described earlier, and let $v(x_p, n\Delta t)$ be the tangent of (1.13) passing through $(x_p, n\Delta t)$. Then, $u_{j+1/2}^{n+1/2}$ is given by:

$$u_{j+1/2}^{n+1/2} = \begin{cases} u(x_p, n\Delta t) \,, & \text{for } v(x_p, n\Delta t) > 0 \,, \\ u(x_p, n\Delta t) - \Delta u \,, & \text{for } v(x_p, n\Delta t) < 0 \,. \end{cases} \tag{1.22}$$

As already mentioned, in the absence of discontinuities, this procedure gives:

$$u_{j+1/2}^{n+1/2} = u(x_p, n\Delta t) = u_j^n + \frac{\Delta t}{2} \frac{\left(\frac{\Delta x}{\Delta t} - u_j^n\right)(u_x)_j + g\left(u_j^n\right)\omega(u_j^n, (u_x)_j)}{1 + \frac{\Delta t}{2}(u_x)_j - \frac{\Delta t}{2} g_u\left(u_j^n\right)\omega(u_j^n, (u_x)_j)} \,. \tag{1.23}$$

At the limit $u_x \rightarrow 0$, the above relation has no singularity and it can be used even for this limiting case. The following expression, based on Taylor series expansion, could also be used:

$$u_{j+1/2}^{n+1/2} = u_j^n + \frac{\Delta x}{2}(u_x)_j + \frac{\Delta t}{2}(u_t)_j \,, \qquad (1.24),$$

(both expressions result in second-order accurate schemes). The fact that for this particular scalar conservation law Taylor series expansions are not necessary to avoid division by zero, can not be easily generalized to systems of equations.

Finally, it is worth mentioning that any interpolation procedure can be implemented with the algorithm, because the interpolation step is in principle independent of the nature (split or unsplit) of the scheme. This step, however, plays an important role in the accuracy of any shock-capturing method. This is more so in the present case, because efficiency and robustness of the scheme depend greatly on the accuracy with which the "invariant" curve (1.13) is known, and hence on the accuracy with which the spatial derivatives of the solution are approximated.

As a first test of the scheme, the source term given by (1.8) is considered, with ε set equal to unity. Initial and boundary conditions (IC's and BC's) are given by:

$$u_0(x) = \begin{cases} x(1-x)\,, & \text{for } x \leq 1\,, \\ 0\,, & \text{for } x > 1\,. \end{cases} \qquad (1.25)$$

and

$$u(0,t) = 0 \qquad u(\infty,t) = 0\,, \qquad \forall\, t\,. \qquad (1.26)$$

The results obtained for this problem are given in Fig. 1.1. For this test case, $CFL = 0.6$. A shock is formed at $t = 0.61803$. The value of u behind the shock increases because of the source term, until $u = 1$ which is a stable equilibrium value (the value $u = 0$ is an unstable one). From then on, the shock propagates with a speed $s = 0.5$. The evolution process is captured quite well by the present scheme.

As a second test, the initial conditions of the previous problem are changed to:

$$u_0(x) = \begin{cases} 1\,, & \text{for} \quad \Delta x < x \leq 1\,, \\ 0\,, & \text{for } x > 1\,, \text{ or} \quad 0 < x < \Delta x\,. \end{cases} \qquad (1.27)$$

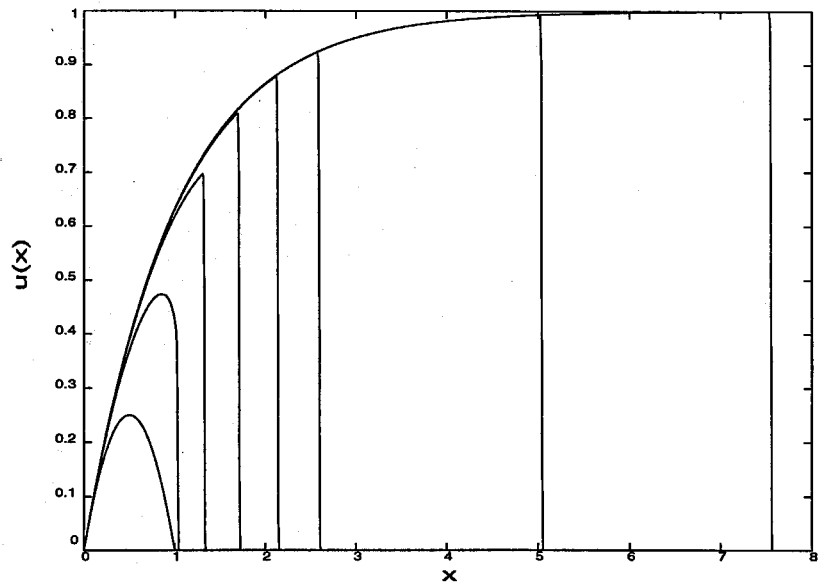

FIG.1.1 Spatial profiles for $g(u) = u(1-u)$, and IC's, and BC's given by (1.25) and (1.26) respectively. Profiles at $t = 0.0,\ 1.0,\ 2.0,\ 3.0,\ 4.0,\ 5.0,\ 10.0,\ 15.0$. $\Delta x = 0.02$.

Results for this problem are given in Fig. 1.2. For this test case, $CFL = 0.6$. The left discontinuity, initially located at $x = 1$, becomes a rarefaction wave. The head of this expansion, which is an "acoustic" disturbance, moves with characteristic speed $u_{\text{ch}} = 1.0$, while the tail stays at the origin because the characteristic speed there is zero. The right discontinuity moves with a shock speed $s = 0.5$. As soon as the head of the expansion reaches the shock, the shock starts to decay. This decay stops because the source term eventually restores the post-shock value at the upper equilibrium level.

Consider now the following Riemann problem:

$$u_0(x) = \begin{cases} 0\,, & \text{for } 0 \le x\,, \\ \\ 1\,, & \text{for } x > 0\,. \end{cases} \tag{1.28}$$

For this particular problem, relations (1.10a) and (1.10b) can be used to get the expression of the resulting rarefaction in closed form:

$$u(x,t) = \begin{cases} \dfrac{e^{t/\varepsilon}\left(e^{x/\varepsilon}-1\right)}{e^{x/\varepsilon}\left(e^{t/\varepsilon}-1\right)}\,, & \text{for } x \le t\,, \\ \\ 1\,, & \text{for } x > t\,. \end{cases} \tag{1.29}$$

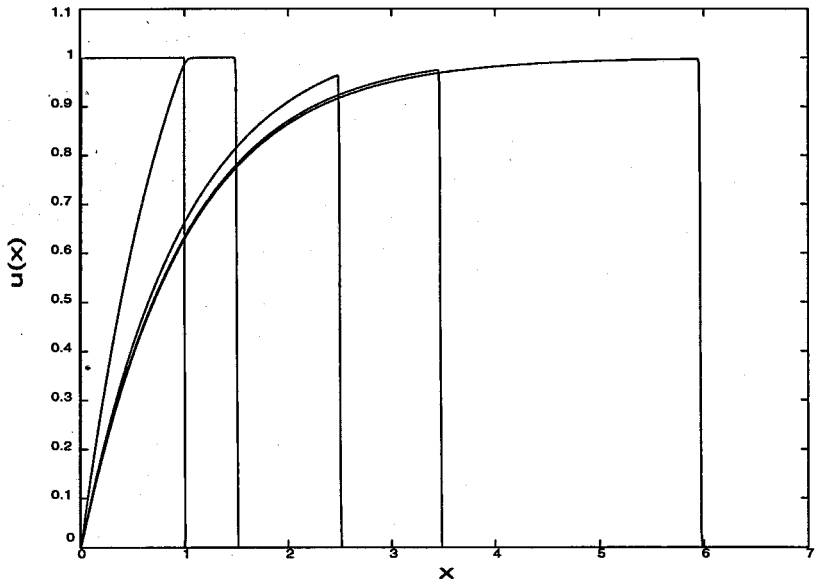

FIG.1.2 Spatial profiles for $g(u) = u(1-u)$, and BC's, and IC's given by (1.26) and (1.27) respectively. Profiles at $t = 0.0,\ 1.0,\ 3.0,\ 5.0,\ 10.0$. $\Delta x = 0.02$.

The computed rarefaction, as shown in Fig. 1.2 (and for times that the post-shock value is unity, so that u gets the equilibrium values at the endpoints of the rarefaction), are in excellent agreement with the above relation.

The same problem is also considered, but now the source term is given by

$$g(u) \;=\; -u\,(1-u)\,. \tag{1.30}$$

The only difference with the previous problem is in the sign of the source term. Because of this sign change the value $u = 1$ is unstable and the value $u = 0$ is stable. Expressions for the characteristics and the shock-formation criterion can also be derived for this case. Numerical results for this problem are shown in Fig. 1.3. Again, they are obtained with $CFL = 0.6$. It can be verified that the shock wave decays with a rate faster than $O(1/\sqrt{t})$, which is the decay rate for a shock wave in the corresponding homogeneous law.

The issue of the stiffness of the source term will now be discussed. Many authors have devoted attention to the numerical integration of hyperbolic PDE's with stiff source terms and the spurious solutions that might be obtained; see for example Colella *et al.* (1986), LeVeque & Yee (1990), Bourlioux (1991), Griffiths *et al.* (1992),

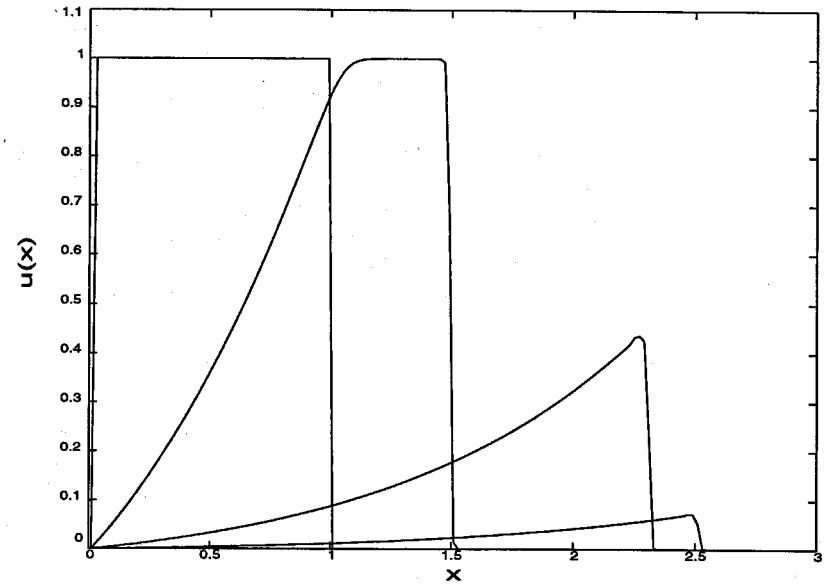

FIG.1.3 Spatial profiles for $g(u) = -u(1-u)$, and BC's, and IC's given by (1.26) and (1.27) respectively. Profiles at $t = 0.0,\ 1.0,\ 3.0,\ 5.0$. $\Delta x = 0.02$.

and Pember (1993). Even though shock-capturing schemes are stable in stiff cases, coarse spatial resolution may give incorrect propagation speeds of discontinuities. This is because the source terms are activated throughout the region occupied by the smeared shock, in a non-physical manner. The result is a spurious shock speed, usually of one cell per time-step for coarse resolutions. It is also acknowledged, Bourlioux (1991), that finer temporal resolutions produce shock speeds of one cell per $2-3$ time-steps. Pember (1993) also pointed that out, and he additionally conjectured a criterion for the non-appearance of spurious solutions by implicit schemes for dissipative 2×2 systems. The criterion is the commutability of the vanishing viscosity limit for viscous regularizations of (1.7), and the limit of infinite stiffness. Chen *et al.* (1994) proved that this commutability holds for such systems.

In the present numerical investigations, the focus is on the scalar law given by (1.7) and (1.8). The proposed scheme is compared with its equivalent split scheme, that is

$$u^{n+1} = \mathcal{L}_S^{(\Delta t/2)}\, \mathcal{L}_F^{(\Delta t)}\, \mathcal{L}_S^{(\Delta t/2)}\, (u^n)\,. \tag{1.31}$$

Here, $\mathcal{L}_F$ is the numerical solution operator for the corresponding homogeneous

conservation law

$$\frac{\partial u}{\partial t} + \frac{\partial}{\partial x}\left(\frac{u^2}{2}\right) = 0 . \tag{1.32a}$$

It is a MUSCL-type algorithm like the nonlinear version of scheme III of van Leer (1977). The flux at the interfaces at $t = (n+1/2)\Delta t$ is evaluated by tracing the characteristic $\mathrm{d}x/\mathrm{d}t = u$ and solving the Riemann problem associated with (1.32a). $\mathcal{L}_S$ is the numerical solution operator for the ODE

$$\frac{\mathrm{d}u}{\mathrm{d}t} = g . \tag{1.32b}$$

In the present work, $\mathcal{L}_S$ is selected to be the second-order accurate, Runge-Kutta scheme. It could be argued that a more efficient split scheme might had been selected, such as an implicit one. But then again, the same is true for the unsplit scheme; the implicit version of the unsplit scheme for a scalar law can be easily implemented. The choice is made among second-order accurate schemes that had already been used in systems of PDE's such as the Euler equations. The MUSCL algorithm used in the split scheme is generally regarded as one of the most efficient algorithms. It is also worth mentioning that the proposed unsplit scheme does not require more operations per time-step than the selected split algorithm; *i.e.*, the computational cost is the same for both schemes.

Initial conditions are given by

$$u_0(x) = \begin{cases} 1 , & \text{for } x \leq 1 , \\ 0 , & \text{for } x > 1 , \end{cases} \tag{1.33}$$

with boundary conditions,

$$u(0,t) = 1 , \qquad u(\infty,t) = 0 , \qquad \forall t . \tag{1.34}$$

For both algorithms, the discretization is $\Delta x = 0.02$ and the CFL number is 0.8. Results for $\varepsilon = 0.01$, 0.02, 0.03, 0.05, and 0.07 are given in Figs. 1.4.

Let s be the shock speed. For this problem, $s = 0.5$. The relative error:

$$\frac{s_{\text{numerical}} - s_{\text{exact}}}{s_{\text{exact}}} ,$$

is plotted for both schemes in Fig. 1.5. The calculation of the numerical shock-wave speeds is based on the level set $u(x,t) = 0.5$. The split scheme gives a smaller error than the unsplit one in the regime $\Delta t/\varepsilon < 0.5$, but in that regime the relative error is above 40% for both schemes and would usually be unacceptable. The unsplit scheme seems to work slightly better than the split scheme in the cases where the above ratio is small. For $\varepsilon > 0.1$, both schemes give an error less than 10%. For values of ε less than 0.01, the computed wave speeds are one cell per time step. The numerical solutions go unstable for $\varepsilon = O(10^5)$ with both schemes. Results for this test case are also obtained by the unsplit scheme (1.17) based on the Taylor series expansion (1.24). The difference between the results given by that scheme and the ones given by the proposed unsplit scheme is negligible. Subsequently, the same test problem is solved with smaller CFL numbers, namely CFL =0.5 and $CFL = 0.2$. The changes, however, in the numerical results are small for both schemes. This observation reflects the fact that both the spatial and the time discretization have to be kept small to avoid spurious solutions.

It is interesting to mention that LeVeque & Yee (1990) studied the equation

$$u_t + u_x = -\frac{1}{\varepsilon} u(u-1)\left(u - \frac{1}{2}\right) ,$$

with initial data given by (1.33). They used split algorithms to solve this problem and they reported no spurious wave speeds for $\Delta t/\varepsilon \simeq 0.5$. This is most likely due to the difference in the source terms. For the source term in this equation, the pre-shock value, $u = 0$, is a stable equilibrium. In contrast, for the source term in the present work, the pre-shock value $u = 0$ is an unstable equilibrium. Consequently, values of $u(x,t)$ even slightly higher than 0 activate the source term which tends to increase u until the stable equilibrium is attained.

In the rest of this chapter, the issue of spurious continuous solutions is examined. The conservation law (1.7) is considered, with a source term given by (1.8). Initial and boundary conditions are given by

$$u_0(x) = e^{-x} , \tag{1.35}$$

$$u(0,t) = 1 , \qquad u(x \to \infty, t) = 0 , \qquad \forall\, t . \tag{1.36}$$

According to (1.11), a shock is never formed in this problem. Combining equations (1.10a) and (1.10b), we deduce the following expression for $u(x,t)$:

$$u(x,t) = \begin{cases} 1\,, & \text{for } x \le t\,, \\ e^{t-x}\left[u(x,t) + e^{t/\varepsilon}\left(1 - u(x,t)\right)\right]^{1-\varepsilon}\,, & \text{for } x > t\,. \end{cases} \tag{1.37}$$

Then, for $\varepsilon \ll 1$, the following approximation holds:

$$u(x,t) \simeq \begin{cases} 1\,, & \text{for } x \le t\,, \\ \dfrac{e^{-(x-t)}}{e^{-t/\varepsilon} + e^{-(x-t)}\left(1 - e^{-t/\varepsilon}\right)}\,, & \text{for } x > t\,. \end{cases} \tag{1.38}$$

The acoustic disturbance, located at $x = t$, initially set at the origin, travels with a speed equal to unity. Then, for an extended region, the spatial decrease of $u(x,t)$ is very slow, *i.e.*, $u(x,t)$ is *almost* equal to 1 within this region. The length of this region increases with time at a rate $(1/\varepsilon + 1)$. After that region, the spatial decrease of $u(x,t)$ is exponential. Therefore, the solution to this problem is approximately an exponential profile travelling with speed

$$c_{\text{e.p.}} = \frac{1}{\varepsilon} + 1\,.$$

Results for this case, obtained by the split scheme, the proposed unsplit scheme, and also by the unsplit scheme (1.17), based on the Taylor-series expansion (1.24), hereafter dubbed as "unsplit - TSE", are presented in Fig. 1.6, for $\varepsilon = 0.01$. The exact solution, computed from (1.37) using Newton iteration, is plotted for comparison purposes. It is clearly seen that the proposed unsplit scheme and the MUSCL split scheme perform better than the unsplit scheme based on Taylor-series expansion. Furthermore, the proposed scheme is slightly superior than the split one. The CFL number is 0.5 for all schemes. When the CFL number is increased to 0.8, the proposed unsplit scheme is again very accurate, and slightly superior than the split scheme; see Fig. 1.6c. For $\varepsilon = 0.01$ the relative error,

$$\left| \frac{c_{\text{numerical}} - c_{\text{e.p.}}}{c_{\text{e.p.}}} \right|\,,$$

in the calculation of the speed of the exponential front against the inverse of the resolution $1/\Delta x$, is presented in Fig. 1.7, for all three schemes. The calculation of the numerical speed is based on the level set $u(x,t) = 0.5$.

It is worth mentioning that, for this particular shock-free case, an increase of Δx, with Δt held constant, did not seem to affect the accuracy of any of the schemes. It is found that fixing Δt at a value of order $O(\varepsilon)$, and satisfying the CFL condition, is enough to produce reasonable results, even when Δx is an order of magnitude or more higher than $\Delta t\,|u|$. This observation is not valid in the case of discontinuous solutions, where both the spatial and the temporal discretization have to be of order $O(\varepsilon)$, or less, to avoid spurious shock waves.

The accuracy of the schemes remains at the same levels when the value of the stiffness coefficient is increased to $1/\varepsilon = 500$, with a proportionally finer resolution. Again, the proposed unsplit scheme is slightly better than the split one, but both outperformed the Taylor-series based algorithm (see Fig. 1.8).

In summary, it was observed that neither the proposed scheme nor the split one give accurate wave speeds if the time-step is not smaller than the stiffness coefficient, ε, especially when discontinuities are present. This is not surprising because both schemes are explicit, and resolution of the smallest time-scale is necessary. However, for reasonable time-steps, the proposed unsplit scheme is slightly more accurate, particularly in cases characterized by a large value of the stiffness coefficient.

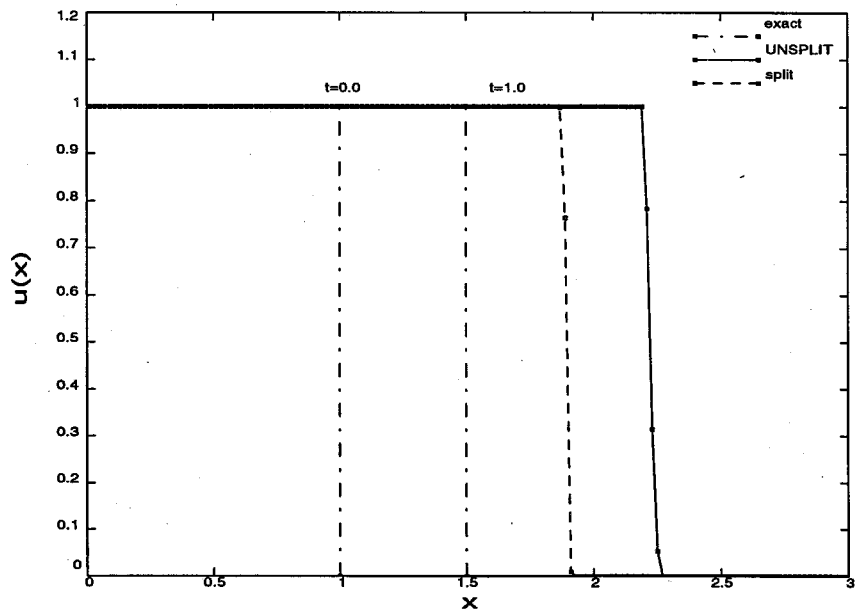

FIG.1.4a Performance of unsplit and split algorithm for the problem given by (1.7), (1.8), (1.33), and (1.34) for $\varepsilon = 0.01$.

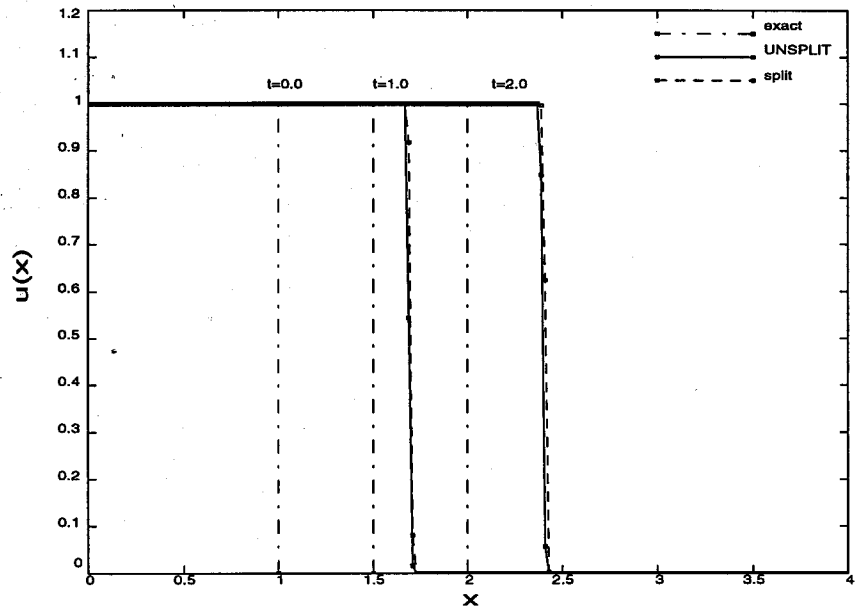

FIG.1.4b Performance of unsplit and split algorithm for the problem given by (1.7), (1.8), (1.33), and (1.34) for $\varepsilon = 0.02$.

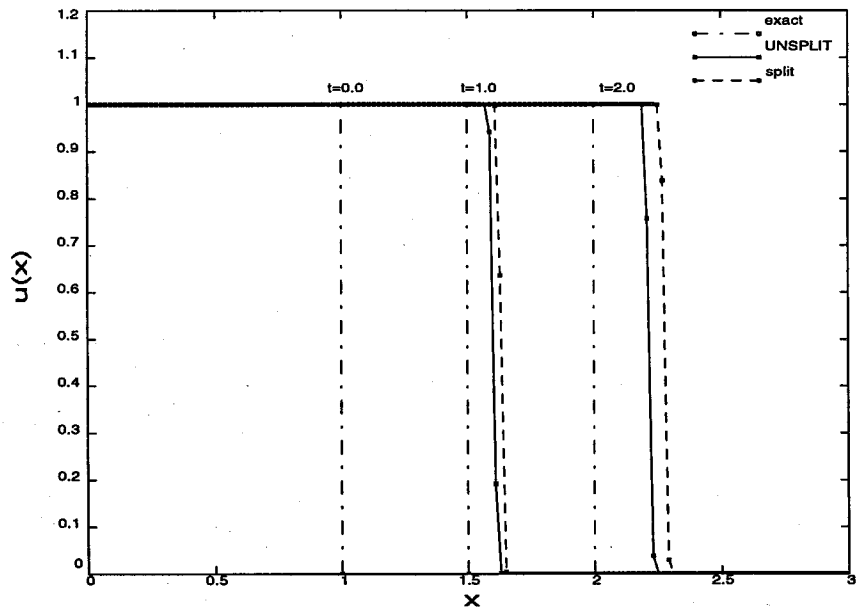

FIG.1.4c Performance of unsplit and split algorithm for the problem given by (1.7), (1.8), (1.33), and (1.34) for $\varepsilon = 0.03$.

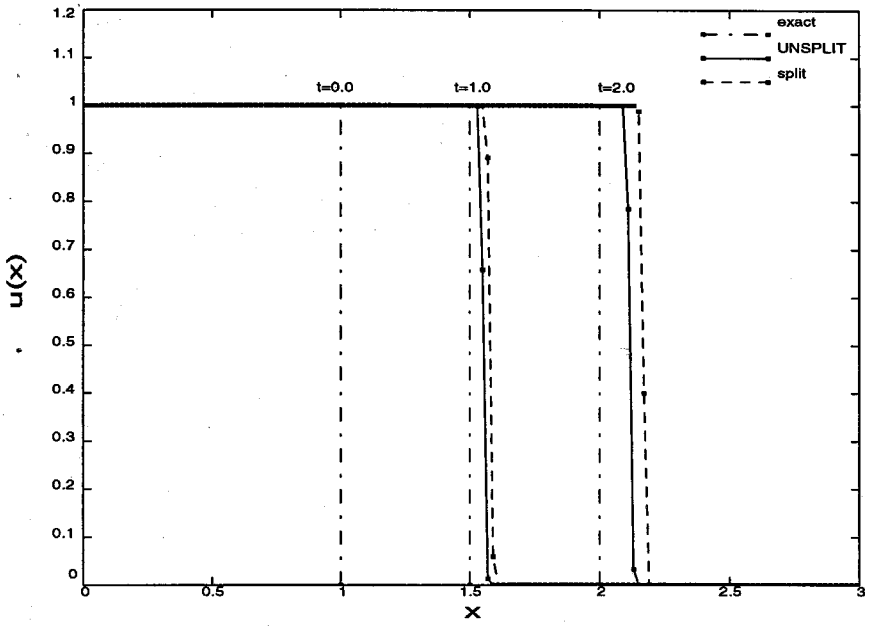

FIG.1.4d Performance of unsplit and split algorithm for the problem given by (1.7), (1.8), (1.33), and (1.34) for $\varepsilon = 0.05$.

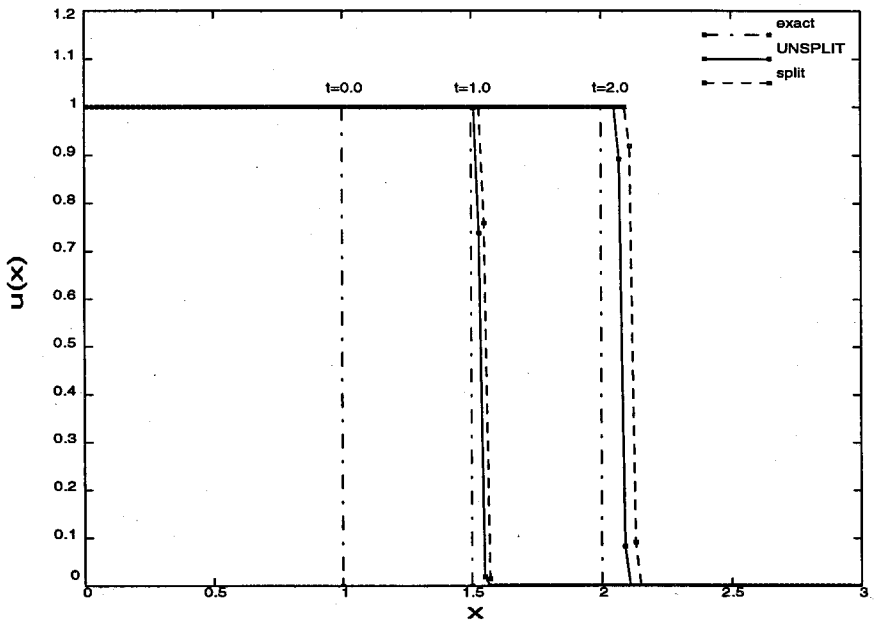

FIG.1.4e Performance of unsplit and split algorithm for the problem given by (1.7), (1.8), (1.33), and (1.34) for $\varepsilon = 0.07$.

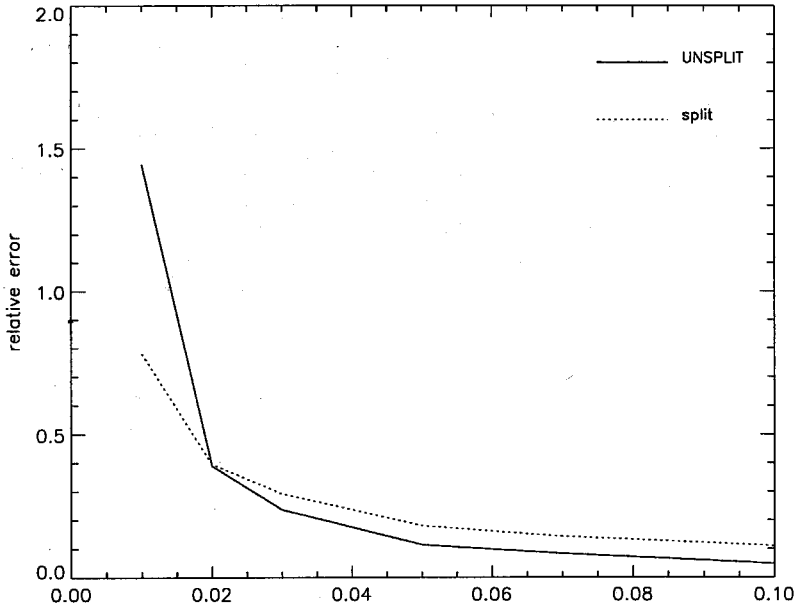

FIG.1.5 Relative error for the split and unsplit algorithm for the problem given by (1.7), (1.8), (1.33), and (1.34). $\Delta x = 0.02, CFL = 0.80$.

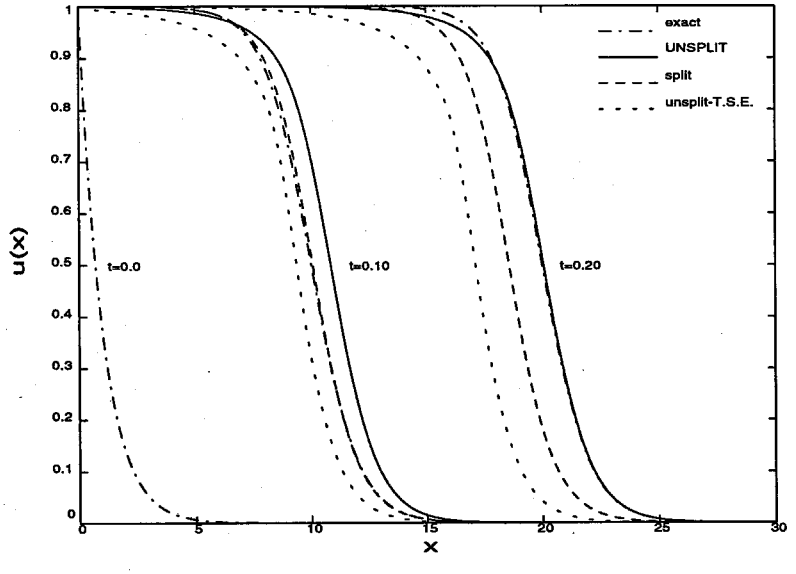

FIG.1.6a Performance of unsplit and split algorithms for the problem given by (1.7), (1.8), (1.35), and (1.36) for $\epsilon = 0.01$. $\Delta x = 0.03$, $CFL = 0.5$.

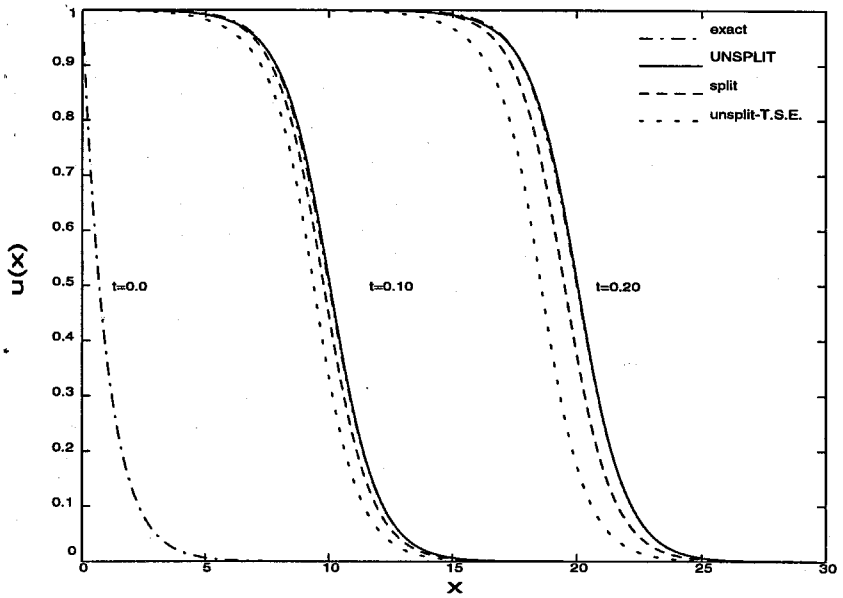

FIG.1.6b Performance of unsplit and split algorithms for the problem given by (1.7), (1.8), (1.35), and (1.36) for $\varepsilon = 0.01$. $\Delta x = 0.02$, $CFL = 0.5$.

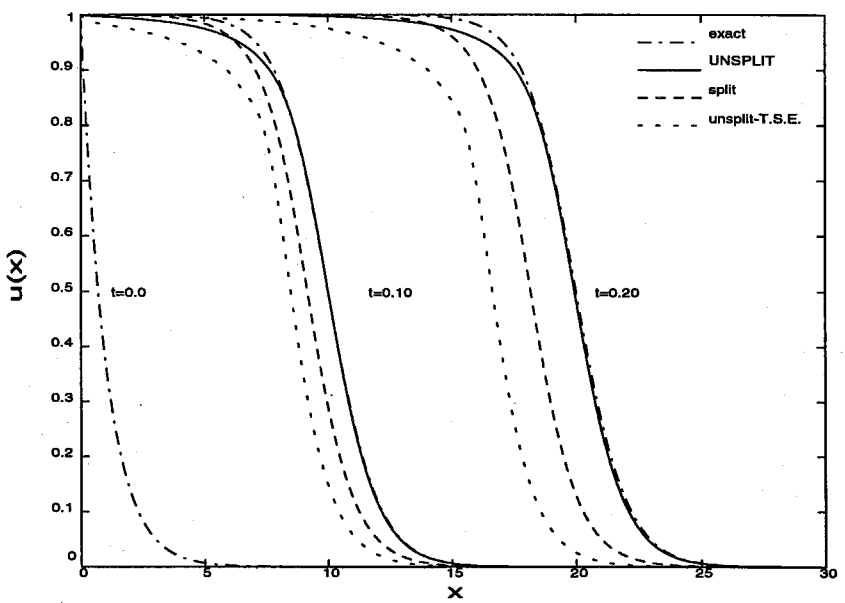

FIG.1.6c Performance of unsplit and split algorithms for the problem given by (1.7), (1.8), (1.35), and (1.36) for $\varepsilon = 0.01$. $\Delta x = 0.02$, $CFL = 0.8$.

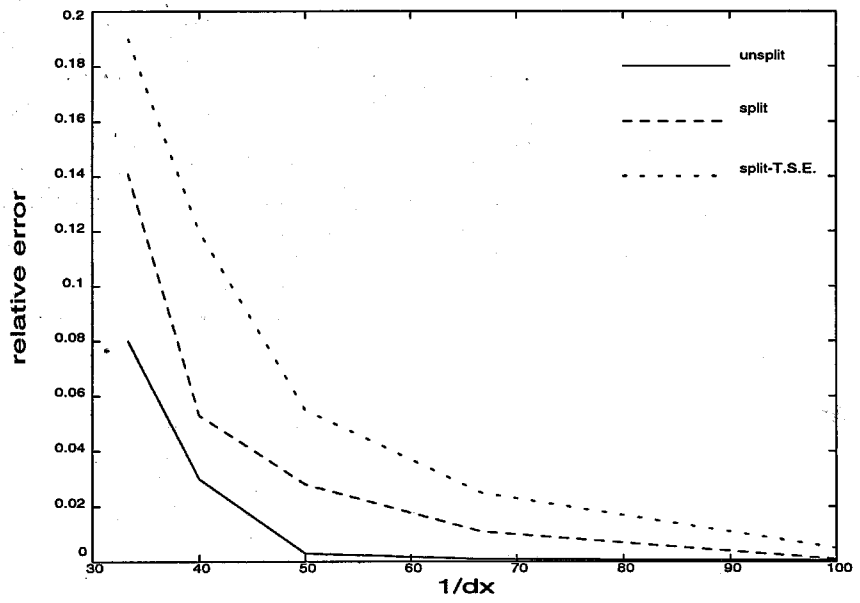

FIG.1.7 Relative error in the calculation of the speed of the exponential front for the problem given by (1.7), (1.8), (1.35), and (1.36) for $\varepsilon = 0.01$. All computations were performed with $CFL = 0.5$.

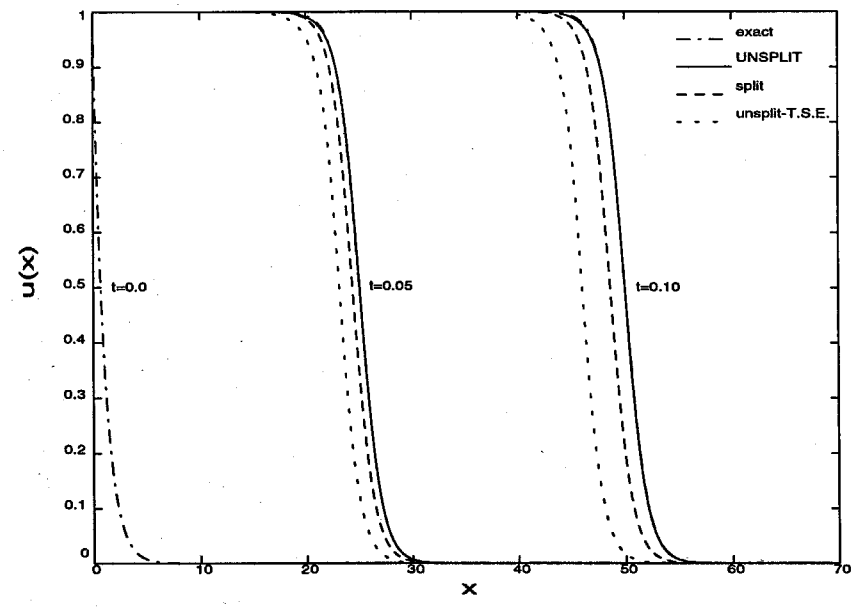

FIG.1.8 Performance of unsplit and split algorithms for the problem given by (1.7), (1.8), (1.35), and (1.36) for $\varepsilon = 0.002$. $\Delta x = 0.004$, $CFL = 0.5$.

CHAPTER 2

The One-Dimensional Euler Equations for Reacting Flows

Research in detonating flows was pioneered by Von Neumann (1942), Zeldovich (1960), Doering (1943), 50 years ago, and subsequently by others. Numerical integration of the governing equations, in high-resolution meshes, was initiated by Fickett & Wood (1966). In the past, progress was achieved in the study of the stability; see, *e.g.*, Erpenbeck (1964), Lee & Stuart (1990), and the high- and low-frequency asymptotic nature of detonations. See, *e.g.*, DiPerna & Majda (1985), Majda & Rosales (1984), (1987), Choi & Majda (1989), Majda & Roytburd (1990), Kapila *et al.* (1983), *etc.*

Accurate algorithms for gas dynamics were first employed in detonation problems in the late '80s using splitting techniques; see *e.g.*, Colella *et al.* (1986), and Yee (1987). Further development of these codes and extensive numerical investigations were carried through to the 90's. See, *e.g.*, Bourlioux *et al.* (1991), Lappas *et al.* (1993), Pember (1993), Quirk (1993), LeVeque & Shyue (1995), *etc.* All these algorithms use a splitting technique.

So far, efforts to design unsplit schemes have been based on the idea of modifying the Riemann problem that has to be solved on the cell interfaces, to take care of the presence of the source terms. This idea of a generalized Riemann problem was introduced by Liu (1979) for quasi-one-dimensional (area-varying) gas flows. He considered a Riemann problem where the initial data were not uniform on each cell but satisfied the steady-state equations, in order to construct a random-choice method to prove existence of global solutions for the non-homogeneous system of equations. Glimm *et al.* (1984) and van Leer (1984) derived second-order accurate schemes for such flows based on this idea. Roe (1986) proposed the addition of extra terms in the expressions of the wave strengths in Roe's approximate Riemann solver, Roe (1981), that take into account the source terms.

Ben-Artzi & Falcovitz (1986), also concerned with area-varying flows, considered a Riemann problem for the non-homogeneous equations with linearly-distributed initial states. They derived expressions for the time derivatives of the unknown variables, and their fluxes, by solving this Riemann problem, and then used these expressions in the upwinding step of their algorithm. Application of this strategy to unsplit schemes for reacting flows was presented by Ben-Artzi (1989).

As mentioned earlier, Lappas *et al.* (1995) proposed another way to avoid splitting, by making use of a particular decomposition of the governing equations. This decomposition, which leads to the introduction of new curves in space-time, was applied in the first chapter for a scalar conservation law. In this chapter, the work of Lappas *et al.* is extended to systems of hyperbolic conservation laws with source terms, such as compressible, reacting flows.

For one-dimensional systems, a set of curves is defined in space-time, such that the equations that hold along these curves are the same as the equations that hold along the characteristics in the corresponding homogeneous case. As in the case discussed by Lappas *et al.*, the local geometry of these curves depends on the spatial derivatives of the flow variables, as well as on the source terms themselves. These curves facilitate the design of unsplit algorithms. In particular, an effort has been made to improve the performance of the MUSCL-type schemes by constructing algorithms in which the integration of the equations, including the contributions of the source terms, is performed in a single, fully-coupled step. This is achieved by tracing the corresponding invariant curves, in a way analogous to characteristic-tracing in the homogeneous case.

The case of detonation problems is particularly interesting, as regards applications, but it is also very difficult to simulate numerically. This difficulty arises from the large number of time-scales and length-scales associated with these problems. Numerical simulations are performed in regimes where the solutions are stable, but also in those regimes where unstable and even chaotic behavior is encountered. The source terms of the equations are typically stiff in these regimes. Comparisons with results obtained by conventional schemes are made, accompanied by observations concerning the behavior of high activation-energy detonations.

2.1 General Formulation

A homogeneous, first-order system of M quasi-linear equations in two independent variables (x,t)

$$\frac{\partial \mathbf{U}}{\partial t} + \frac{\partial \mathbf{F}(\mathbf{U})}{\partial x} = 0\,, \tag{2.1}$$

is called hyperbolic, if the Jacobian $\mathbf{DF}(U)$ has real eigenvalues λ_k, $k = 1,\ldots,M$. In the equation above, $\mathbf{U} = (u_1,\ldots,u_M)$ is the solution vector, and $\mathbf{F}(\mathbf{U})$ is the corresponding flux vector. One can write the system in characteristic form:

$$\mathbf{l}_k \cdot \left(\frac{\mathrm{d}\mathbf{U}}{\mathrm{d}t}\right)_k = 0\,, \qquad k = 1,\ldots,M\,, \tag{2.2}$$

(repeated index does not imply summation), with

$$\left(\frac{\mathrm{d}}{\mathrm{d}t}\right)_k \equiv \frac{\partial}{\partial t} + \lambda_k \frac{\partial}{\partial x}\,. \tag{2.3}$$

This is done by performing the following steps:

1. Evaluate the eigenvalues of the Jacobian $\mathbf{DF}(\mathbf{U})$, and the corresponding left eigenvectors $\mathbf{l}_k = (l_1,...,l_M)_k$, $k = 1,\ldots,M$.
2. Multiply system (2.1) by $\mathbf{l}_k$, $k = 1,\ldots,M$.

There are cases where the system of ODE's (2.2) is integrable. The equations describing isentropic one-dimensional gas dynamic flows represent such an example. In such cases, the following relation holds:

$$\mathbf{l}_k \cdot \left(\frac{\mathrm{d}\mathbf{U}}{\mathrm{d}t}\right)_k = \left(\frac{\mathrm{d}R_k}{\mathrm{d}t}\right)_k = 0\,, \qquad k = 1,\ldots,M\,. \tag{2.4}$$

The functions R_k, $k = 1,\ldots,M$, are called Riemann invariants, and remain constant along the corresponding characteristic directions:

$$\frac{\mathrm{d}x}{\mathrm{d}t} = \lambda_k\,, \qquad k = 1,\ldots,M\,. \tag{2.5}$$

In general, the system (2.2) is not integrable. Nonetheless, numerical evidence, coming mainly from results based on shock-capturing schemes for the one-dimensional Euler equations of gas dynamics, *e.g.*, van Leer (1979), and Colella & Woodward (1984), has shown that it is useful for numerical purposes to try to decompose the initial system of PDE's (2.1) to the characteristic set (2.2). The phrase *numerical purposes* can be defined as "development of algorithms that are both accurate and stable". As mentioned above, in the homogeneous case, the system (2.2) holds along the characteristic lines (2.5).

The case of non-homogeneous systems, *i.e.*,

$$\frac{\partial \mathbf{U}}{\partial t} + \frac{\partial \mathbf{F}(\mathbf{U})}{\partial x} = \mathbf{G}(\mathbf{U}) , \tag{2.6}$$

is not so straightforward. In the later case, the set of equations (2.2) does not hold along the characteristics (2.5). A straightforward calculation shows that the system of ODE's (2.2) holds along the curves defined by

$$\frac{\mathrm{d}x}{\mathrm{d}t} = \lambda_k - \frac{\mathbf{l}_k \cdot \mathbf{G}(\mathbf{U})}{\mathbf{l}_k \cdot \partial \mathbf{U}/\partial x} , \qquad k = 1, \ldots, M . \tag{2.7}$$

It is the system of equations (2.2) that can be easily discretized and solved numerically in the upwinding step of a shock-capturing solver. While this decomposition holds only at smooth parts of the flow, this is not a serious restriction. The numerical treatment of the above decomposition in non-smooth parts of the flow is completely analogous to the treatment of the characteristic decomposition, for the homogeneous case, when shocks are present. Even though the characteristic decomposition in the homogeneous case holds only when the solution is continuous, it is still useful numerically in the presence of shocks because it holds on either side of the discontinuity. Furthermore, the computation of these curves can be performed at no extra cost, since the information about the spatial derivatives of the flow is always available at points where the solution is known.

2.2 Formulation of the One-Dimensional Detonation Problem

Consider a simple model of chemical interaction of two calorically perfect gases, $A \rightarrow B$, assuming one-step, irreversible, Arrhenius kinetics, and the absence of dissipation mechanisms.

The conservation equations are given by:

$$\frac{\partial}{\partial t}\rho + \frac{\partial}{\partial x}(\rho u) = 0\,, \tag{2.8a}$$

$$\frac{\partial}{\partial t}(\rho u) + \frac{\partial}{\partial x}(\rho u^2 + p) = 0\,, \tag{2.8b}$$

$$\frac{\partial}{\partial t}(\rho e_{\mathrm{t}}) + \frac{\partial}{\partial x}[(\rho e_{\mathrm{t}} + p)u] = 0\,, \tag{2.8c}$$

$$\frac{\partial}{\partial t}(\rho z) + \frac{\partial}{\partial x}(\rho u z) = \rho g(T, z)\,. \tag{2.8d}$$

The total specific energy and the source term are given by

$$e_{\mathrm{t}} \equiv \frac{p}{\rho(\gamma - 1)} + q_0 z + \frac{u^2}{2}\,, \tag{2.9}$$

and

$$g(T, z) = -K z\, e^{-E_{\mathrm{a}}/T}\,, \tag{2.10}$$

respectively. The equation of state reads:

$$T = \frac{p}{\rho}\,. \tag{2.11}$$

In the equations above, z is the reactant mass fraction, γ is the specific-heat ratio (assumed the same for both species), and q_0 is the heat-release parameter. E_{a} is the activation energy parameter, and K is an amplitude parameter that sets the spatial and temporal scales. As employed here, $0 \leq z \leq 1$. It equals unity, when the material is totally unreacted, and zero when the reaction has been completed.

Despite the simplicity of this model, computing such flows is quite challenging. The reason is that for a wide range of values of the parameters of the reaction-rate equation, q_0, E_a, K, this system of conservation laws is linearly and non-linearly unstable. Furthermore, the reaction-rate equation is generally stiff, and this leads to a large range of (coupled) spatial and temporal modes. Required resolution for numerical simulation of these flows typically exceeds available computational resources.

The system (2.8) can be written in conservation form, *i.e.*, in the divergence form of (2.6), by setting:

$$\mathbf{U} \equiv [u_1, u_2, u_3, u_4]^{\mathrm{T}} = [\rho, \rho u, \rho e_{\mathrm{t}}, \rho z]^{\mathrm{T}} , \tag{2.12a}$$

$$\mathbf{F}(\mathbf{U}) \equiv \left[u_2, \frac{u_2^2}{u_1} + p(\mathbf{U}), \frac{u_2}{u_1}(u_3 + p), \frac{u_2 u_4}{u_1}\right]^{\mathrm{T}} , \tag{2.12b}$$

$$\mathbf{G}(\mathbf{U}) \equiv [0, 0, -q_0(\gamma - 1)g, g]^{\mathrm{T}} , \tag{2.12c}$$

with

$$p = p(\mathbf{U}) = (\gamma - 1)\left(u_3 - \frac{u_2^2}{2u_1} - q_0 u_4\right) , \tag{2.13a}$$

$$g = g(\mathbf{U}) = -K u_4 \, e^{-E_a u_1 / p(\mathbf{U})} . \tag{2.13b}$$

The eigenvalues of the system are:

$$\lambda_1 = u + \sqrt{\frac{\gamma p}{\rho}} , \tag{2.14a}$$

$$\lambda_{2,3} = u , \tag{2.14b}$$

$$\lambda_4 = u - \sqrt{\frac{\gamma p}{\rho}} . \tag{2.14c}$$

The second eigenvalue is degenerate; therefore, z can sustain jumps only across contact discontinuities.

The following curves in the (x,t)-plane can be defined by performing the decomposition of the system to a set of ODE's, as described in the previous section:

$$\mathcal{C}_{\pm}: \qquad \frac{\mathrm{d}x}{\mathrm{d}t} = u \pm a + u_{\pm} \,, \tag{2.15a}$$

$$\mathcal{C}_{0}: \qquad \frac{\mathrm{d}x}{\mathrm{d}t} = u + u_{0} \,, \tag{2.15b}$$

$$\mathcal{C}_{\mathrm{r}}: \qquad \frac{\mathrm{d}x}{\mathrm{d}t} = u + u_{\mathrm{r}} \,, \tag{2.15c}$$

with

$$a \equiv \sqrt{\frac{\gamma\, p}{\rho}}$$

and

$$u_{\pm} \equiv -\frac{K\, q_0(\gamma-1)\,\rho\, z\, e^{-E_{\mathrm{a}}/T}}{\partial p/\partial x \;\pm\; \rho a\,(\partial u/\partial x)} \tag{2.16a}$$

$$u_{0} \equiv -\frac{K\, q_0(\gamma-1)\,\rho\, z\, e^{-E_{\mathrm{a}}/T}}{\partial p/\partial x \;-\; a^2\,(\partial \rho/\partial x)} \tag{2.16b}$$

$$u_{\mathrm{r}} \equiv \frac{K\, z\, e^{-E_{\mathrm{a}}/T}}{\partial z/\partial x} \,. \tag{2.16c}$$

The ODE's that hold along these curves are:

$$\text{along } \mathcal{C}_{\pm}: \qquad \mathrm{d}p \pm \rho a\, \mathrm{d}u \;=\; 0 \,, \tag{2.17a}$$

$$\text{along } \mathcal{C}_{0}: \qquad \mathrm{d}p - a^2\, \mathrm{d}\rho \;=\; 0 \,, \tag{2.17b}$$

$$\text{along } \mathcal{C}_{\mathrm{r}}: \qquad \mathrm{d}z \;=\; 0 \,. \tag{2.17c}$$

There can be parts of the flow where the values of the added convection velocities, u_α, for $\alpha = 0, +, -, \mathrm{r}$, defined by (2.16) are small and the curves defined by (2.15) are very close to the corresponding (classical) characteristic curves. But there can also be parts of the flow where these are not negligible. In the latter case, the propagation speeds, $u \pm a + u_{\pm}$, will be considerably different from the

classical characteristic speeds, $u \pm a$, and might even differ in sign. Interestingly, portions of these curves that emanate from some point, P, in the (x,t)-plane, might lie outside the region enclosed by the (classical) characteristics emanating from P, *i.e.*, the domain of dependence of P. In such cases, the curves (2.15) might then be classified as locally space-like, otherwise locally time-like. Nevertheless, it is the (invariant) curve equations given by (2.7) that are the ones along which the characteristic equations apply (exactly). These equations translate to the system (2.15) for the problem under study here.

2.3 Description of the Numerical Scheme

A second-order accurate MUSCL scheme, based on the above decomposition, is designed to solve the system of equations (2.8) numerically. Consider a finite-volume formulation, *i.e.*, space is discretized to a set of computational cells of length Δx. Additionally, consider mass-averaged values of the conservative variables

$$m_j \equiv \int_{x_{j-1/2}}^{x_{j+1/2}} \rho \, \mathrm{d}x \,, \tag{2.18a}$$

$$m_j u_j \equiv \int_{x_{j-1/2}}^{x_{j+1/2}} \rho u \, \mathrm{d}x \,, \tag{2.18b}$$

$$m_j e_{\mathrm{t}j} \equiv \int_{x_{j-1/2}}^{x_{j+1/2}} \rho e_{\mathrm{t}} \, \mathrm{d}x \,, \tag{2.18c}$$

$$m_j z_j \equiv \int_{x_{j-1/2}}^{x_{j+1/2}} \rho z \, \mathrm{d}x \,. \tag{2.18d}$$

Finally, set

$$m_j g_j \equiv \int_{x_{j-1/2}}^{x_{j+1/2}} \rho g(T,z) \, \mathrm{d}x \,. \tag{2.19}$$

In these expressions, average values of all quantities in the j^{th} cell are denoted by the subscript j, while values of various quantities at the cell boundaries are denoted by $j \pm 1/2$.

By using the following notation for the fluxes of the system

$$F_m \equiv \rho u \,, \tag{2.20a}$$

$$F_u \equiv \rho u^2 + p \,, \tag{2.20b}$$

$$F_e \equiv \rho e_t u + p u \,, \tag{2.20c}$$

$$F_z \equiv \rho z u \,, \tag{2.20d}$$

the conservation equations at the j^{th} cell are written as

$$\frac{\mathrm{d}}{\mathrm{d}t} m_j + (F_m)_{j+1/2} - (F_m)_{j-1/2} = 0 \,, \tag{2.21a}$$

$$\frac{\mathrm{d}}{\mathrm{d}t} (m_j u_j) + (F_u)_{j+1/2} - (F_u)_{j-1/2} = 0 \,, \tag{2.21b}$$

$$\frac{\mathrm{d}}{\mathrm{d}t} (m_j e_{tj}) + (F_e)_{j+1/2} - (F_e)_{j-1/2} = 0 \,, \tag{2.21c}$$

$$\frac{\mathrm{d}}{\mathrm{d}t} (m_j z_j) + (F_z)_{j+1/2} - (F_z)_{j-1/2} = m_j g_j \,. \tag{2.21d}$$

As in the case of the scalar conservation law, linear interpolation is used for all quantities on each cell. The slopes are estimated by van Albada's limiter (1.16). The proposed scheme, which evaluates the solution at time $(n+1)\Delta t$ from the solution at the previous time $n\Delta t$, can be written as:

$$m_j^{n+1} = m_j^n - \Delta t \left[(F_m)_{j+1/2}^{n+1/2} - (F_m)_{j-1/2}^{n+1/2} \right] \,, \tag{2.22a}$$

$$(m_j u_j)^{n+1} = (m_j u_j)^n - \Delta t \left[(F_u)_{j+1/2}^{n+1/2} - (F_u)_{j-1/2}^{n+1/2} \right] \,, \tag{2.22b}$$

$$(m_j e_{tj})^{n+1} = (m_j e_{tj})^n - \Delta t \left[(F_e)_{j+1/2}^{n+1/2} - (F_e)_{j-1/2}^{n+1/2} \right] \,, \tag{2.22c}$$

$$(m_j z_j)^{n+1} = (m_j z_j)^n - \Delta t \left[(F_z)_{j+1/2}^{n+1/2} - (F_z)_{j-1/2}^{n+1/2} + (m_j g_j)^{n+1/2} \right] \tag{2.22d}$$

The numerical fluxes $(F_m)_{j+1/2}^{n+1/2}$, $(F_u)_{j+1/2}^{n+1/2}$, $(F_e)_{j+1/2}^{n+1/2}$, $(F_z)_{j+1/2}^{n+1/2}$, are given by equations (2.20) and are evaluated by solving the ODE's (2.17) numerically along the curves defined by (2.15). The case where a denominator in the expressions for u_+, u_-, u_0, u_r vanishes is treated in the same way as in the scalar law. Since the points of vanishing denominators are not points of singularity but simply points of

singularity but simply points of locally zero convection upwinding can be obtained by a Taylor expansion in time. In practice, when one of these denominators becomes smaller that a critical value inside a cell (in the present implementation of the scheme this value is 10^{-4}, made dimensionless with respect to the reference state), Taylor-series expansion is used. This procedure ensures, uniformly, second-order accuracy, in both space and time, for smooth parts of the flow. Numerical tests showed that no spurious oscillations occur because of the use of Taylor expansion at those isolated points.

This set of ODE's must be supplemented with the appropriate jump relations, to take care of the presence of the discontinuities, *i.e.*, a Riemann problem has to be solved locally at each cell interface. The exact jump relations have to be used in the cells where the density and pressure slopes are large. The acoustic approximation can be used otherwise. A detailed description of the Riemann solver that is used can be found in Lappas *et al.* (1993). The Riemann problem that corresponds to this set of equations, referred as "Generalized Riemann Problem" (GRP), is not the same as the classical one-dimensional, gasdynamic Riemann problem (RP). The GRP is not a self-similar problem and its solution is more complicated. The shock and expansion waves are curved in the (x,t)-plane; *i.e.*, they are accelerating. The solution to the GRP has been worked out by Ben-Artzi (1989), who showed that the solution approaches the solution of the RP in the limit $x \to 0$, and $t \to 0$. The use of the classical Riemann problem for numerical purposes is, therefore, justified by the same arguments that were mentioned in the first chapter of this work, which deals with scalar laws. It will be verified in the next section that, using this approximation, the acceleration of the various waves can be captured numerically quite well.

2.4 Numerical Results for One-Dimensional Detonations

In the early 40's, Zeldovich (1960), von Neumann (1942), and Doering (1943) independently proposed that detonation waves in one-dimensional flows are steady shock waves, propagating in a medium of local thermodynamic equilibrium, and followed by a reaction zone of finite length. This theory is historically known as the ZND theory of detonations. Given a fixed state ahead of the detonation, the computation of the spatial profiles of the solution reduces to the numerical integration

the pressure and the reactant mass fraction are given in Figs. 2.1.

For the detonations governed by the one-step irreversible Arrhenius law (2.9b), there is a minimum shock velocity. This is the Chapman-Jouguet velocity, $D_{\rm CJ}$. A reaction process characterized by this shock velocity is called a Chapman-Jouguet detonation. The point at the end of the reaction zone of a Chapman-Jouguet detonation is sonic. For every detonation, the shock velocity, D, has to satisfy:

$$D \geq D_{\rm CJ} \, .$$

The parameter f, defined as $f \equiv (D/D_{\rm CJ})^2$, is the overdrive factor of the detonation. The half-reaction length, $L_{1/2}$, *i.e.*, the distance between the shock wave and the point where $z = 0.5$, has been used as the unit length, throughout. The half-reaction length divided by the sound speed ahead of the shock serves as the time unit. Experimental studies suggest, in contrast with ZND theory, that detonation phenomena are generally unstable and possess a far more complicated structure; see, *e.g.*, Fickett & Davis (1979). Linear-stability analysis of the equations (2.8) by Erpenbeck (1964), and Lee & Stewart (1990), verify that the system is unstable for a large range of the parameters γ, q_0, $E_{\rm a}$, and f.

In the following, the variables and parameters of the system have been made dimensionless by reference to the uniform state ahead of the detonation front, hence f becomes the stability parameter of the system. The remaining parameters have been fixed as follows:

$$\gamma \, = \, 1.2 \, , \qquad q_0 \, = \, 50 \, , \qquad E_{\rm a} \, = \, 50.$$

According to linear-stability analysis, there is a critical value f^* at which the real part of one of the eigenvalues of the system changes sign and becomes positive.

The system is unstable for overdrives below this critical value, with additional eigenmodes becoming unstable as f decreases. This is to be expected, since a decrease in the overdrive implies lower post-shock temperature and an increasing ratio of the activation energy over this temperature. That makes the reaction zone more sensitive to small changes of the hydrodynamic shock strength. The critical value of the overdrive factor, for the above set of parameters, is $f^* = 1.72$. It should also be noted that the value of the stiffness coefficient, K, is determined

completely by the value of f and the normalized speed of sound ahead of the shock, $\sqrt{\gamma}$. In particular, K increases as the overdrive factor f decreases, *i.e.*, the lower the post-shock temperature is, the slower the reaction becomes.

In the numerical simulations presented here, the spatial ZND profiles for various overdrive factors are evaluated and given to the computer code as initial condition. The truncation error is left to trigger the instabilities, and the evolution process is observed. The state at the left boundary is always given by the state at the end of the reaction zone at $t = 0$, that is the left end-point of the ZND profile. All computations are performed with $CFL = 0.50$, where

$$CFL \equiv \frac{\Delta t}{\Delta x} |u + a|_{\max} . \tag{2.23}$$

As a first test, the overdrive factor is taken to be $f = 1.8$. This is a case of a stable detonation. The shock speed and stiffness coefficient for this case are $D = 9.1357$, and $K = 145.69$, respectively. The time history of the shock pressure, *i.e.*, the pressure immediately behind the shock is presented in Fig. 2.2; the fluctuation of the shock pressure decays with time. The resolution for this simulation is $15\,\mathrm{pts}/L_{1/2}$. The results of the time history of the shock pressure are in very good agreement with the results obtained by Bourlioux *et al.* (1991), using the Piecewise Parabolic Method (PPM) and front-tracking, with the same resolution.

The overdrive factor is then lowered to $f = 1.6$. This case corresponds to $D = 8.6134$, and $K = 230.75$. Linear-stability analysis predicts one unstable mode for this case. The time history of the shock pressure is presented in Fig. 2.3a. The spatial profile of the pressure at $t = 80.0$ is presented in Fig. 2.3b. Following Quirk (1993), a convergence study for the peak shock pressure for various numerical schemes is performed, and the results are presented in Fig. 2.3c. The numerical schemes are: PPM with front-tracking and mesh refinement, Bourlioux *et al.* (1991), Roe's solver with Superbee Limiter, Quirk (1993), Roe's Solver with the Minmod Limiter, Quirk (1993), and the present unsplit scheme. In this figure, a relative mesh spacing of 1 corresponds to a resolution of $10\,\mathrm{pts}/L_{1/2}$; similarly, a relative mesh spacing of 0.25 corresponds to a resolution of $40\,\mathrm{pts}/L_{1/2}$. The schemes are seen to converge to approximately the value predicted by Fickett & Wood (1979), who estimated that the peak pressure is 98.6.

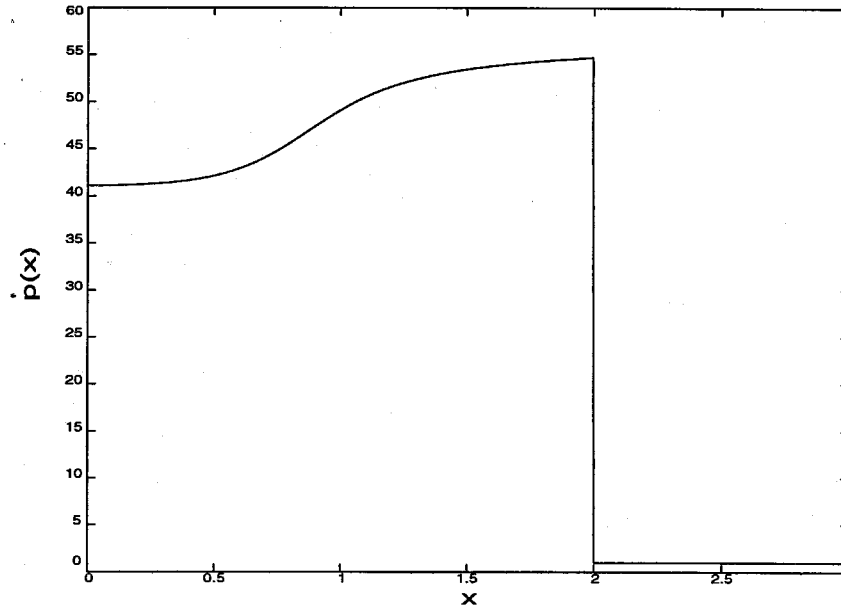

FIG.2.1a Typical spatial profile of the pressure for a ZND detonation.

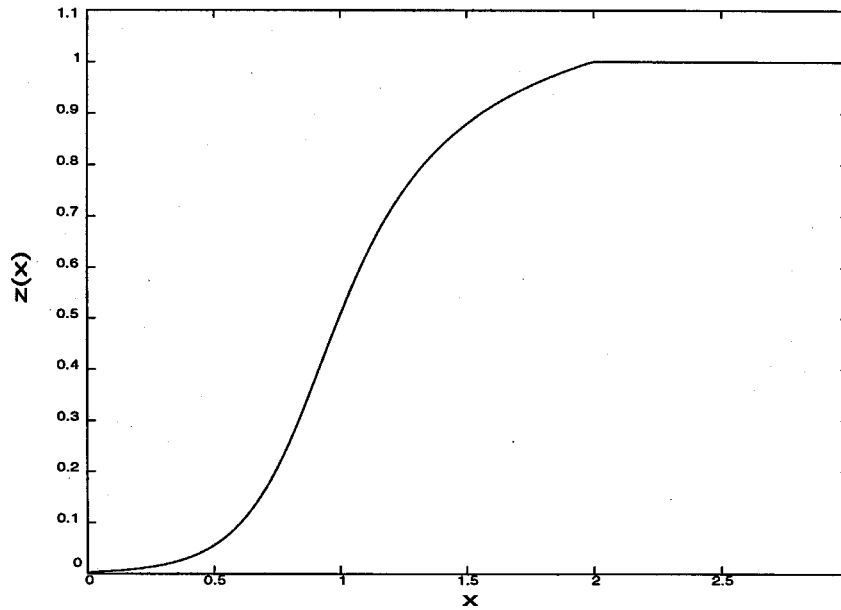

FIG.2.1b Typical spatial profile of the reactant mass fraction for a ZND detonation.

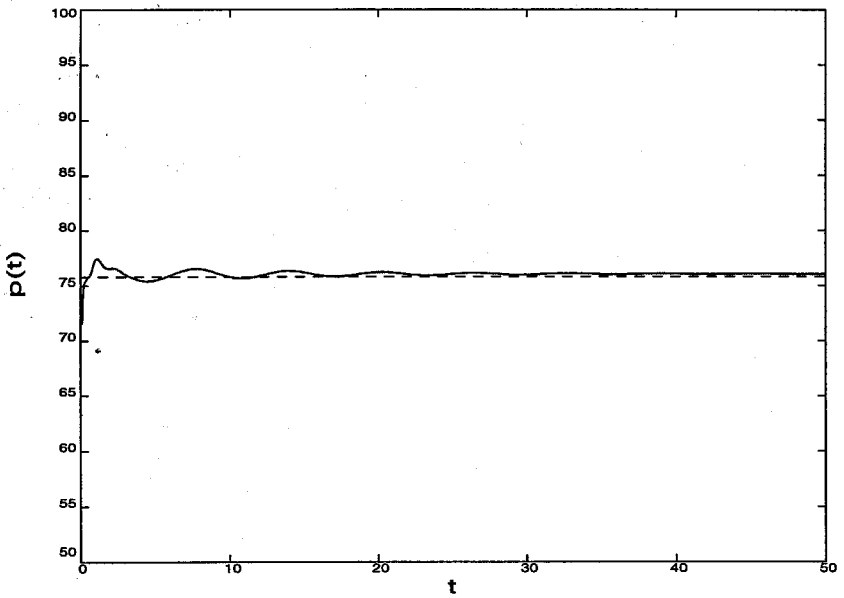

FIG.2.2 Time history of the shock pressure for a detonation with an overdrive factor, $f = 1.80$. Resolution, $15\,\text{pts}/L_{1/2}$. Horizontal line represents ZND solution.

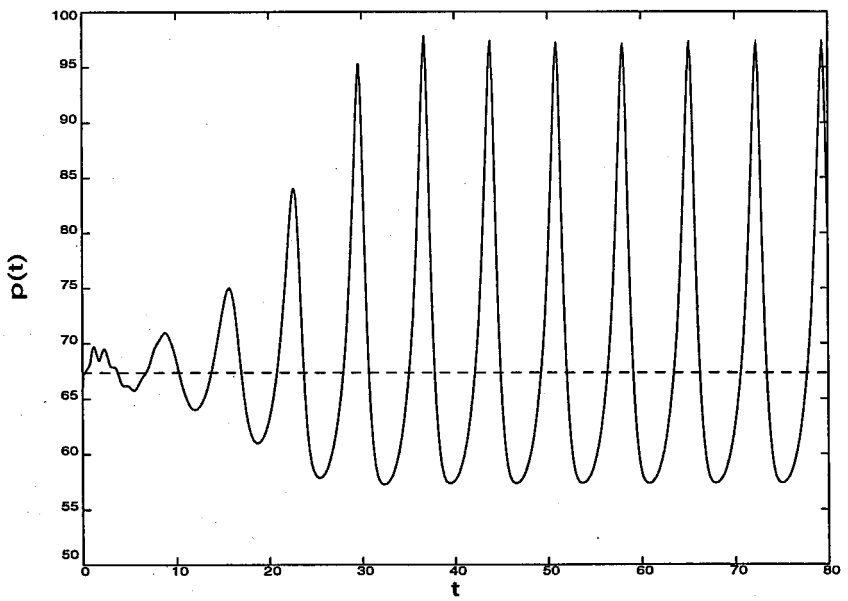

FIG.2.3a Time history of the shock pressure for a detonation with an overdrive factor, $f = 1.60$. Resolution, $20\,\text{pts}/L_{1/2}$. Horizontal line represents ZND solution.

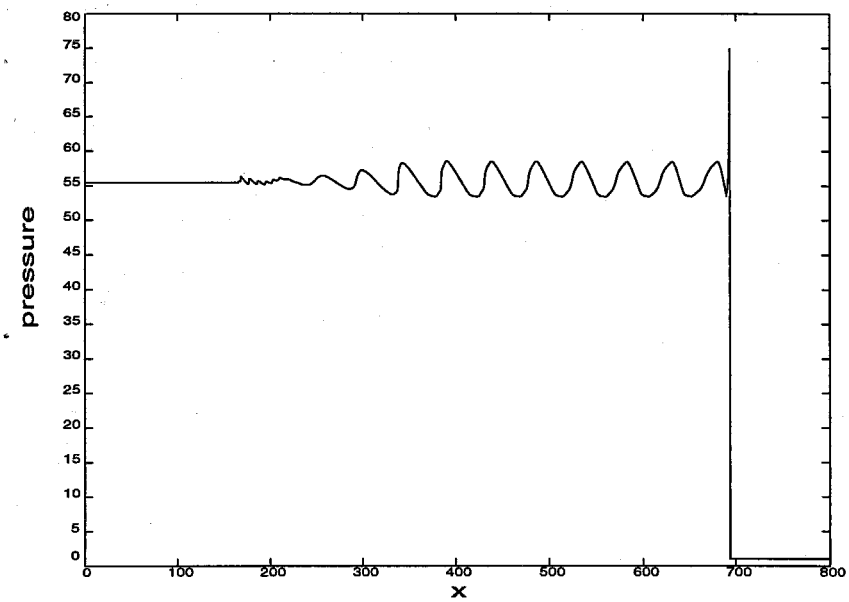

FIG.2.3b Spatial profile of the pressure for a detonation with an overdrive factor, $f = 1.60$, at $t = 80.0$. Resolution, $20\,\text{pts}/L_{1/2}$.

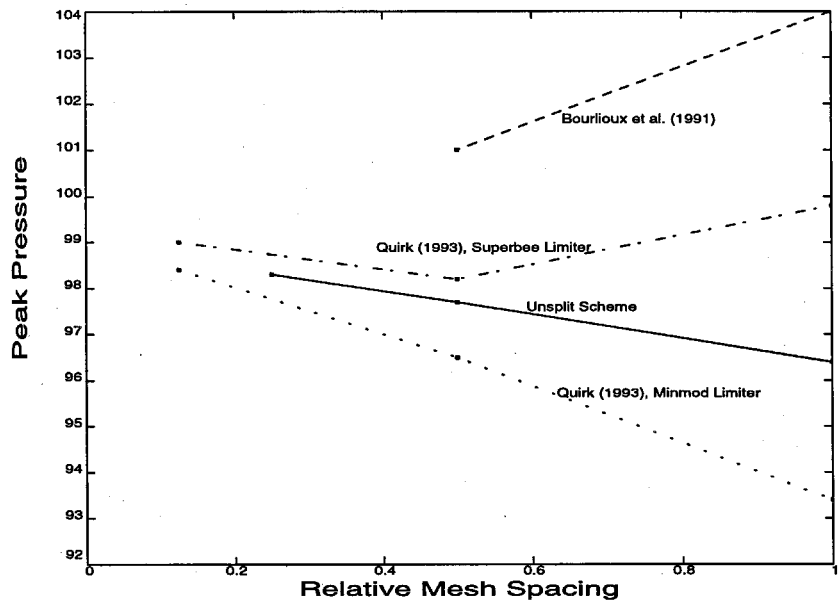

FIG.2.3c Variation of peak pressure with grid resolution for various schemes. Detonation with overdrive factor $f = 1.60$.

Subsequently, numerical results are obtained for lower overdrive factors, namely $f = 1.40$ and $f = 1.34$. For $f = 1.40$, the parameters are $D = 8.06$, and $K = 411.98$. Linear-stability analysis predicts two unstable modes. The shock pressure history, which exhibits a period-doubling oscillation, is presented in Fig. 2.4a. The spatial profile of pressure at $t = 100.0$ is presented in Fig. 2.4b.

For $f = 1.34$, the parameters of the problem are $D = 7.88$ and $K = 504.91$. This is a case of three unstable modes, according to linear-stability analysis. The shock pressure history and the spatial profile of the pressure at $t = 100$ are presented in Figs. 2.5. The results for both overdrive factors are obtained with a resolution of $40\,\mathrm{pts}/L_{1/2}$. Numerical simulations with higher resolution produce the same results in both cases.

The overdrive factor is lowered further, to a value of $f = 1.30$. The shock speed and stiffness coefficient for this detonation are $D = 7.764$, and $K = 583.71$. Linear-stability analysis suggests three unstable modes for this case. Bourlioux *et al.* (1991) proposed the existence of chaotic-pulsation instabilities because they observed a sensitive dependence of the results on the initial data, as is characteristic of chaotic systems with a small number (greater-than or equal-to 3) of degrees of freedom, *e.g.*, Nicolis (1995). Specifically, they observed that slightly-perturbed initial data produced results that were qualitatively similar but quantitatively different.

Similar behavior is demonstrated in the present study in simulations performed using the unsplit scheme. This can be verified by comparing the shock pressure history of unperturbed initial profiles, as presented in Fig. 2.6a, with the pressure history of perturbed initial profiles in Fig. 2.6b. To perform these simulations, a perturbation is added to the ZND profiles of the fluid-dynamic variables given by a sinusoidal wave of amplitude 0.1% of the values behind the shock, with wavelength set to unity.

Numerical simulations using high-order algorithms for even lower overdrive factors had not been published until recently. Linear stability predicts an increased number of unstable modes as f decreases. He & Lee (1995) presented results obtained by a split algorithm, for overdrive factors as low as $f = 1.10$. For this case, which corresponds to a shock speed of $D = 7.1418$ and a stiffness coefficient $K = 1389.58$, they found that the initial perturbations die out, that the post-shock

values of the variables become steady, and that the reaction front lags behind the hydrodynamic shock at an ever-increasing distance (quenched detonation). They attempted a connection between the detonation quenching they observed and linear-stability analysis, noting that, at $f = 1.165$, the imaginary part of the first eigenvalue becomes zero. Linear-stability analysis, however, is helpful for overdrives close to f^* and not for overdrives close to unity.

Furthermore, this system of equations can not produce a quenched detonation at large times. This is because of the phenomenon of thermal runaway: the reaction front stays temporarily behind the main shock and the temperature in the area between the reaction front and the shock is low. In this area, therefore, the source term on the right-hand side of the species equation is exponentially small. The process in that region can be described as homogeneous combustion, *i.e.*, after some time, the source term becomes large and a rapid explosion takes place, resulting in high combustion spikes.

An *underresolved* simulation for $f = 1.10$ is presented in Fig 2.7a. The proposed unsplit scheme is used, with a resolution of $15\,\mathrm{pts}/L_{1/2}$. The result is in agreement with the result of He & Lee (1995), obtained with a mesh of $50\,\mathrm{pts}/L_{1/2}$, up to $t = 60.0$ (it is at that time that He & Lee stopped their simulation). The high rise of the shock pressure that occurs at time $t \simeq 65.0$ is due to the phenomenon of thermal runaway discussed above.

When the resolution is increased in the current simulations, a dramatic change takes place (see Fig. 2.7b). The temporal profile of the shock pressure becomes irregular, with no evident structure. At $t \simeq 8.0$, the shock pressure drops to a value around $p \simeq 27.0$. The temperature at this point is around $T \simeq 3.4$, which is indeed too low to initiate and sustain the chemical reaction. Consequently, the reaction front is convected by the flow and stays behind the hydrodynamic shock.

In the region between the reaction front and the shock, however, the temperature is not constant. It can be verified that there are small pockets of material with higher temperature (see Fig. 2.8a). Recall that the initial fluctuations in the shock pressure produced shock waves that travelled upstream (they can be seen in Fig. 2.8). These waves interacted with each other and some reflected back, travelled downstream, and created the temperature gradients in the region discussed above.

Higher-temperature points are responsible for chemical-reaction initiation. The area between the initial reaction front and the hot spot remains inert. It develops to a pocket of unreacted material as soon as the hot spot has burnt completely.

In the beginning, the reaction inside the pocket is slow because the source term in the species equation is still exponentially small. This early stage of the combustion can be considered as a constant-pressure process. When the source term becomes larger, a relatively-rapid explosion occurs. During this stage of combustion, the density is initially almost constant (for inertial reasons) with the temperature rise producing a large pressure rise. This pressure rise produces two shock waves, one travelling downstream and one upstream. The downstream shock wave catches up with the main shock. The time required for this to take place can be estimated by the shock-pressure history; Fig. 2.7b. In this figure, the sudden jumps in shock pressure, at time up to $t \simeq 55.0$, correspond to the overtakings of the main front by shocks produced during earlier explosions. The increase of the shock pressure restarts the detonation process behind the shock, until it drops again to a value $p \simeq 27.0$. The shock wave that propagates upstream causes the explosion of the pocket of unreacted material. This second explosion gives birth to a second pair of shock waves. Spatial profiles of the flow variables during such an explosion are given in Figs. 2.9.

This process repeats itself, until $t \simeq 55.0$, when the explosions become large. After that, the detonation oscillates in an irregular way and appears to correspond to the situation termed "spatial and temporal chaos", *e.g.*, Nicolis (1995). Resolutions up to $250\,\text{pts.}/L_{1/2}$ are used for this case. It is observed that resolutions finer than $15\,\text{pts}/L_{1/2}$ produce qualitatively-similar, but quantitatively-different, results at large times. In such highly-unstable cases, different resolutions are equivalent to different initial conditions. Further numerical investigations, with much higher resolutions, may be required for a definitive conclusion, even though the present numerical evidence indicates clearly that the detonation does not quench and that the system exhibits chaotic behavior for $f = 1.10$.

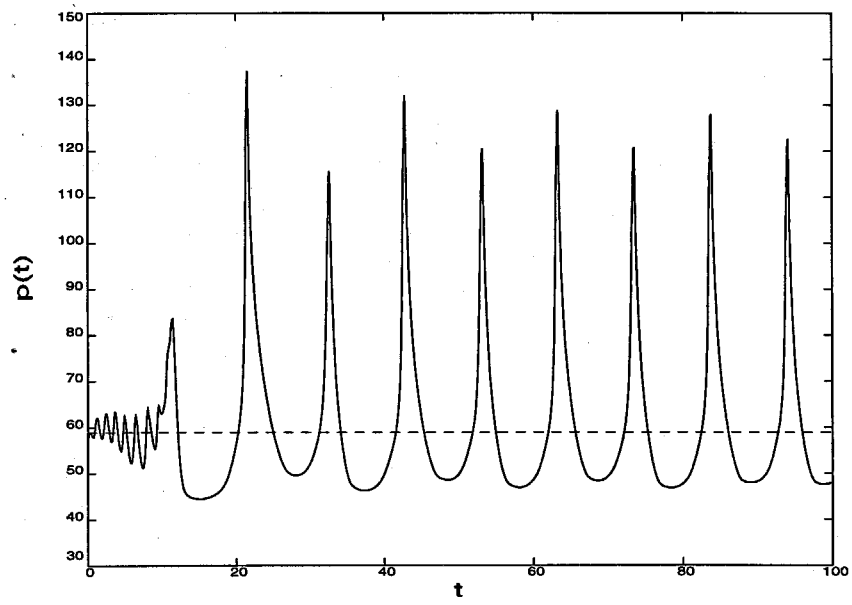

FIG.2.4a Time history of the shock pressure for a detonation with an overdrive factor, $f = 1.40$. Resolution, 20 pts/$L_{1/2}$. Horizontal line represents ZND solution.

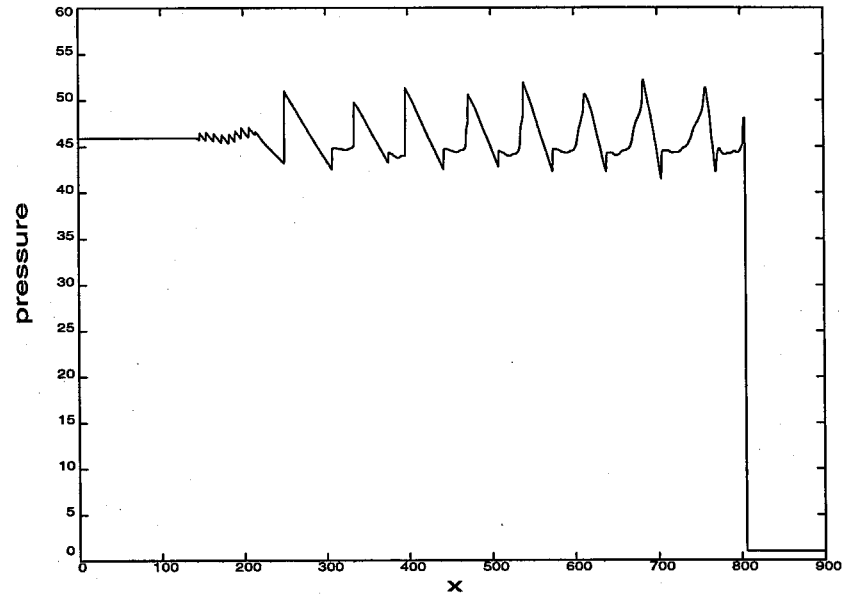

FIG.2.4b Spatial profile of the pressure for a detonation with an overdrive factor, $f = 1.40$, at $t = 100.0$. Resolution, 20 pts/$L_{1/2}$.

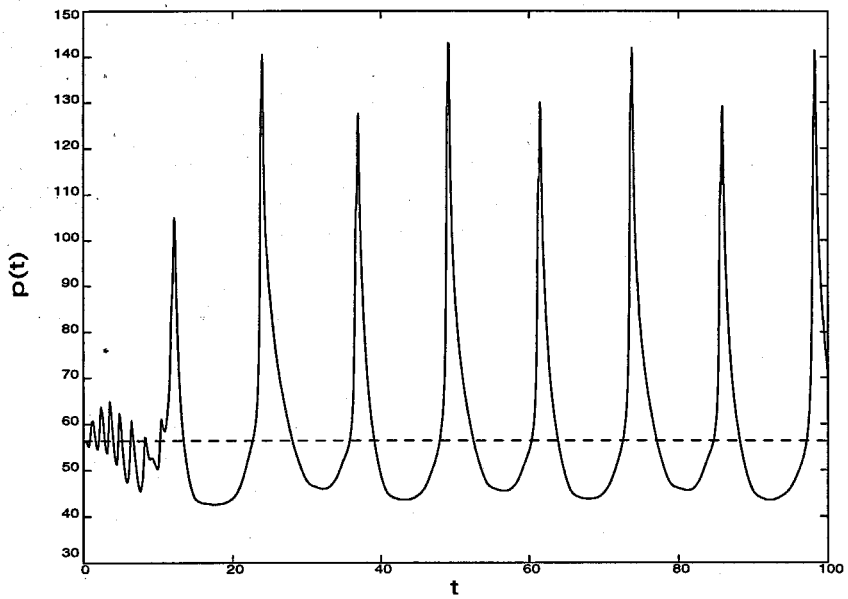

FIG.2.5a Time history of the shock pressure for a detonation with an overdrive factor, $f = 1.34$. Resolution, $20\,\mathrm{pts}/L_{1/2}$. Horizontal line represents ZND solution.

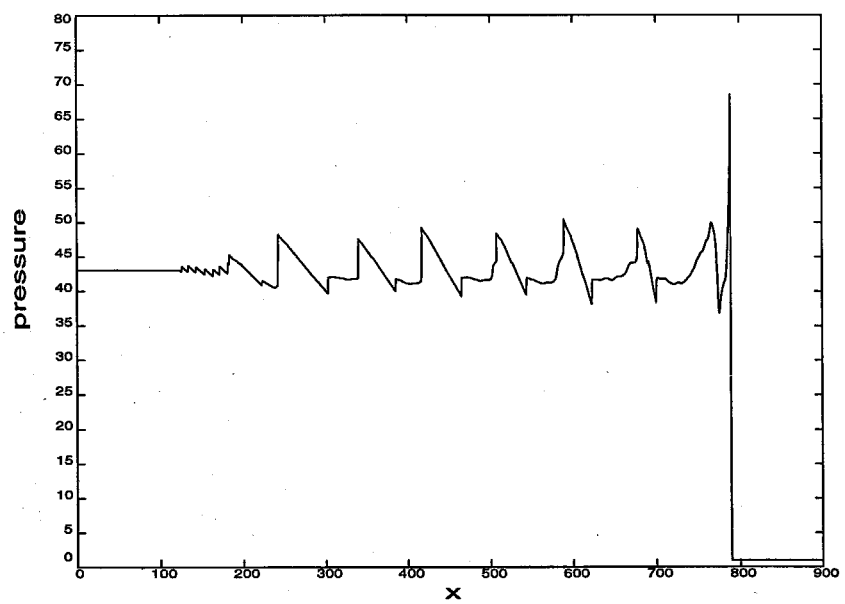

FIG.2.5b Spatial profile of the pressure for a detonation with an overdrive factor, $f = 1.34$, at $t = 100.0$. Resolution, $20\,\mathrm{pts}/L_{1/2}$.

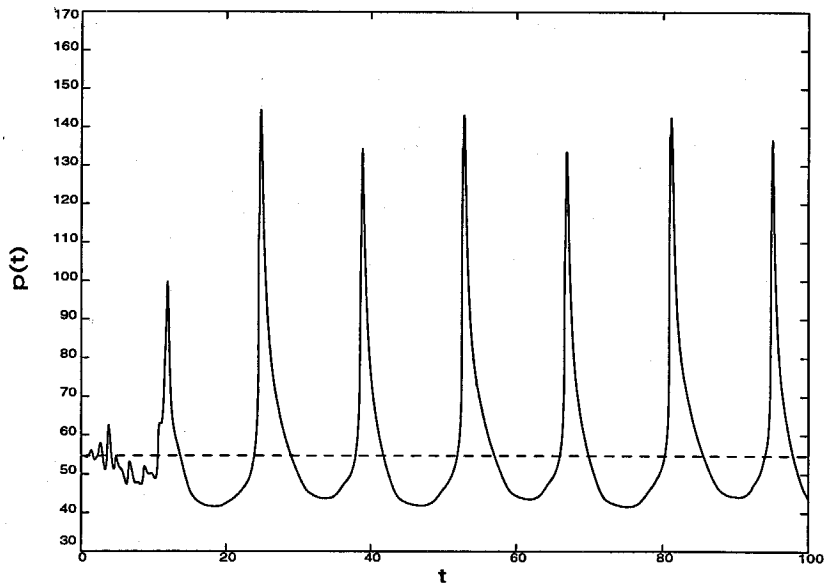

FIG.2.6a Time history of the shock pressure for a detonation with an overdrive factor, $f = 1.30$. Resolution, $80\,\text{pts}/L_{1/2}$. Horizontal line represents ZND solution.

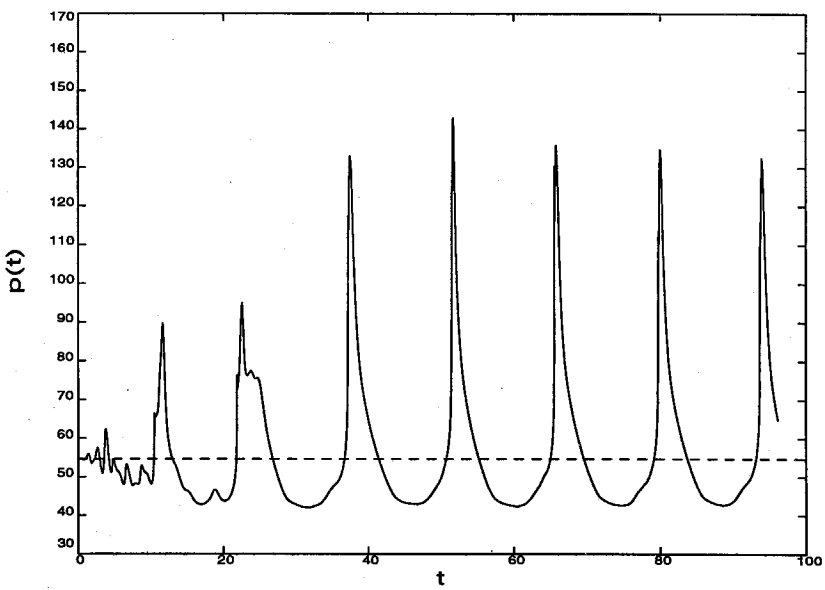

FIG.2.6b Time history of the shock pressure for a detonation with an overdrive factor, $f = 1.30$, and perturbed initial data. Resolution, $80\,\text{pts}/L_{1/2}$. Horizontal line represents ZND solution.

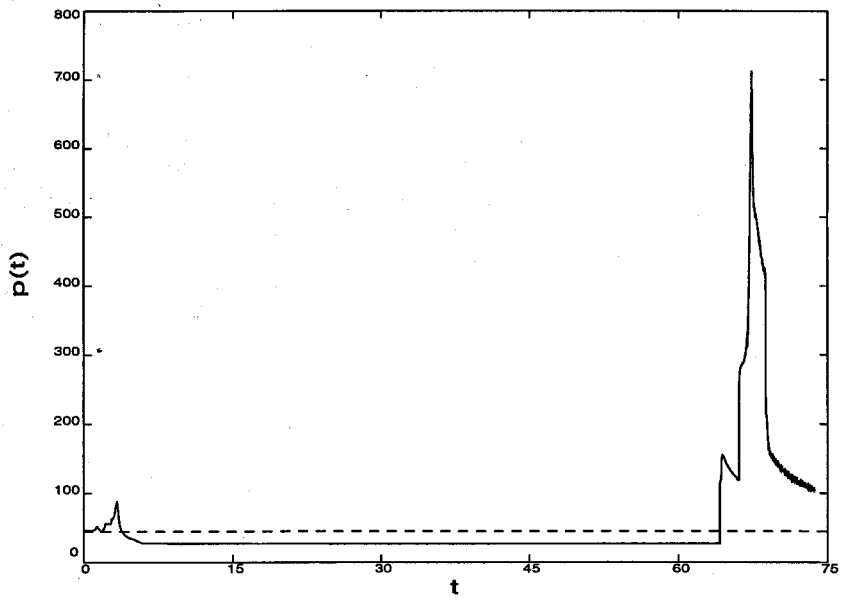

FIG.2.7a Time history of the shock pressure for a detonation with an overdrive factor, $f = 1.10$. Resolution, 15 pts/$L_{1/2}$. Horizontal line represents ZND solution.

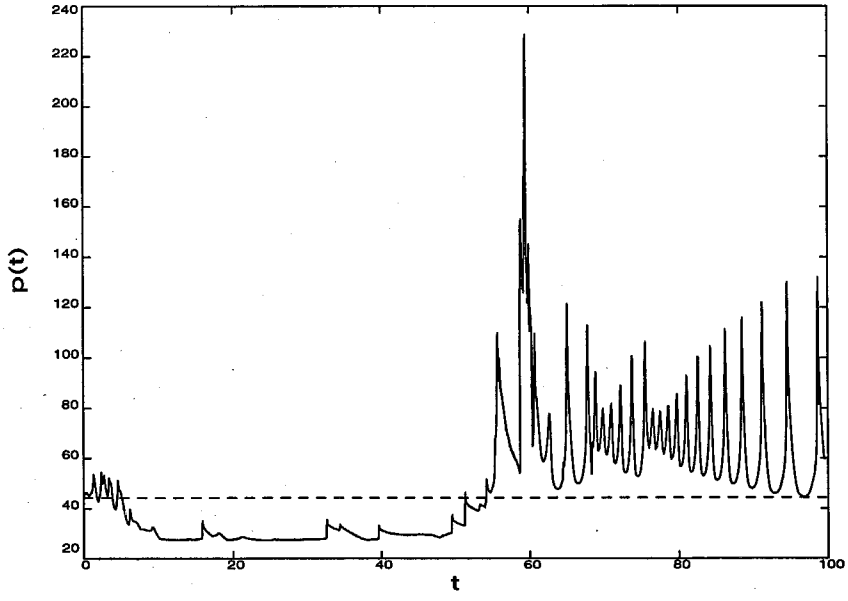

FIG.2.7b Time history of the shock pressure for a detonation with an overdrive factor, $f = 1.10$. Resolution, 50 pts/$L_{1/2}$. Horizontal line represents ZND solution.

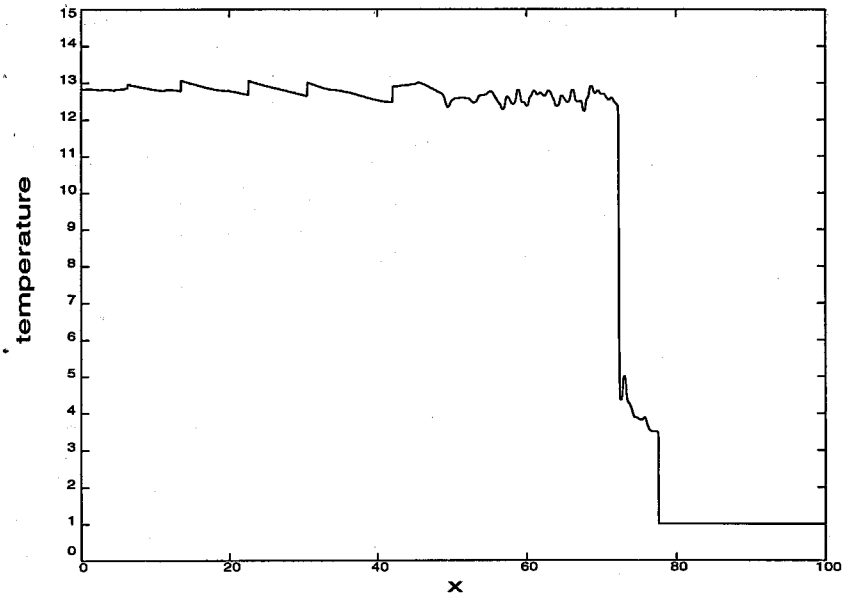

FIG.2.8a Spatial profile of the temperature for a detonation with an overdrive factor, $f = 1.10$, at $t = 12.0$. Resolution, $50\,\text{pts}/L_{1/2}$.

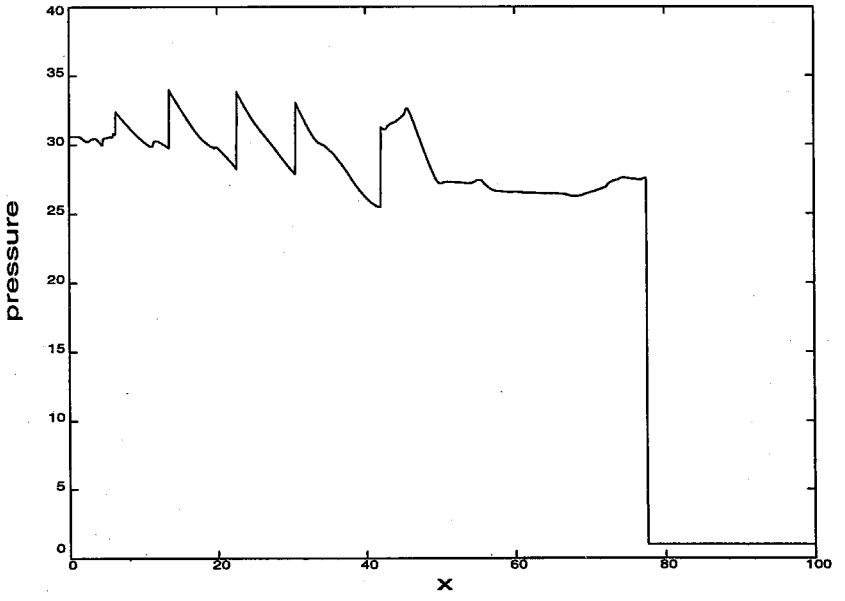

FIG.2.8b Spatial profile of the pressure for a detonation with an overdrive factor, $f = 1.10$, at $t = 12.0$. Resolution, $50\,\text{pts}/L_{1/2}$.

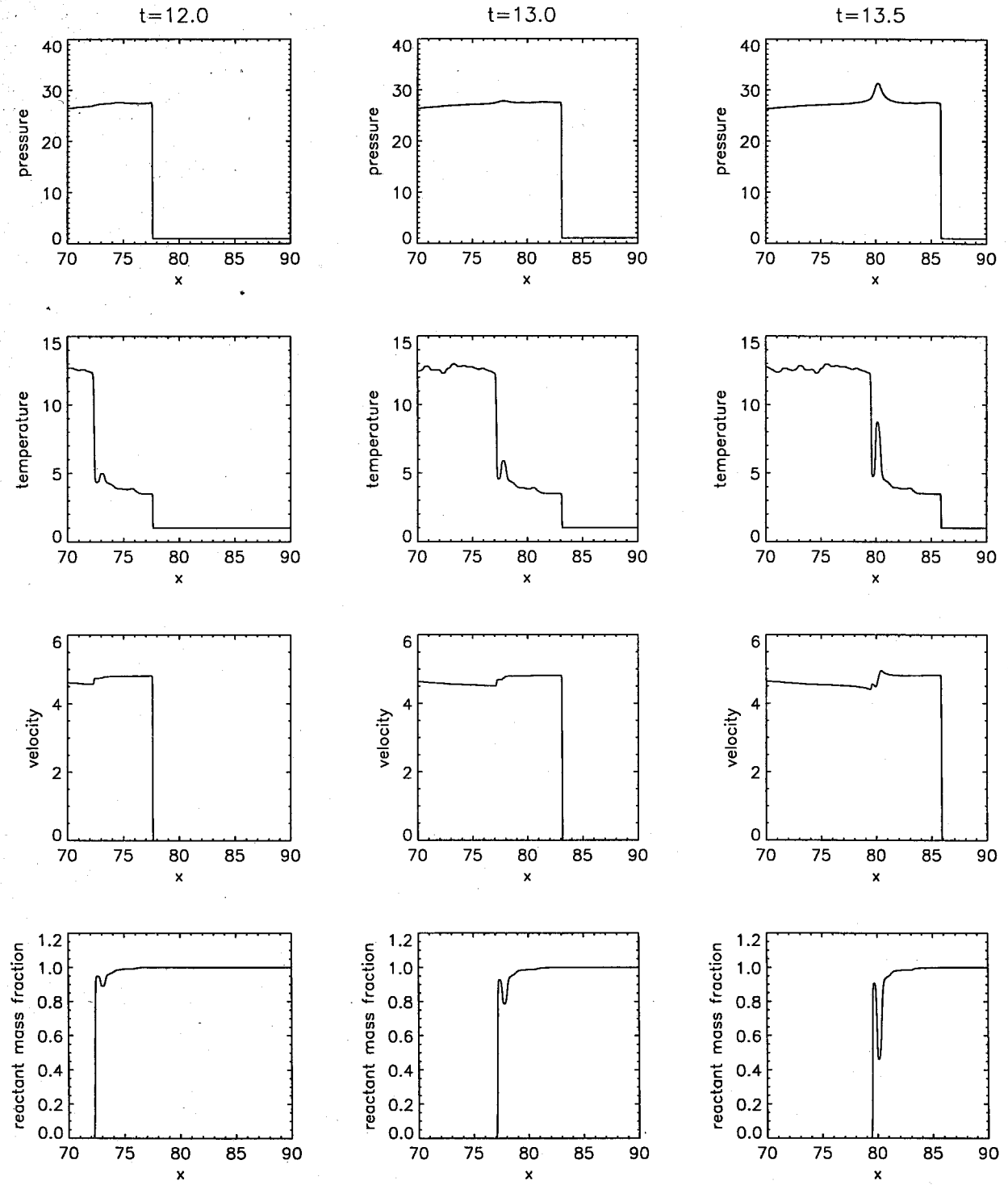

FIG.2.9a Spatial profiles of the flow variables at the area of an explosion, for a detonation with overdrive factor, $f = 1.10$. Profiles at $t = 12.0$, 13.0, 13.5. Resolution, $50\,\text{pts}/L_{1/2}$.

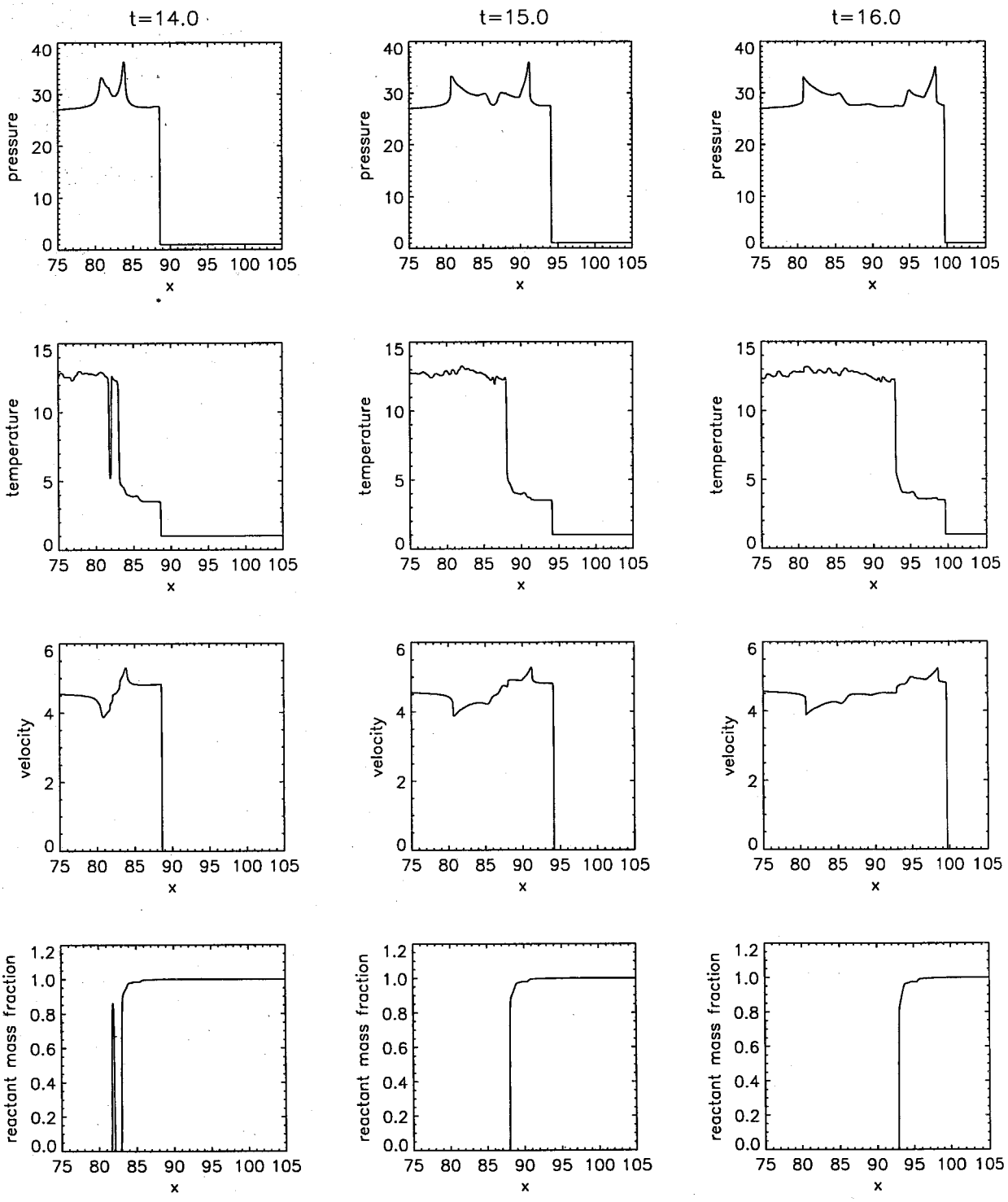

FIG.2.9b Spatial profiles of the flow variables at the area of an explosion, for a detonation with an overdrive factor, $f = 1.10$. Profiles at $t = 14.0$, 15.0, 16.0. Resolution, 50 pts/$L_{1/2}$.

2.5 Concluding Remarks

A new approach for evolving hyperbolic systems with source terms in one space dimension has been presented. Performing the decomposition of the equations to a set of scalar fields along selected curves in space-time, it is possible to identify associated invariants along these curves that permit the construction of unsplit algorithms for the numerical integration of these laws.

The proposed scheme was tested on a scalar conservation law with a non-linear source term, and on the one-dimensional compressible Euler equations for reacting flows. The scheme is found to be accurate and robust. In the scalar case, increased stiffness may, depending on the initial data, produce continuous solutions with high propagation velocities. Unless the computational grid is sufficiently resolved, these velocities may not be captured correctly with explicit schemes. Overall, the proposed unsplit scheme is more accurate than the equivalent split version.

In the case of reacting flows, useful insight for the evolution of detonations in the unstable regime was obtained. The question of the long-time behavior of detonations near the CJ point is still open. Results obtained by the present scheme indicate chaotic behavior of the system, in contrast with recent previous predictions.

An advantage of the new approach is that it can be generalized to multidimensional flows, in a straightforward way. The system of conservation laws can be decomposed to a set of homogeneous ODE's, as in the one-dimensional case, that hold along selected manifolds in (x, y, t) space. The study of the geometry of these manifolds and the design of unsplit multi-dimensional algorithms is the subject of the following chapter.

CHAPTER 3

Unsplit Schemes for Multi-Dimensional Hyperbolic Systems

Considerable amount of work had been devoted to the study of systems of hyperbolic conservation laws in the past. Most of the effort was focused in systems with two independent variables. These variables were, usually, time and a space variable. As a result of this effort, it became possible to establish existence and uniqueness of weak solutions for such systems and to derive important properties of these solutions, such as their asymptotic behavior. It also became possible to construct accurate algorithms for the numerical approximation of these solutions. The concepts of characteristics and Riemann invariants played a significant role in both the derivation of these theoretical results, and the design of stable and accurate numerical algorithms.

The extension, however, of these theoretical results to systems with more than two independent variables has not been successful. The extremely complicated topology of the discontinuous solutions admitted by such systems has not allowed, so far, the development of global existence theories. Furthermore, the design of numerical schemes for multi-dimensional problems that share the same properties as the equivalent one-dimensional schemes, has not been straightforward. As a consequence, numerical schemes that have been devised consist practically of a patch of one-dimensional computations on each spatial dimension.

The problems arising in the computational efforts of hyperbolic conservation laws with source terms are more complicated, because of the presence of a large number of spatial and temporal scales. Additionally, the source terms are stiff for most applications, and this makes the integration of the equations even more difficult. The conventional approach for solving such systems is to introduce time-splitting for the source terms, *i.e.*, integration of the source term in an intermediate time-step, in addition to dimensional splitting.

Recently, Lappas *et al.* (1995) proposed a way to avoid dimensional splitting for systems of multi-dimensional homogeneous laws. They introduced a family of space-time manifolds, dubbed as *Riemann Invariant Manifolds* along which the system of equations can be decomposed into the characteristic ODE's for the corresponding one-dimensional case. This particular decomposition was employed in the upwinding step of an unsplit, MUSCL-type scheme. This idea was also used in the previous chapters of the present work to design unsplit algorithms for the numerical solution of one-dimensional equations with source terms. In this chapter, this decomposition is employed to systems of equations in two space dimensions. The proposed algorithm is an unsplit, multi-dimensional scheme. Neither time-splitting nor dimensional splitting is performed. In Chapter 4, this algorithm will be used for the numerical simulation of unsteady, two-dimensional detonations.

3.1 First-Order, Quasi-Linear Hyperbolic Systems

A brief review of the theory of hyperbolic systems is given in this section in order to provide the necessary background for the material that follows. Consider the euclidean space-time of N spatial dimensions, $t \times \Re^N$, and the following system of M equations, satisfied at each point, $(t, \mathbf{x}) = (t, x_1, \ldots, x_N)$ of $t \times \Re^N$:

$$\frac{\partial \mathbf{U}}{\partial t} + A_j(\mathbf{U}) \frac{\partial \mathbf{U}}{\partial x_j} = \mathbf{G}\,, \qquad j = 1, \ldots, N\,. \tag{3.1}$$

For this system of quasilinear equations, $\mathbf{U}(t, \mathbf{x}) = [u_1(t, \mathbf{x}), \ldots, u_M(t, \mathbf{x})]$ is the solution vector, and $\mathbf{G}(\mathbf{U}, t, \mathbf{x}) = [g_1(\mathbf{U}, t, \mathbf{x}), \ldots, g_M(\mathbf{U}, t, \mathbf{x})]$ is the vector of the source terms. $A_j(\mathbf{U})$, $j = 1, \ldots, N$, are $M \times M$ matrices. Summation notation is implied for repeated indices.

The Cauchy initial value problem for this system amounts to specifying initial data (referred to as *Cauchy data*) at points on some initial N-dimensional submanifold of $t \times \Re^N$, $\mathcal{S}$, and determining $\mathbf{U}$ that satisfies (3.1) off this manifold. The idea behind the hyperbolicity of a quasi-linear system is that the Cauchy problem be well-posed for it, that is there exists unique solution that depends continuously on the data specified on $\mathcal{S}$. It is interesting to see how the terms of the system (3.1) can be rearranged so that the derivative of $\mathbf{U}$ normal to $\mathcal{S}$ (exterior derivative) can be expressed in terms of the Cauchy data and its derivatives in $\mathcal{S}$ (interior derivatives).

The way to do this is to consider a coordinate transformation and replace $(t, \mathbf{x})$ by a new vector, $\boldsymbol{\phi} = [\phi_0, \ldots, \phi_N]$. The components $\phi_i(t, \mathbf{x})$, $i = 0, \ldots, N$, are assumed to be differentiable functions of their arguments. Keep the variable t unchanged, *i.e.*, $\phi_0 = t$, and assume that the manifold $\mathcal{S}$ is associated with one particular coordinate, say ϕ_N. The following equation is then used to define the manifold $\mathcal{S}$:

$$\phi_N(t, \mathbf{x}) \; = \; 0 \, . \tag{3.2}$$

The other coordinates $\phi_i(t, \mathbf{x})$, $i = 1, \ldots, N-1$, can be selected arbitrarily, provided that the Jacobian of the coordinate transformation,

$$J \; = \; \frac{\partial(t, x_1, \ldots, x_N)}{\partial(\phi_0, \ldots, \phi_N)} \, , \tag{3.3}$$

is non-vanishing at the points of interest, *i.e.*, in the vicinity of $\mathcal{S}$. Then the system (3.1) becomes

$$\left(I \frac{\partial \phi_N}{\partial t} + A_j \frac{\partial \phi_N}{\partial x_j} \right) \frac{\partial \mathbf{U}}{\partial \phi_N} + \left(I \frac{\partial \phi_i}{\partial t} + A_j \frac{\partial \phi_i}{\partial x_j} \right) \frac{\partial \mathbf{U}}{\partial \phi_i} + \; = \; \mathbf{G}(\mathbf{U}, t, \mathbf{x}) \, . \tag{3.4}$$

By making the substitutions

$$\begin{aligned} \boldsymbol{\Lambda} &\equiv I \, \frac{\partial \phi_N}{\partial t} + A_j \frac{\partial \phi_N}{\partial x_j} \, , \\ \mathbf{R} &\equiv \left(I \, \frac{\partial \phi_i}{\partial t} + A_j \frac{\partial \phi_i}{\partial x_j} \right) \frac{\partial \mathbf{U}}{\partial \phi_i} \; - \; \mathbf{G} \, , \end{aligned} \tag{3.5}$$

the system (3.4) yields:

$$\boldsymbol{\Lambda} \, \frac{\partial \mathbf{U}}{\partial \phi_N} + \mathbf{R} \; = \; \mathbf{0} \, . \tag{3.6}$$

In the equations above, and throughout this section, repeated index j implies summation from 1 to N and repeated index i implies summation from 0 to $N-1$.

Given Cauchy data on $\mathcal{S}$, all the tangential derivatives

$$\frac{\partial \mathbf{U}}{\partial \phi_i} \, , \qquad i = 0, \ldots, N-1 \, ,$$

are known. Only the $\mathcal{S}$-normal derivative, *i.e.*, the exterior derivative, is not known. It can be evaluated, however, by equation (3.6) provided that $\boldsymbol{\Lambda}^{-1}$ exists. This condition implies that the following relation must hold on a given point P of $\mathcal{S}$:

$$Q(P; \mathbf{n}, \lambda) \; \equiv \; det(\boldsymbol{\Lambda}) \; \neq \; 0. \tag{3.7}$$

Furthermore, let $\nabla\phi_N$ be the spatial gradient of ϕ_N and define

$$\lambda \equiv \frac{-\partial\phi_N/\partial t}{|\nabla\phi_N|}\,, \qquad \mathbf{n} \equiv \frac{\nabla\phi_N}{|\nabla\phi_N|}\,. \tag{3.8}$$

Substituting in the expression for $Q(P;\mathbf{n},\lambda)$, one finds that

$$Q(P;\mathbf{n},\lambda) \;=\; det(-\lambda I + n_j A_j)\,. \tag{3.9}$$

The expression (3.9) is a homogeneous polynomial of degree M in the quantities $(\lambda, n_1, \ldots, n_N)$, and a first-order differential equation for $\phi_N(t,\mathbf{x})$.

The surfaces along which this polynomial equals zero are called *characteristic* surfaces. The normal derivative of the solution can not be determined along these surfaces. Therefore, a discontinuity of this (or a higher-order) derivative, is possible. Consequently, one can define the characteristic surfaces as surfaces across which discontinuities of the derivatives of the solution can be present. The differential equation that holds on a particular characteristic surface can be found by taking the inner product of the original system with the appropriate left eigenvector $\mathbf{l}_k$,

$$\mathbf{l}_k \cdot \frac{\partial \mathbf{U}}{\partial t} + \mathbf{l}_k \cdot \left(A_j \frac{\partial \mathbf{U}}{\partial x_j} - \mathbf{G} \right) \;=\; 0\,, \qquad k = 1, \ldots, M\,. \tag{3.10}$$

The system of first-order, quasi-linear equations (3.1) is defined to be hyperbolic at a point P in the space-time $t \times \Re^N$, if real characteristic surfaces pass through this point. In other words, the system (3.1) is hyperbolic if the zeros λ_k of the polynomial $Q(P;\mathbf{n},\lambda)$ are all real, and if the corresponding right eigenvectors $\mathbf{r}_k$, satisfying

$$(-\lambda_k I + n_j A_j)\,\mathbf{r}_k \;=\; 0\,, \qquad k = 1, \ldots, M\,, \tag{3.11}$$

(no summation on k) span the space E^M. The property of hyperbolicity as formulated above is a local property, and it depends on both the point P and the Cauchy data prescribed initially.

Every curve $\mathbf{x} = \mathbf{x}(t)$ passing through P that lies on a characteristic surface is called characteristic ray, or bicharacteristic, of the original system of equations. Recall that $\phi_N(t,\mathbf{x}) = 0$ on $\mathcal{S}$; therefore,

$$\frac{\mathrm{d}\phi_N(t,\mathbf{x})}{\mathrm{d}t} \;=\; 0 \qquad \text{on } \mathcal{S}\,, \tag{3.12}$$

which, by virtue of (3.8), yields the following relation for the vector tangent to $\mathcal{S}$:

$$\mathbf{n} \cdot \frac{\mathrm{d}\mathbf{x}}{\mathrm{d}t} = \lambda \,. \tag{3.13}$$

This relation serves as a definition of the bicharacteristics. Given the fact that any surface on space-time can be regarded as a wavefront, Whitham (1974), one can deduce the following simple geometric interpretation of the above relation: λ is considered to be the propagation velocity of $\mathcal{S}$ on the direction specified by $\mathbf{n}$. For every possible choice of $\mathbf{n}$, there exists a different bicharacteristic direction. The totality of these directions form the so-called characteristic cone. This cone is tangent to the conoid that is generated by the characteristic rays that pass through P. This conoid is referred to as the ray conoid.

Every non-characteristic surface can be either space-like or time-like. A surface $\mathcal{S}$ is defined to be space-like at a point P, if $\mathbf{\Lambda}$ is positive definite at P; see Fig. 3.1. In such a case, the direction normal to $\mathcal{S}$ at P is inside the ray conoid and is said to be a time-like direction. For example, constant-t hyperplanes are space-like surfaces. Similarly, a surface $\mathcal{S}$ is defined to be time-like at a point P, if $\mathbf{\Lambda}$ is not positive definite at P. In this case, the direction normal to $\mathcal{S}$ at P is outside the conoid and it is said to be a space-like direction.

Existence and uniqueness theorems of classical (continuous) solutions of hyperbolic systems with Cauchy data prescribed on any space-like surface can be found in Courant & Hilbert (1963). These theorems state that the solution $\mathbf{U}$ at a point P is uniquely determined by Cauchy data prescribed on the bounded domain $\mathbf{D}$ that is formed by the intersections of the ray conoid of P with the constant-t hyperplanes. This domain is called *domain of dependence* of the point P.

Characteristic surfaces play a significant role in the proof of these existence and uniqueness theorems. Furthermore, it might happen that the ODE's (3.12) that hold on the characteristic surfaces are integrable and form a convenient set to integrate, either analytically or numerically. The characteristic equations for isentropic, one-dimensional, gasdynamic flow is such an example. But these ODE's are in general non-integrable. In such cases, the characteristic surfaces do not provide any computational advantage against some other surfaces. Another transformation of variables that leads to a more appropriate, for computational purposes, set of ODE's has to be employed. In the following section, such a transformation is applied to the compressible Euler equations of reacting flows in two space dimensions.

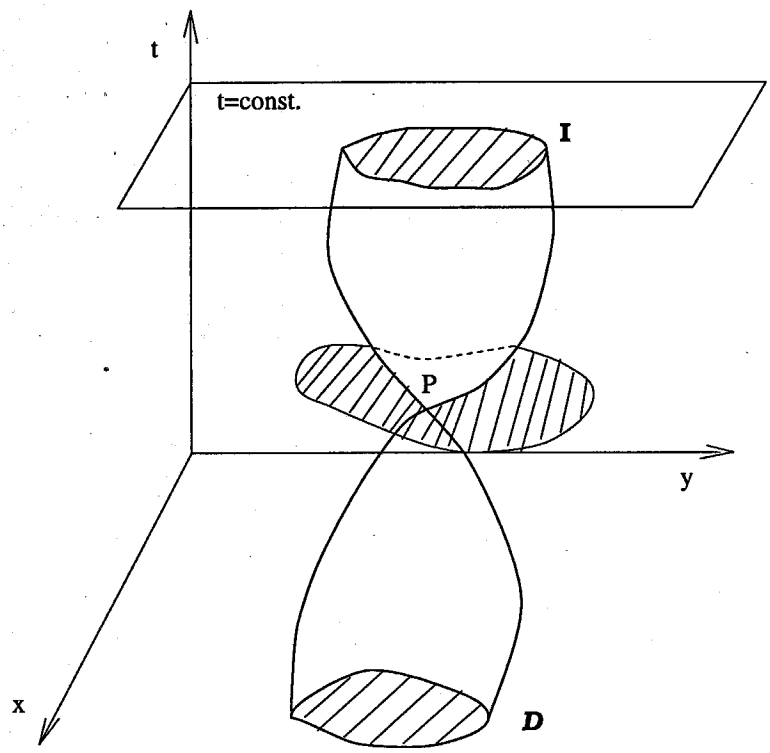

FIG.3.1 The ray conoid through the point P the domain of dependence of the solution at P at an earlier time, and the domain of influence of the solution at P at a later time. The surface element passing through P is space-like.

3.2 Invariant Manifolds of the 2-D Euler Equations for Reacting Flows

Consider a simple model of chemical interaction of two calorically-perfect gases, $A \rightarrow B$, assuming one-step, irreversible, Arrhenius kinetics and absence of dissipation mechanisms. The conservation equations of the reacting system are given by:

$$\frac{\partial \rho}{\partial t} + \nabla \cdot (\rho \mathbf{u}) = 0 \,, \tag{3.14a}$$

$$\frac{\partial \mathbf{u}}{\partial t} + \mathbf{u} \cdot \nabla \mathbf{u} + \frac{1}{\rho} \nabla p = 0 \,, \tag{3.14b}$$

$$\frac{\partial p}{\partial t} + \mathbf{u} \cdot \nabla p + \gamma p \nabla \cdot \mathbf{u} = K q_0 (\gamma - 1) \rho z e^{-E_a/T} \,, \tag{3.14c}$$

$$\frac{\partial z}{\partial t} + \mathbf{u} \cdot \nabla z = -K z e^{-E_a/T} \,. \tag{3.14d}$$

The equation of state of the reacting system is:

$$T = \frac{p}{\rho} . \tag{3.15}$$

In the equations above, $\mathbf{u} = (u, v)$ is the velocity vector and z is the reactant mass fraction, satisfying $0 \leq z \leq 1$. The parameters of the system are:

γ, the specific heat ratio, assumed common for both species,
q_0, the heat-release parameter,
E_a, the activation-energy parameter, and
K, a scaling factor.

In the system under consideration, there are five dependent unknowns, therefore $M = 5$, on a three-dimensional space-time; therefore, $N = 2$.

Assume that the solution is continuous, and consider an arbitrary but fixed spatial unit vector $\mathbf{n} = (n_1, n_2)$. Then, for the system under consideration, the characteristic polynomial gives

$$(\mathbf{u} \cdot \mathbf{n} - \lambda)^3 \left((\mathbf{u} \cdot \mathbf{n} - \lambda)^2 - (a\,|\mathbf{n}|)^2 \right) = 0 , \tag{3.16}$$

where

$$a = \sqrt{\frac{\gamma p}{\rho}} . \tag{3.17}$$

This quantity is usually referred to as the frozen speed of sound. Relation (3.16) yields, in view of (3.8),

$$\left(\frac{\partial \phi_N}{\partial t} + \mathbf{u} \cdot \nabla \phi_N \right)^3 \left(\left(\frac{\partial \phi_N}{\partial t} + \mathbf{u} \cdot \nabla \phi_N \right)^2 - (a\,|\nabla \phi_N|)^2 \right) = 0 . \tag{3.18}$$

The convective manifold defined by the equation

$$\frac{\partial \phi_N}{\partial t} + \mathbf{u} \cdot \nabla \phi_N = 0 , \tag{3.19}$$

has a thre-fold degeneracy. The triple eigenvalue associated with it is $\lambda_{1,2,3} = \mathbf{u} \cdot \mathbf{n}$. The acoustic manifold defined by the equation

$$\frac{\partial \phi_N}{\partial t} + \mathbf{u} \cdot \nabla \phi_N + a\,|\nabla \phi_N| = 0 , \tag{3.20}$$

corresponds to the eigenvalue $\lambda_4 = \mathbf{u}\cdot\mathbf{n} - a$, while the acoustic manifold defined by the equation

$$\frac{\partial \phi_N}{\partial t} + \mathbf{u}\cdot\nabla\phi_N - a\,|\nabla\phi_N| \;=\; 0\,, \tag{3.21}$$

corresponds to the eigenvalue $\lambda_5 \;=\; \mathbf{u}\cdot\mathbf{n} + a$. The left eigenvectors of the system are, respectively,

$$\mathbf{l}_1 \;=\; [0,\, -n_2/n_1,\, 1,\, 0,\, 0]\,, \tag{3.22a}$$

$$\mathbf{l}_2 \;=\; [-a^2,\, 0,\, 0,\, 1,\, 0]\,, \tag{3.22b}$$

$$\mathbf{l}_3 \;=\; [0,\, 0,\, 0,\, 0,\, 1]\,, \tag{3.22c}$$

$$\mathbf{l}_4 \;=\; [0,\, n_1\rho\, a,\, n_2\rho\, a,\, 1,\, 0]\,, \tag{3.22d}$$

$$\mathbf{l}_5 \;=\; [0,\, -n_1\rho\, a,\, -n_2\rho\, a,\, 1,\, 0]\,. \tag{3.22e}$$

By applying (3.10) the original system of equations can be written in the following characteristic form:

$$\frac{\partial}{\partial t}\log(p\rho^{-\gamma}) + \mathbf{u}\cdot\nabla(\log(p\rho^{-\gamma})) \;=\; K\,(\gamma-1)\,q_0\,\rho\,\frac{z}{T}\,e^{-E_a/T}\,, \tag{3.23a}$$

$$\frac{\partial z}{\partial t} + \mathbf{u}\cdot\nabla z \;=\; -K\,z\,e^{-E_a/T}\,, \tag{3.23b}$$

$$\frac{\partial}{\partial t}(\mathbf{u}\cdot\mathbf{n}^{\perp}) + \mathbf{u}\cdot\nabla(\mathbf{u}\cdot\mathbf{n}^{\perp}) \;=\; -\frac{1}{\rho}\nabla p\cdot\mathbf{n}^{\perp}\,, \tag{3.23c}$$

$$\left(\frac{\partial p}{\partial t} + \rho\, a\,\mathbf{n}\cdot\frac{\partial \mathbf{u}}{\partial t}\right) + (\mathbf{u} + a\mathbf{n})\cdot(\nabla p + \rho\, a\,\mathbf{n}\cdot\nabla\mathbf{u}) \;=\; R\,, \tag{3.23d}$$

$$\left(\frac{\partial p}{\partial t} - \rho\, a\,\mathbf{n}\cdot\frac{\partial \mathbf{u}}{\partial t}\right) + (\mathbf{u} - a\mathbf{n})\cdot(\nabla p - \rho\, a\,\mathbf{n}\cdot\nabla\mathbf{u}) \;=\; R\,, \tag{3.23e}$$

where

$$R \;=\; \rho a^2\,[\mathbf{n}\cdot(\nabla\mathbf{u})\mathbf{n} - \nabla\cdot\mathbf{u}] + K\,(\gamma-1)\,q_0\,\rho\,z\,e^{-E_a/T}\,. \tag{3.24}$$

In the equations above, $\mathbf{n}^{\perp}$ stands for the spatial unit vector normal to $\mathbf{n}$. The solution of each of these five equations defines a manifold in $t \times \Re^N$. These are the characteristic manifolds. The integral curves defined by

$$\frac{\mathrm{d}\mathbf{x}}{\mathrm{d}t} = \mathbf{u} \tag{3.25}$$

lie on the first three manifolds, while the integral curves defined by

$$\frac{\mathrm{d}\mathbf{x}}{\mathrm{d}t} = \mathbf{u} + a\mathbf{n} \tag{3.26}$$

and

$$\frac{\mathrm{d}\mathbf{x}}{\mathrm{d}t} = \mathbf{u} - a\mathbf{n} \tag{3.27}$$

lie on the fourth and fifth manifold respectively.

The terms on the right-hand side of equations (3.23) act like forcing terms and do not allow a straightforward extension of the method of characteristics, as used for the one-dimensional Euler equations of gas dynamics. The usual approach in the design of shock-capturing schemes for multi-dimensional flows (with or without chemical source terms) is to fix $\mathbf{n}$ parallel to the grid direction, ignore the velocity component normal to $\mathbf{n}$ and the terms on the right-hand side of the characteristic equations, and finally solve the resulting one-dimensional characteristic problem.

By employing this strategy, however, one essentially disregards information that is coming from other directions. Therefore, integrating equations (3.25), (3.26), and (3.27) that hold along the bicharacteristic directions parallel to the grid does not provide any obvious computational advantage against considering some other direction.

The idea behind the present design of unsplit, multi-dimensional schemes is to find manifolds in space-time along which the equivalent one-dimensional characteristic problem holds. The immediate advantage of using such manifolds is that the characteristic problem can be easily discretized and solved numerically. As a first step towards the construction of such manifolds, one needs to assume that the solution vector is continuous up to first-order derivatives. Then, the convective velocities $\mathbf{u}_0$, $\mathbf{u}_r$, $\mathbf{u}_{\perp}$, $\mathbf{u}_+$, $\mathbf{u}_-$, can be defined so that the following relations are satisfied:

$$\mathbf{u}_0 \cdot \nabla \log(p\rho^{-\gamma}) \;=\; -K\,(\gamma-1)\,q_0\,\frac{z}{T}\,e^{-E_a/T}\,, \tag{3.28a}$$

$$\mathbf{u}_r \cdot \nabla z \;=\; K\,z\,e^{-E_a/T}\,, \tag{3.28b}$$

$$\mathbf{u}_\perp \cdot \nabla(\mathbf{u}\cdot\mathbf{n}^\perp) \;=\; \frac{1}{\rho}\nabla p \cdot \mathbf{n}^\perp\,, \tag{3.28c}$$

$$\mathbf{u}_+ \cdot (\nabla p + \rho\,a\,\mathbf{n}\cdot\nabla\mathbf{u}) \;=\; -R\,, \tag{3.28d}$$

$$\mathbf{u}_- \cdot (\nabla p - \rho\,a\,\mathbf{n}\cdot\nabla\mathbf{u}) \;=\; -R\,. \tag{3.28e}$$

Additionally, consider the manifolds $\mathcal{S}_0$, $\mathcal{S}_+$, $\mathcal{S}_-$, $\mathcal{S}_r$, $\mathcal{S}_\perp$, defined as the integral surfaces of the following equations:

$$\mathcal{S}_0 \;:\quad \frac{\mathrm{D}}{\mathrm{D}t}\log(p\rho^{-\gamma}) \;=\; 0\,, \tag{3.29a}$$

$$\mathcal{S}_r \;:\quad \frac{\mathrm{D}z}{\mathrm{D}t} \;=\; 0\,, \tag{3.29b}$$

$$\mathcal{S}_\perp \;:\quad \frac{\mathrm{D}}{\mathrm{D}t}(\mathbf{u}\cdot\mathbf{n}^\perp) \;=\; 0\,, \tag{3.29c}$$

$$\mathcal{S}_+ \;:\quad \frac{\mathrm{D}p}{\mathrm{D}t} + \rho\,a\frac{\mathrm{D}}{\mathrm{D}t}(\mathbf{u}\cdot\mathbf{n}) \;=\; 0\,, \tag{3.29d}$$

$$\mathcal{S}_- \;:\quad \frac{\mathrm{D}p}{\mathrm{D}t} - \rho\,a\frac{\mathrm{D}}{\mathrm{D}t}(\mathbf{u}\cdot\mathbf{n}) \;=\; 0\,. \tag{3.29e}$$

By combining relations (3.28) and (3.23), it can be verified that the integral curves of the following vector fields lie on the manifolds (3.29):

$$\{(t,\mathbf{x}) \in t\times\Re^N : \frac{\mathrm{d}\mathbf{x}}{\mathrm{d}t} = \mathbf{u}+\mathbf{u}_0\} \in \mathcal{S}_0\,, \tag{3.30a}$$

$$\{(t,\mathbf{x}) \in t\times\Re^N : \frac{\mathrm{d}\mathbf{x}}{\mathrm{d}t} = \mathbf{u}+\mathbf{u}_\mathrm{r}\} \in \mathcal{S}_\mathrm{r}\,, \tag{3.30b}$$

$$\{(t,\mathbf{x}) \in t\times\Re^N : \frac{\mathrm{d}\mathbf{x}}{\mathrm{d}t} = \mathbf{u}+\mathbf{u}_\perp\} \in \mathcal{S}_\perp\,, \tag{3.30c}$$

$$\{(t,\mathbf{x}) \in t\times\Re^N : \frac{\mathrm{d}\mathbf{x}}{\mathrm{d}t} = \mathbf{u}+a\,\mathbf{n}+\mathbf{u}_+\} \in \mathcal{S}_+\,, \tag{3.30d}$$

$$\{(t,\mathbf{x}) \in t\times\Re^N : \frac{\mathrm{d}\mathbf{x}}{\mathrm{d}t} = \mathbf{u}-a\,\mathbf{n}+\mathbf{u}_-\} \in \mathcal{S}_-\,. \tag{3.30e}$$

The convective velocities $\mathbf{u}_0$, $\mathbf{u}_\mathrm{r}$, $\mathbf{u}_\perp$, $\mathbf{u}_+$, $\mathbf{u}_-$, depend locally on the spatial gradients of the flow and are defined through the inner-product relations (3.28). These relations must be regarded as the necessary compatibility conditions for the integral curves given by (3.30) to lie on the corresponding manifolds.

Each of these equations is linear in the components of the corresponding convective velocity. This is because each of the ODE's (3.29) holds on a family of curves that constitutes a two-dimensional space on the three-dimensional euclidean space-time. This space is the manifold associated with the particular ODE. Every curve on this manifold passing through a point P corresponds to a different choice of convective velocity, see Fig. 3.2.

The construction of these manifolds is of local character because it is made under the assumption of a smooth solution vector. The existence of discontinuities in the solution or its derivatives does not allow a global (at-the-large) construction of the five manifolds.

This is not, however, a serious restriction for the numerical integration of the original system of conservation laws under consideration. If a discontinuity is present in the flow-field, each of these manifolds can be defined, and used for computational purposes, on either side of the discontinuity. The presence of shocks is then taken care by supplementing the equations that hold on the curves of the

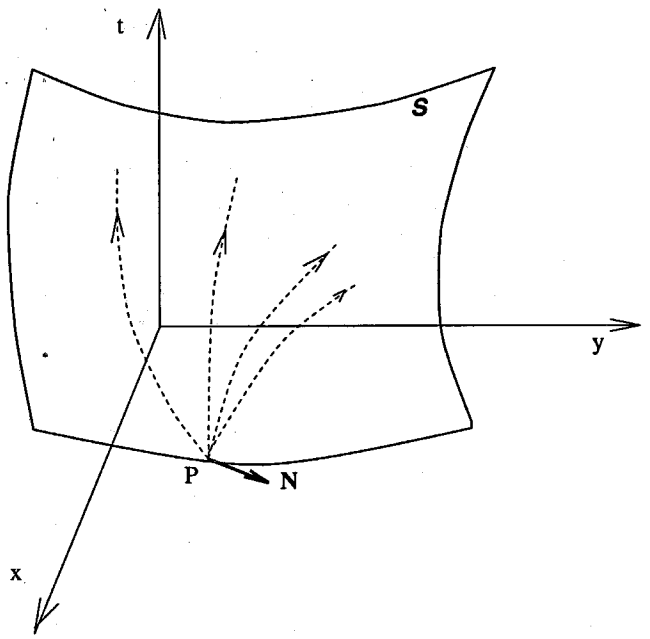

FIG.3.2 An invariant manifold in the three-dimensional space-time. The surface on this picture can be either of the five manifolds defined by (3.29). There is an infinite number of curves passing through a given point P on the surface.

manifolds, with the appropriate jump conditions across the discontinuities. In other words, an appropriate Riemann problem has to be solved. In this case, care must be taken so that not both initial states are taken from the unshocked region, because then the information carried by the manifolds will not propagate through the approaching shock. This methodology is exactly the same as the one used in traditional schemes. In such schemes, it is the bicharacteristic rays that are traced on each side of the discontinuity.

It should be mentioned that even though these manifolds can not be defined globally in the euclidean space-time E^3, one can still study their local geometrical properties. For this purpose, consider a vector $\mathbf{x}$ corresponding to a point $P \in \mathrm{E}^3$ and having components (t, x, y). Let s denote arclength in E^3. The displacement on E^3 is given by

$$\mathrm{d}s \;=\; \sqrt{\mathrm{d}t^2 + \mathrm{d}x^2 + \mathrm{d}y^2}\;. \tag{3.31}$$

Let $\mathcal{S}$ denote any of the five previously-defined manifolds. Let also $\mathbf{c} = (c_1, c_2)$ denote the corresponding convective velocity that represents the velocity of the

manifold $\mathcal{S}$. Finally, let the ODE

$$\frac{\mathrm{D}W}{\mathrm{D}t} = 0 \tag{3.32}$$

denote the one-dimensional characteristic equation which holds on the manifold of interest. For example, if $\mathcal{S} = \mathcal{S}_+$, then $\mathbf{c} = \mathbf{u} + a\,\mathbf{n} + \mathbf{u}_+$ and

$$\frac{\mathrm{D}W}{\mathrm{D}t} = \frac{\mathrm{D}p}{\mathrm{D}t} + \rho\, a \frac{\mathrm{D}}{\mathrm{D}t}(\mathbf{u}\cdot\mathbf{n})\,.$$

A vector $\mathbf{N} \in \mathrm{E}^3$ normal to the manifold is given by

$$\mathbf{N} = [W_t,\, W_x,\, W_y] \frac{1}{\sqrt{W_t^2 + W_x^2 + W_y^2}}\,. \tag{3.33}$$

The following curves lie on S:

$$\begin{aligned} \frac{\mathrm{d}x}{\mathrm{d}t} &= c_1\,, \\ \\ \frac{\mathrm{d}y}{\mathrm{d}t} &= c_2\,, \end{aligned} \tag{3.34}$$

and the displacement on $\mathcal{S}$ is, therefore, given by

$$\mathrm{d}s = \mathrm{d}t\sqrt{1 + c_1^2 + c_2^2}\,. \tag{3.35}$$

The tangent vector at each point on $\mathcal{S}$ is represented by

$$\frac{\mathrm{d}\mathbf{x}}{\mathrm{d}s} = \left[1, \frac{\mathrm{d}x}{\mathrm{d}t}, \frac{\mathrm{d}y}{\mathrm{d}t}\right]\frac{\mathrm{d}t}{\mathrm{d}s} = (1,\, c_1,\, c_2)\frac{1}{\sqrt{1 + c_1^2 + c_2^2}} \tag{3.36}\,.$$

The curvature vector of a curve lying on $\mathcal{S}$ is given by:

$$\mathbf{k} = \frac{\mathrm{d}^2\mathbf{x}}{\mathrm{d}s^2}\,,$$

which, in view of (3.34) and (3.35), produces

$$\mathbf{k} = [A,\, B,\, \Gamma]\frac{1}{(1 + c_1^2 + c_2^2)^2}\,, \tag{3.37}$$

where

$$A \equiv -(\dot{c}_1\, c_1 + \dot{c}_2\, c_2)\,. \tag{3.38a}$$

$$B \equiv (\dot{c}_1 + \dot{c}_1\, c_2^2 - \dot{c}_2\, c_1\, c_2)\,, \tag{3.38b}$$

$$\Gamma \equiv (\dot{c}_2 + \dot{c}_2\, c_1^2 - \dot{c}_1\, c_1\, c_2)\,. \tag{3.38c}$$

In this relation, a dotted quantity represents differentiation along a curve on $\mathcal{S}$. For example,

$$\dot{c_1} = \frac{\mathrm{d}c_1}{\mathrm{d}t} = \frac{\partial c_1}{\partial t} + c_1 \frac{\partial c_1}{\partial x} + c_2 \frac{\partial c_1}{\partial y} .$$

The normal and geodesic curvature vectors, $\mathbf{k}_n$ and $\mathbf{k}_g$ respectively, are given by

$$\mathbf{k}_n = (\mathbf{k} \cdot \mathbf{N})\mathbf{N} , \tag{3.39a}$$

$$\mathbf{k}_g = \mathbf{k} - \mathbf{k}_n . \tag{3.39b}$$

Given these relations, one can get estimates for the curvature of the various curves on the manifold, and use this information to achieve higher-order accuracy. The geodesic curves of the manifold under consideration (that is, the curves whose geodesic curvature is zero) satisfy the following set of equations:

$$A\, W_x = B\, W_t , \tag{3.40a}$$

$$B\, W_y = \Gamma\, W_x . \tag{3.40b}$$

Some numerically useful choices of directions on the manifolds of interest are presented below. Recall that every surface $\phi(t, \mathbf{x}) = 0$ in space-time can be viewed as a wavefront. First, consider the invariant manifold $\mathcal{S}_+$. Let $\mathbf{N}_+$ denote the spatial unit vector normal to this front. Then

$$\mathbf{N}_+ = \frac{\nabla p + \rho a \nabla(\mathbf{u} \cdot \mathbf{n})}{|\nabla p + \rho a \nabla(\mathbf{u} \cdot \mathbf{n})|} . \tag{3.41}$$

$\mathbf{N}_+$ depends on the spatial unit vector $\mathbf{n}$. Actually, there is a class of manifolds $\mathcal{S}_+$, each manifold corresponding to a different choice of $\mathbf{n}$. The unit vector $\mathbf{n}$, which is assumed to be arbitrary but fixed, acts as a "label" for the particular manifold under consideration. In other words, $\mathbf{n}$ is the free parameter of the one-parameter class of manifolds $\mathcal{S}_+$. This is also true for the class of manifolds $\mathcal{S}_-$ and $\mathcal{S}_\perp$. It not true, however, for $\mathcal{S}_0$ and $\mathcal{S}_\mathrm{r}$ because these manifolds do not depend on $\mathbf{n}$; see equations (3.30).

Furthermore, $\mathbf{n}$ gives the spatial direction along which a one-dimensional characteristic problem holds. By keeping $\mathbf{u}_+$ fixed and letting $\mathbf{n}$ rotate a full circle, one gets a conoid of invariant curves passing through the point P. An example of the relative position of this conoid with respect to the ray conoid is given in Fig. 3.3.

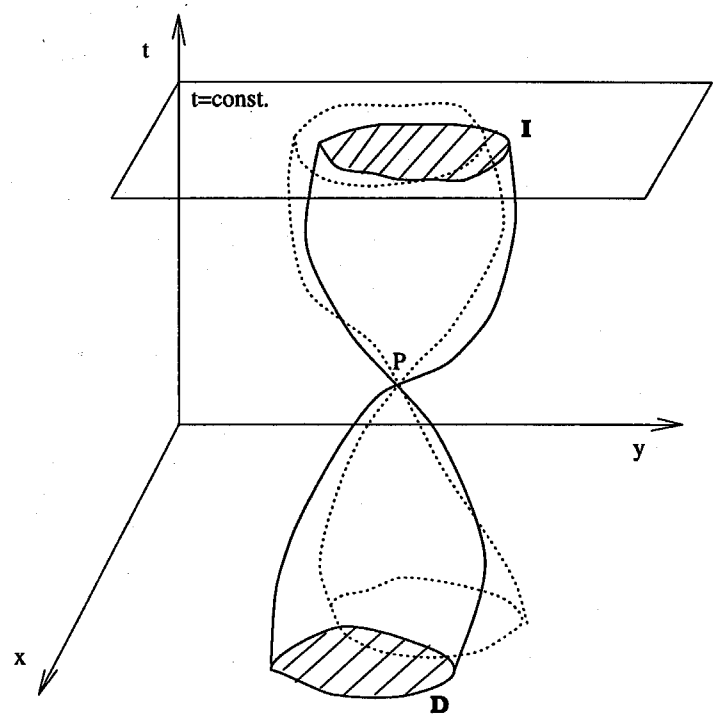

FIG.3.3 Relative position of the invariant conoid formed by the rotation of $\mathbf{n}$, with respect the ray conoid passing through a point P in space-time. The solid line represents the ray conoid, and the dotted line represents the invariant conoid.

The velocity of the front $\mathcal{S}_+$ is given by

$$\mathbf{c}_+ = \mathbf{u} + a\,\mathbf{n} + \mathbf{u}_+ \,. \tag{3.42}$$

A possible choice for $\mathbf{u}_+$ is to seek $|\mathbf{u}_+|_{\min}$. The curve on $\mathcal{S}_+$ that corresponds to this choice is the curve that lies as close to the equivalent bicharacteristic ray as possible. This means that the point of the proposed curve is closer to the intersection of the bicharacteristic ray and the constant-t plane than any other intersection point of the manifold and the constant-t plane. Then

$$\mathbf{u}_+ \;//\; \mathbf{N}_+ \,,$$

and, in fact,

$$\mathbf{u}_+ = \left(\frac{-R}{|\nabla p + \rho a \nabla(\mathbf{u}\cdot\mathbf{n})|}\right)\mathbf{N}_+ \,. \tag{3.43}$$

Another choice would be to try to minimize $|\mathbf{u}_+ + a\mathbf{n}|$, *i.e.*, to consider the curve that is as close as possible to the fluid streamline. In this case

$$(\mathbf{u}_+ + a\mathbf{n}) \;//\; \mathbf{N}_+ \,,$$

and the expression for the convective velocity becomes

$$\mathbf{u}_+ \;=\; \left(a(\mathbf{n}\cdot\mathbf{N}_+) - \frac{R}{|\nabla p + \rho\, a \nabla(\mathbf{u}\cdot\mathbf{n})|} \right) \mathbf{N}_+ - a\mathbf{n}\,. \tag{3.44}$$

Since $\mathbf{u}_+ + a\mathbf{n}$ is parallel to $\mathbf{N}_+$, the velocity of the front $\mathcal{S}_+$ can be written as

$$\mathbf{c}_+ \;=\; \mathbf{u} + aM_+\,\mathbf{N}_+\,. \tag{3.45}$$

In the equation above, the expression for M_+ can be obtained form (3.44). The result is

$$M_+ \;=\; \frac{\mathbf{n}\cdot\nabla p + \rho\, a \nabla\cdot\mathbf{u} - (\gamma-1)\,K\,q_0\,(\rho\, z/a)\,e^{-E_a/T}}{|\nabla p + \rho\, a \nabla(\mathbf{u}\cdot\mathbf{n})|}\,. \tag{3.46}$$

The dimensionless parameter M_+ is a measure of the deviation of the surface-element around the selected curve on the manifold $\mathcal{S}_+$ from the bicharacteristic ray $\mathbf{u} + a\mathbf{n}$. When $|M_+| < 1$ the surface-element is time-like. When $|M_+| > 1$, the surface-element is space-like (and when $|M_+| = 1$, it is characteristic). When the surface-element of $\mathcal{S}_+$ is space-like, it lies outside the domain of dependence of a given point P. At first-sight, this result might look counter-intuitive but it has to do with the fact that knowledge of the local spatial gradients of the flow and their smoothness constitutes additional information about how the initial data are related. This information can propagate with speeds greater than the characteristic speeds, as (3.46) reveals, and can be used for computational purposes; see also relative discussion in Lappas *et al.* (1995).

Most of the information about $\mathcal{S}_+$ is contained in $\mathbf{N}_+$ and M_+, which provide the direction of this manifold and its relative position with respect to the characteristic manifolds. Both of these quantities depend directly on the spatial unit vector $\mathbf{n}$, but this is because of the multi-dimensional character of the problem under consideration.

As mentioned by Lappas *et al.* (1995), the intersection of a manifold in space-time and the local characteristic ray-cone can be examined by considering the projection vector, $\mathbf{V}_p$, of an arbitrary bicharacteristic direction $\hat{\mathbf{n}}$,

$$\mathbf{V}_p \;=\; \mathbf{u} + a\hat{\mathbf{n}}\,, \tag{3.47}$$

on the manifold of interest. For the case of $\mathcal{S}_+$, one can readily find that the projection of a curve $\dot{\mathbf{x}}(t) = \mathbf{W}$ on $\mathcal{S}_+$ is the curve $\dot{\mathbf{x}}(t) = \mathbf{w}_p$ such that the norm $|\mathbf{W} - \mathbf{w}_p|$ attains a minimum. Following the same procedure as in Lappas *et al.* (1995), one observes that this occurs if

$$(\mathbf{W} - \mathbf{w}_p) \;/\!/\; \mathbf{N}_+ \,.$$

If this condition is satisfied, then $\mathbf{W} = \mathbf{V}_p$ and $\mathbf{w}_p = \mathbf{c}_+$. Furthermore, one gets that

$$(\mathbf{W} - \mathbf{w}_p) \;=\; \mathbf{V}_p - \mathbf{c}_+ \;=\; a(\hat{\mathbf{n}} \cdot \mathbf{N}_+ - M_+)\mathbf{N}_+ \,. \tag{3.48}$$

The bicharacteristic ray lies locally on the invariant manifold $\mathcal{S}_+$ if the right-hand side of the above expression becomes zero, *i.e.*, if the following relation is satisfied:

$$M_+ \;=\; \hat{\mathbf{n}} \cdot \mathbf{N}_+ \,. \tag{3.49}$$

This equation admits a solution only if $|M_+| \leq 1$. This condition is satisfied when the surface-element of $\mathcal{S}_+$ lies within the characteristic ray cone. This is because both $\hat{\mathbf{n}}$ and $\mathbf{N}_+$ are unit vectors, which implies that whenever the invariant manifold $\mathcal{S}_+$ is not space-like, there are bicharacteristic directions along which an equivalent one-dimensional problem holds.

Similar relations hold for the invariant manifold $\mathcal{S}_-$. The spatial unit normal to this front is given by

$$\mathbf{N}_- \;=\; \frac{\nabla p - \rho\, a \nabla(\mathbf{u} \cdot \mathbf{n})}{|\nabla p - \rho\, a \nabla(\mathbf{u} \cdot \mathbf{n})|} \,. \tag{3.50}$$

Along the curve of $\mathcal{S}_-$ that lies as close as possible to the equivalent bicharacteristic, the norm $|\mathbf{n}_-|$ attains a minimum. In this case, $\mathbf{u}_- \;/\!/\; \mathbf{N}_-$, and one gets

$$\mathbf{u}_- \;=\; \left(\frac{-R}{|\nabla p - \rho\, a \nabla(\mathbf{u} \cdot \mathbf{n})|} \right) \mathbf{N}_- \,. \tag{3.51}$$

The curve along $\mathcal{S}_-$ that lies as close to the fluid streamline as possible is found by selecting $\mathbf{u}_-$ such that $(\mathbf{u}_- - a\mathbf{n}) \;/\!/\; \mathbf{N}_-$:

$$\mathbf{u}_- \;=\; \left(-a(\mathbf{n} \cdot \mathbf{N}_-) - \frac{R}{|\nabla p - \rho\, a \nabla(\mathbf{u} \cdot \mathbf{n})|} \right) \mathbf{N}_- + a\mathbf{n} \,. \tag{3.52}$$

Given that the velocity of the front is given by

$$\mathbf{c}_- = \mathbf{u} - a\,\mathbf{n} + \mathbf{u}_- ,$$

one gets for the above choice for $\mathbf{u}_-$:

$$\mathbf{c}_- = \mathbf{u} + aM_-\mathbf{N}_- . \tag{3.53}$$

M_- is a dimensionless parameter, similar to M_+, that measures the deviation of the selected curve from the bicharacteristic ray $\mathbf{u} - a\mathbf{n}$. The expression for M_- is

$$M_- = \frac{-\mathbf{n}\cdot\nabla p + \rho a \nabla\cdot\mathbf{u} - (\gamma-1)\,K\,q_0\,(\rho z/a)\,e^{-E_a/T}}{|\nabla p + \rho a \nabla(\mathbf{u}\cdot\mathbf{n})|} . \tag{3.54}$$

As in the case of $\mathcal{S}_+$, a surface-element on $\mathcal{S}_-$ is time-like, characteristic, or space-like, according to whether $|M_-| < 1$, $|M_-| = 1$, or $|M_-| > 1$, respectively. Using arguments similar to the ones employed when $\mathcal{S}_+$ was examined, one can find that the necessary condition for a characteristic curve to lie on $\mathcal{S}_-$ is

$$M_- = \hat{\mathbf{n}}\cdot\mathbf{N}_- . \tag{3.55}$$

It remains to investigate the structure of the invariant manifolds $\mathcal{S}_0, \mathcal{S}_r, \mathcal{S}_\perp$, and determine the curves along these manifolds that can be used for numerical purposes. The spatial unit normal vectors of these manifolds are given by

$$\mathbf{N}_0 = \frac{\nabla p - a^2\nabla\rho}{|\nabla p - a^2\nabla\rho)|} , \tag{3.56a}$$

$$\mathbf{N}_r = \frac{\nabla z}{|\nabla z|} , \tag{3.56b}$$

$$\mathbf{N}_\perp = \frac{\nabla(\mathbf{u}\cdot\mathbf{n}^\perp)}{|\nabla(\mathbf{u}\cdot\mathbf{n}^\perp)|} , \tag{3.56c}$$

respectively. The corresponding front velocities are

$$\mathbf{c}_0 = \mathbf{u} + \mathbf{u}_0 , \tag{3.57a}$$

$$\mathbf{c}_r = \mathbf{u} + \mathbf{u}_r , \tag{3.57b}$$

$$\mathbf{c}_\perp = \mathbf{u} + \mathbf{u}_\perp . \tag{3.57c}$$

As mentioned earlier, the convective velocities $\mathbf{u}_0$, $\mathbf{u}_r$, and $\mathbf{u}_\perp$ need only satisfy the compatibility conditions (3.28). Since each of these conditions are linear equations in the velocity space, a particular choice of a convective velocity represents a curve along the corresponding manifold. It is natural to select the velocities whose norm attain a minimum, *i.e.*, to look for $|\mathbf{u}_0|_{\min}$, $|\mathbf{u}_r|_{\min}$, $|\mathbf{u}_\perp|_{\min}$. Then, one immediately gets

$$\mathbf{u}_0 \,//\, \mathbf{N}_0 \,, \tag{3.58a}$$

$$\mathbf{u}_r \,//\, \mathbf{N}_r \,, \tag{3.58b}$$

$$\mathbf{u}_\perp \,//\, \mathbf{N}_\perp \,. \tag{3.58c}$$

Using relation (3.56), the following expressions are deduced:

$$\mathbf{u}_0 \;=\; -\frac{K\,(\gamma-1)\,q_0\,\rho\,z\,e^{-E_a/T}}{|\nabla p - a^2\nabla\rho|}\,\mathbf{N}_0 \,, \tag{3.59a}$$

$$\mathbf{u}_r \;=\; \frac{K\,z\,e^{-E_a/T}}{|\nabla z|}\,\mathbf{N}_r \,, \tag{3.59b}$$

$$\mathbf{u}_\perp \;=\; \frac{\nabla p\cdot\mathbf{n}^\perp}{\rho\,|\nabla(\mathbf{u}\cdot\mathbf{n}^\perp)|}\,\mathbf{N}_\perp \,. \tag{3.59c}$$

Alternatively, one can introduce dimensionless parameters:

$$M_0 \;\equiv\; \frac{K\,(\gamma-1)\,q_0\,z\,e^{-E_a/T}}{a\,|\nabla p - a^2\nabla\rho|} \,, \tag{3.60a}$$

$$M_r \;\equiv\; \frac{K\,z\,e^{-E_a/T}}{a\,|\nabla z|} \,, \tag{3.60b}$$

$$M_\perp \;\equiv\; \frac{\nabla p\cdot\mathbf{n}^\perp}{\rho\,a\,|\nabla(\mathbf{u}\cdot\mathbf{n}^\perp)|} \,, \tag{3.60c}$$

and express the convective velocities in the following fashion:

$$\mathbf{u}_0 \;=\; -aM_0\mathbf{N}_0 \,, \tag{3.61a}$$

$$\mathbf{u}_r \;=\; aM_r\mathbf{N}_r \,, \tag{3.61b}$$

$$\mathbf{u}_\perp \;=\; aM_\perp\mathbf{N}_\perp \,. \tag{3.61c}$$

As in the case with M_+ and M_-, the parameters M_0, M_r, and $M_\perp$, determine the relative position of the corresponding invariant manifolds with respect to the local ray cone. The manifolds $\mathcal{S}_0$, $\mathcal{S}_r$ and $\mathcal{S}_\perp$, can be locally space-like, or time-like, depending on the values of these parameters.

When one of M_0, M_r, or $M_\perp$ is greater than unity, the corresponding invariant manifold is locally space-like and its surface-element lies outside the domain of dependence of a point P. This fact can be, at first glance, contradictory to the concept of the domain of dependence. Careful consideration, though, shows that no such contradiction exists; see relative discussion above when the manifolds $\mathcal{S}_+$ and $\mathcal{S}_-$ were examined.

The intersection of $\mathcal{S}_0$, $\mathcal{S}_r$, and $\mathcal{S}_\perp$ with the ray cone can be examined in the same way as above, *i.e.*, by considering the projection vector of an arbitrary characteristic direction. Then, one deduces that the following condition has to be satisfied for a characteristic curve to lie on $\mathcal{S}_0$:

$$M_0 = \hat{\mathbf{n}} \cdot \mathbf{N}_0 \,. \tag{3.62}$$

Similarly, if a characteristic curve is to lie on $\mathcal{S}_r$, then the necessary condition is

$$M_r = \hat{\mathbf{n}} \cdot \mathbf{N}_r \,. \tag{3.63}$$

Finally, if a characteristic curve is to lie on $\mathcal{S}_\perp$, then the the necessary condition is

$$M_\perp = \hat{\mathbf{n}} \cdot \mathbf{N}_\perp \,. \tag{3.64}$$

3.3 Description of the Numerical Scheme

The compressible Euler equations for reacting flows (3.14), written in integral form, are:

$$\frac{\mathrm{d}}{\mathrm{d}t}\int_V \rho \, \mathrm{d}V + \int_S \rho \, \mathbf{u} \cdot \mathrm{d}\mathbf{S} = 0 \,, \tag{3.65a}$$

$$\frac{\mathrm{d}}{\mathrm{d}t}\int_V \rho\mathbf{u} \, \mathrm{d}V + \int_S \rho\mathbf{u} \, \mathbf{u} \cdot \mathrm{d}\mathbf{S} + \int_S p \, \mathrm{d}\mathbf{S} = 0 \,, \tag{3.65b}$$

$$\frac{\mathrm{d}}{\mathrm{d}t}\int_V \rho e_t \, \mathrm{d}V + \int_S \rho e_t \, \mathbf{u} \cdot \mathrm{d}\mathbf{S} + \int_S p\mathbf{u} \cdot \mathrm{d}\mathbf{S} = 0 \,, \tag{3.65c}$$

$$\frac{\mathrm{d}}{\mathrm{d}t}\int_V \rho z \, \mathrm{d}V + \int_S \rho z \, \mathbf{u} \cdot \mathrm{d}\mathbf{S} - \int_V \dot{z} \, \rho \, \mathrm{d}V = 0 \,, \tag{3.65d}$$

where the total specific energy, e_t, is given by:

$$e_t = \frac{p}{\rho(\gamma-1)} + q_0 z + \frac{u^2}{2} . \tag{3.66}$$

These equations are written for an arbitrary control volume V whose bounding surface S has zero velocity. The procedure of discretization and numerical evaluation of these integrals at each computational cell is given below.

Consider a simply-connected domain consisting of $N_c \times M_c$ quadrilateral cells of arbitrary shape; see Fig. 3.4. The area of the (i,j) cell is denoted by $\Delta S_{i,j}$, and the coordinates of the center of the cell are denoted by $(x^c_{i,j}, y^c_{i,j})$. The interface between the cells (i,j) and $(i+1,j)$ is denoted by $(i+1/2,j)$. Similarly, the interface between the cells (i,j) and $(i,j+1)$ is denoted by $(i,j+1/2)$. Finally, the unit vector normal to a cell interface is denoted by $\mathbf{n}_s$, and the length of a cell interface is denoted by l.

Linear variation of all variables is assumed in each cell. The generic quantity q is then given by

$$q(i,j) = q_{i,j} + (q_x)_{i,j}\,(x - x^c_{i,j}) + (q_y)_{i,j}\,(y - y^c_{i,j}) , \quad i = 1,\ldots,N_c, \quad j = 1,\ldots,M_c , \tag{3.67}$$

where $q_{i,j}$, the average value of q in the (i,j) cell, is given by

$$q_{i,j} \equiv \frac{1}{\Delta S_{i,j}} \int_{(i,j)} q \, dx dy , \tag{3.68}$$

and $(q_x)_{i,j}, (q_y)_{i,j}$ are the slopes of q in this cell.

Under the assumption of linear variation of q, the slopes are constant; therefore, $q_{i,j}$ becomes the value of q at the center of the cell. The slopes $(q_x)_{i,j}$, $(q_y)_{i,j}$ are evaluated through the divergence theorem. For linear functions, this theorem takes the form:

$$[(q_x)_{i,j}\ , (q_y)_{i,j}]\,\Delta S_{i,j} = (q\mathbf{n}_s\, l)_{i\pm1/2,j} + (q\mathbf{n}_s\, l)_{i,j\pm1/2} . \tag{3.69}$$

In the relation above, q must be evaluated at the center of each cell interface. This is performed with the following procedure.

Assume that q is to be computed at the center of the left interface, and let Δl_i denote the distance between $(x^c_{i,j}, y^c_{i,j})$ and $(x^c_{i-1,j}, y^c_{i-1,j})$. Consider the left divided difference

$$\Delta q_L \equiv \frac{q_{i,j} - q_{i-1,j}}{\Delta l_i} . \tag{3.70}$$

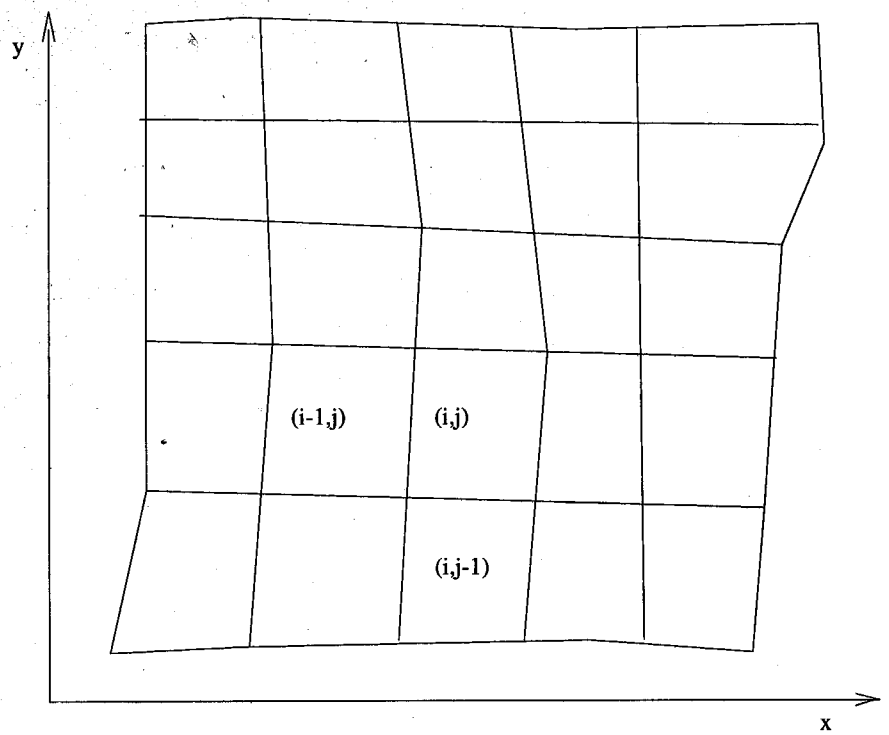

FIG.3.4 A typical computational mesh of quadrilaterals of arbitrary shape.

The differences $\Delta q_{\rm R}$, $\Delta q_{\rm U}$, $\Delta q_{\rm D}$, in the right, up, and down directions, respectively, are defined in a similar fashion. Then, the value of q at the left interface is given by

$$q_{i-1/2,j} \;=\; q_{i,j} - 0.5\,\Delta l_i\,\Delta q_{\rm LR}\;,$$

where $\Delta q_{\rm LR}$ is an approximation of the slope of q in the direction normal to the cell interface. It can be computed from $\Delta q_{\rm L}$ and $\Delta q_{\rm R}$ with the use of van Albada's limiter, van Leer (1984),

$$\Delta q_{\rm LR} \;=\; {\rm ave}(\Delta q_{\rm L}, \Delta q_{\rm R})\;, \tag{3.71}$$

and

$${\rm ave}(a,b) \;\equiv\; \frac{a+b}{2}\left(1 \;-\; \frac{(a-b)^2}{a^2+b^2+\epsilon^2}\right)\;, \tag{3.72}$$

with ϵ being a small positive number, say, $\epsilon = 10^{-12}$. This slope-limiting procedure is employed to preserve the monotonicity of q near discontinuities. The evaluation of q at the centers of the other cell interfaces is performed by repeating these steps to the appropriate interface.

For the numerical solution of the system of conservation equations, mass-averaged values of the conservative variables are considered:

$$m_{i,j} \equiv \int_{(i,j)} \rho \, \mathrm{d}x \, \mathrm{d}y \, , \tag{3.73a}$$

$$m_{i,j}u_{i,j} \equiv \int_{(i,j)} \rho u \, \mathrm{d}x \, \mathrm{d}y \, , \tag{3.73b}$$

$$m_{i,j}v_{i,j} \equiv \int_{(i,j)} \rho v \, \mathrm{d}x \, \mathrm{d}y \, , \tag{3.73c}$$

$$m_{i,j}e_{t\,i,j} \equiv \int_{(i,j)} \rho e_t \, \mathrm{d}x \, \mathrm{d}y \, , \tag{3.73d}$$

$$m_{i,j}z_{i,j} \equiv \int_{(i,j)} \rho z \, \mathrm{d}x\mathrm{d}y \, . \tag{3.73e}$$

Furthermore, let $g(T,z)$ denote the source term in the reaction equation:

$$g(T,z) = -K z e^{-E_a/T} \, , \tag{3.74}$$

and set

$$m_{i,j}g_{i,j} \equiv \int_{(i,j)} \rho g(T,z) \, \mathrm{d}x \, \mathrm{d}y \, . \tag{3.75}$$

The value of each of these integrals equals the product of the integrand, evaluated at the center of the cell, with the area of the cell, because linear variation of all primitive quantities has been assumed.

The flux vectors are given by

$$\mathbf{F}_m \equiv [\rho u, \, \rho v] \, , \tag{3.76a}$$

$$\mathbf{F}_u \equiv \left[\rho u^2 + p, \, \rho u\right] \, , \tag{3.76b}$$

$$\mathbf{F}_v \equiv \left[\rho uv, \, \rho v^2 + p\right] \, , \tag{3.76c}$$

$$\mathbf{F}_e \equiv [\rho e_t u + pu, \, \rho e_t v + pv] \, , \tag{3.76d}$$

$$\mathbf{F}_z \equiv [\rho zu, \, \rho zv] \, . \tag{3.76e}$$

The integration of the flux vectors along each cell interface is performed using the midpoint rule.

Consequently, the proposed numerical scheme, which evaluates the solution at time $(n+1)\Delta t$ from the solution at the previous time $n\Delta t$, can be written as:

$$\begin{aligned}(m_{i,j})^{n+1} = (m_{i,j})^n &- \Delta t \left[(l\mathbf{n}_s \cdot \mathbf{F}_m)^{n+1/2}_{i+1/2,j} - (l\mathbf{n}_s \cdot \mathbf{F}_m)^{n+1/2}_{i-1/2,j}\right] \\ &- \Delta t \left[(l\mathbf{n}_s \cdot \mathbf{F}_m)^{n+1/2}_{i,j+1/2} - (l\mathbf{n}_s \cdot \mathbf{F}_m)^{n+1/2}_{i,j-1/2}\right] ,\end{aligned} \tag{3.77a}$$

$$\begin{aligned}(m_{i,j}u_{i,j})^{n+1} = (m_{i,j}u_{i,j})^n &- \Delta t \left[(l\mathbf{n}_s \cdot \mathbf{F}_u)^{n+1/2}_{i+1/2,j} - (l\mathbf{n}_s \cdot \mathbf{F}_u)^{n+1/2}_{i-1/2,j}\right] \\ &- \Delta t \left[(l\mathbf{n}_s \cdot \mathbf{F}_u)^{n+1/2}_{i,j+1/2} - (l\mathbf{n}_s \cdot \mathbf{F}_u)^{n+1/2}_{i,j-1/2}\right] ,\end{aligned} \tag{3.77b}$$

$$\begin{aligned}(m_{i,j}v_{i,j})^{n+1} = (m_{i,j}v_{i,j})^n &- \Delta t \left[(l\mathbf{n}_s \cdot \mathbf{F}_v)^{n+1/2}_{i+1/2,j} - (l\mathbf{n}_s \cdot \mathbf{F}_v)^{n+1/2}_{i-1/2,j}\right] \\ &- \Delta t \left[(l\mathbf{n}_s \cdot \mathbf{F}_v)^{n+1/2}_{i,j+1/2} - (l\mathbf{n}_s \cdot \mathbf{F}_v)^{n+1/2}_{i,j-1/2}\right] ,\end{aligned} \tag{3.77c}$$

$$\begin{aligned}(m_{i,j}e_{i,j})^{n+1} = (m_{i,j}e_{i,j})^n &- \Delta t \left[(l\mathbf{n}_s \cdot \mathbf{F}_e)^{n+1/2}_{i+1/2,j} - (l\mathbf{n}_s \cdot \mathbf{F}_e)^{n+1/2}_{i-1/2,j}\right] \\ &- \Delta t \left[(l\mathbf{n}_s \cdot \mathbf{F}_e)^{n+1/2}_{i,j+1/2} - (l\mathbf{n}_s \cdot \mathbf{F}_e)^{n+1/2}_{i,j-1/2}\right] ,\end{aligned} \tag{3.77d}$$

$$\begin{aligned}(m_{i,j}z_{i,j})^{n+1} = (m_{i,j}z_{i,j})^n &- \Delta t \left[(l\mathbf{n}_s \cdot \mathbf{F}_z)^{n+1/2}_{i+1/2,j} - (l\mathbf{n}_s \cdot \mathbf{F}_z)^{n+1/2}_{i-1/2,j}\right] \\ &- \Delta t \left[(l\mathbf{n}_s \cdot \mathbf{F}_z)^{n+1/2}_{i,j+1/2} - (l\mathbf{n}_s \cdot \mathbf{F}_z)^{n+1/2}_{i,j-1/2}\right] . \\ &+ \Delta t \;\; \Delta S_{i,j} \;\; (m_{i,j}g_{i,j})^{n+1/2}\end{aligned} \tag{3.77e}$$

The flux terms in relation above have to be evaluated at the center of each cell interface, and at time $t = (n+1/2)\Delta t$. This is performed by making use of the information provided by the invariant manifolds that were studied in the previous section. This procedure is illustrated below, for the interface between the cells (i,j) and $(i+1,j)$. For the other three cell interfaces, the procedure is exactly the same.

Let $\mathbf{x}_w = (x_w, y_w)$ denote the center of this interface. One has to trace specific curves along the five invariant manifolds that pass through the point with coordinates $(x_w, y_w, (n+1/2)\Delta t)$, and find the intersection of these curves with the surface $t = n\Delta t$. Then, the equations that hold on the manifolds have to be discretized and solved numerically.

But first, one should select $\mathbf{n}$. Recall that there is a one-parameter family of the manifolds $\mathcal{S}_+$ that is generated by the rotation of $\mathbf{n}$. These manifolds form a conoid equivalent to the ray conoid. By selecting $\mathbf{n}$, one essentially decides the direction along which the ODE's that hold on $\mathcal{S}_+$, and $\mathcal{S}_-$, are solved. Numerical experiments showed that selecting the unit normal to the cell interface, *i.e.*, $\mathbf{n} = \mathbf{n}_s$, works well in practice.

Having determined the manifold $\mathcal{S}_+$ that will be used, one has to decide which specific curve on $\mathcal{S}_+$ should be traced forward in time, *i.e.*, which convective velocity $\mathbf{u}_+$ will be used. The intersection of $\mathcal{S}_+$ with the plane $t = n\Delta t$ is the locus of the points that are connected with the point $(x_w, y_w, (n+1/2)\Delta t)$ by the characteristic differential equation (3.29d); see Fig. 3.5. Each point of this curve corresponds to a specific $\mathbf{u}_+$. In the present work, the convective velocity $\mathbf{u}_+$ has been selected to satisfy equation (3.43). In other words, the curve that lies as close to the equivalent characteristic as possible has been chosen.

The coordinates of the point at which this curve intersects the plane $t = n\Delta t$, say $\mathbf{x}_p$, are evaluated by solving equation (3.30d) numerically. For this purpose the selected curve is approximated by a straight line. After some straightforward calculations, one gets the following expression for the coordinates of $\mathbf{x}_p$:

$$\begin{bmatrix} x_p \\ y_p \end{bmatrix} = \frac{1}{\det \boldsymbol{\Xi}} \boldsymbol{\Xi} \cdot \boldsymbol{\Sigma}\,, \tag{3.78}$$

where

$$\boldsymbol{\Xi} = \begin{bmatrix} (v+v_+)_y + \frac{2}{\Delta t} & -(u+u_+)_y \\ -(v+v_+)_x & (u+u_+)_x + \frac{2}{\Delta t} \end{bmatrix},$$

$$\boldsymbol{\Sigma} = \begin{bmatrix} \frac{\Delta x}{\Delta t} - (u+u_+) \\ \frac{\Delta y}{\Delta t} - (v+v_+) \end{bmatrix},$$

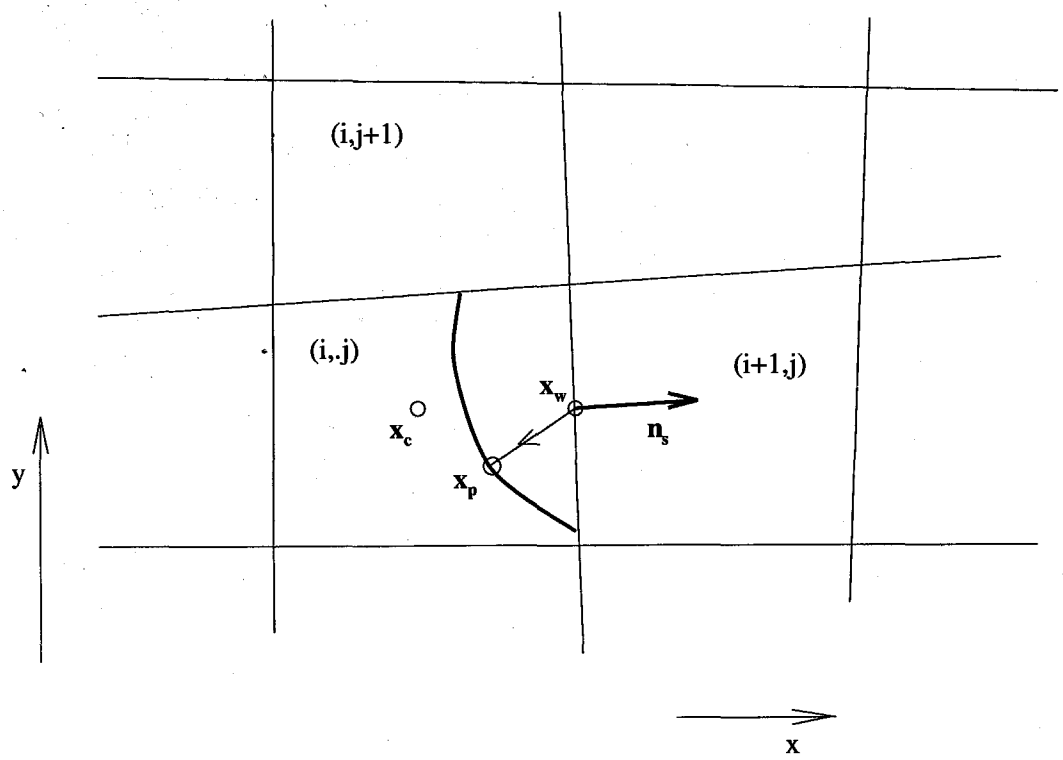

FIG.3.5 The locus of the points at $t = n\Delta t$, that are connected with (x_w, y_w) through (3.29d).

All the quantities in this relation are evaluated at the center of the cell interface. Once the coordinates of $\mathbf{x}_p$ are computed, the solution vector is evaluated at this point.

This procedure is repeated for the manifold $\mathcal{S}_-$ by setting $\mathbf{n} = -\mathbf{n}_s$. The specific curve on $\mathcal{S}_-$ that is used is the one that corresponds to a convective velocity $\mathbf{u}_-$ which satisfies (3.51). The point at the plane $t = n\Delta t$ that is connected with $(x_w, y_w, (n+1/2)\Delta t)$ by the characteristic equation (3.29e) is determined by solving numerically the equation (3.30e), with a procedure similar to the one employed for (3.30d) that was described earlier. Then, the solution vector is evaluated at this point.

Subsequently, the ODE's (3.29d) and (3.29e) are solved for the computation of the pressure and the normal velocity component at the cell interface at time $(n + 1/2)\Delta t$. These two equations must be supplemented with the appropriate

jump conditions, in the presence of discontinuities. The easiest and most robust way to implement this, is to consider a one-dimensional Riemann problem in the direction parallel to $\mathbf{n}$. As mentioned in the second chapter, the Riemann problem that corresponds to the governing equations for reacting flows is not the same as the classical one-dimensional gasdynamic Riemann problem. This Riemann problem is not self-similar and, as a result, shock waves and expansion fans are not straight lines anymore, *i.e.*, they are accelerating. Yet, one can safely use the classical one-dimensional Riemann problem, because, as mentioned in Chapter 2, the difference between the two solutions vanishes as $t \to 0$, $x \to 0$.

It should also be mentioned that, by design, shock-capturing schemes allow discontinuities only at the cell interfaces and parallel to them. This constraint can be important, especially in cases of shock fronts with high curvature. The result is that in the presence of oblique shocks, there is more numerical diffusion than one would expect. This problem is a constraint imposed by the grid and it is independent of the effort to construct multi-dimensional, unsplit schemes.

The tangential velocity component, $\mathbf{u}\cdot\mathbf{n}^{\perp}$, is evaluated by selecting a curve on $\mathcal{S}_{\perp}$. In the present work the selected curve corresponds to the velocity $\mathbf{u}_{\perp}$ given by equation (3.58c). As usual, the curve is approximated by a straight-line segment, and its intersection with the plane $t = n\Delta t$ is computed. At that point, $\mathbf{u}\cdot\mathbf{n}^{\perp}$ has the same value as at $(x_w, y_w, (n+1/2)\Delta t)$. The expression for the coordinates of that point is analogous to (3.77). The reactant mass fraction is evaluated by selecting a curve on $\mathcal{S}_{\mathrm{r}}$. The selected curve corresponds to a velocity $\mathbf{u}_{\mathrm{r}}$ given by equation (3.58b).

Finally, the density is evaluated by tracing the curve on $\mathcal{S}_0$ that corresponds to a velocity $\mathbf{u}_0$ given by equation (3.58a), and subsequently locating the point at which this curve crosses the $t = n\Delta t$ plane. Let p_0, ρ_0 denote the values of pressure and density at this point. The density at the interface, say $(i+1/2, j)$, is evaluated by discretizing equation (3.29a) in the following way:

if $p^{n+1/2}_{i+1/2,j} > p_0$, then

$$(p^{n+1/2}_{i+1/2,j} - p_0) - \frac{\gamma p_0}{\rho_0}\left(\frac{\gamma+1}{2\gamma} + \frac{\gamma-1}{2\gamma}\frac{p^{n+1/2}_{i+1/2,j}}{p_0}\right)(\rho^{n+1/2}_{i+1/2,j} - \rho_0) \;=\; 0\,. \qquad (3.78a)$$

If $p^{n+1/2}_{i+1/2,j} < p_0$, then

$$\rho^{n+1/2}_{i+1/2,j} = \rho_0 \left(\frac{p^{n+1/2}_{i+1/2,j}}{p_0} \right)^{1/\gamma} . \tag{3.78b}$$

Equation (3.78a) is the jump condition of (3.29a). It is used when the curve on $\mathcal{S}_0$ is being crossed by a shock. Equation (3.78b) is just the discretized version of (3.29a). An example of the projection of five curves that were traced to upwind the solution, on the (x,t)-plane, is shown in Fig. 3.6.

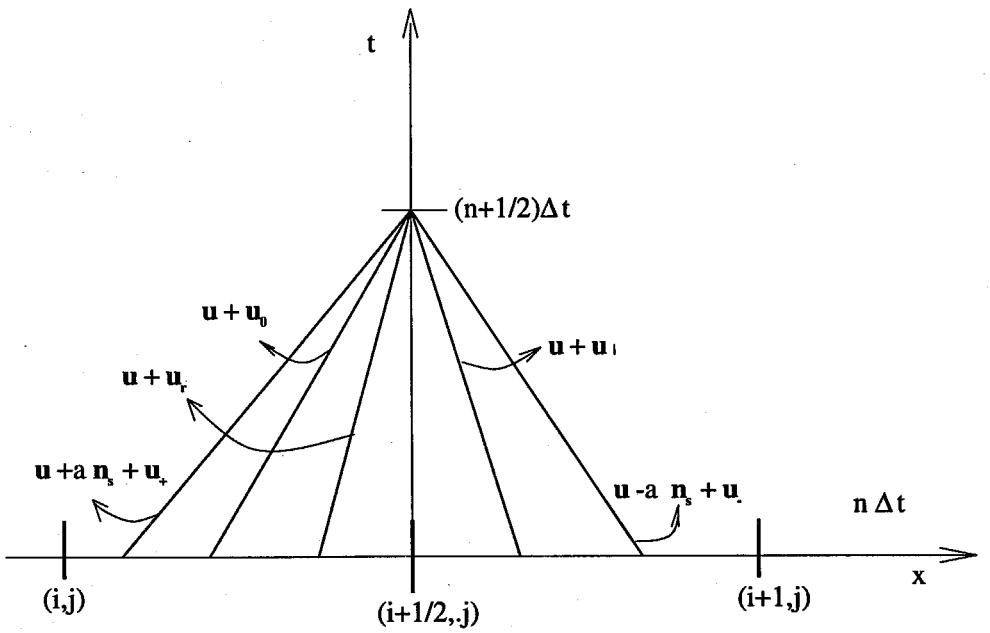

FIG.3.6 A typical example of the projection of the five curves used to find the solution at $t = (n + 1/2)\Delta t$ on the (x,t)-plane.

CHAPTER 4

Numerical Study of Two-Dimensional Detonations

4.1 Historical Background

Detonations are generally unstable phenomena that can develop very complicated structures. The most noticeable structure of a detonation is the cellular pattern. Examples of such patterns can be found in the photographs of Strehlow *et al.* (1972), and Fickett & Davis (1979), which were taken during experiments with detonations in channel flows. These patterns are self-sustained because of the continuous energy release from the chemical reaction. The cells are diamond-shaped and are formed by transverse waves. The cell-size can be almost uniform, resulting to a system of regularly-distributed cells, or it might vary from cell to cell. The existence, or not, of such regularity depends on the combustible mixture and the width of the channel. In general, narrow channels result in cells of uniform size. Unconfined detonations typically produce irregular cellular patterns. Fickett & Davis (1979) observe that the cell-spacing is of the order of 100 reaction-lengths of the steady (ZND) solution.

The transverse waves that are responsible for the formation of the cellular patterns move along the leading front. They are generated by the non-uniformities of the front and are attached to it at triple-points via the traditional three-shock pattern. The Mach stem and the incident shock are part of the leading front and the transverse wave is the reflected shock. The strength of a transverse wave is not constant, it diminishes with time. Consequently, the propagation velocity of these waves is not constant either. Transverse waves moving in opposite directions collide with each other. These collisions lead to explosions that release large amounts of heat and enable the rejuvenation of the three-shock structures.

One finds that the non-uniformities of the leading shock are small hot spots, distributed along the front. Eventually they explode, resulting in the development of micro-detonations. The waves generated by these explosions interact with each other and form a triple point that signals the generation of the transverse waves. Two important issues have attracted the attention of researchers on the field of detonation dynamics. The first issue is the stability of two-dimensional detonations. The second issue is the size of the cellular structure of an unstable detonation.

The linearized, two-dimensional stability problem has been considered by Erpenbeck (1964), who used a Fourier-series approach to investigate the growth-rate of transverse instabilities. Strehlow and his coworkers pioneered the investigation of the role of acoustic-ray trapping in the reaction zone (see, Strehlow & Fernandez (1965), Barthel & Strehlow (1966), Barthel (1974), *etc.*. They employed the method of geometrical acoustics to derive simplified stability criteria. These criteria examine whether amplification of the acoustic signal occurs, or not. Strehlow (1970), and Barthel (1972), presented cell-size predictions based on these simplified stability approaches. Recently, Majda (1987) used non-linear geometrical optics for the prediction of the cell-size.

In general, linearized-stability theories applied to these problems are very accurate in the prediction of the stability limits. As it turns out, two-dimensional detonations, governed by one-step Arrhenius kinetics, are intrinsically unstable. It is worth mentioning that unstable behavior is encountered even in cases where the corresponding one-dimensional problem is stable. Stability is maintained only if the overdrive is extremely high (more than 10), or the activation energy is very small. The approximate theories mentioned above, however, have not been successful in the prediction of cell-size. The mechanisms that determine the evolution of detonations are highly non-linear and, as a result, theoretical results based upon linearity assumptions are of limited validity.

Traditionally, studies of the geometry of the detonation front were based in observations, interpreted with information provided by standard blast-wave and shock-dynamics theories, like the one proposed by Whitham (1974). These theories take advantage of the fact that, in the non-reacting case, the flow in the neighborhood of a triple point is almost steady. Applications of these theories to reacting flows have enjoyed limited success, because of the complexity and the unstable nature of the flow around a triple point of the detonation front. For recent modelling

efforts see, among others, Stewart & Bdzil (1988), Bdzil & Stewart (1989), Bartlma (1990), Bukiet & Menikoff (1992), Klein & Stewart (1993), and Menikoff *et al.* (1996). In all these works, the simplified one-step model was used, and the assumption of absence of transport mechanisms was made. Therefore, viscosity effects, such as boundary layers, and multiple-species effects, such as chain-branching, were ignored.

Numerical simulations of two-dimensional detonations using finite-difference schemes were initiated in the late '60s and early '70s. See, for example, the pioneering work of Taki & Fujiwara (1973). The simulations served as a supplement to the experimental investigations and to the theoretical-modelling approaches. The quality of the simulations has been improved greatly over the years because of the progress that was achieved in the numerical analysis of hyperbolic equations.

In the early '90s, a trend of detailed, high-fidelity, reacting-flow simulations was established. Modern, state-of-the-art schemes that were developed during the '80s, were employed in these simulations. Oran *et al.* (1982) and Lefebvre *et al.* (1993), simulated detonating channel flows (with periodic boundary conditions at the top and bottom boundaries) using the Flux-Corrected-Transport (FCT) algorithm. Bourlioux & Majda (1991) performed simulations of the same problem for a wide range of parameters using the Piecewise Parabolic Method (PPM) with adaptive mesh refinement and front-tracking of the main front. Quirk (1993) also employed a Roe's solver and adaptive mesh refinement for this problem.

Cai (1995) designed a hybrid algorithm that uses an Essentially Non-Oscillatory (ENO) scheme at regimes of steep gradients and spectral representation at regimes where the flow is smooth. He also studied channel-flow problems using reflecting-wall boundary conditions at the top and bottom boundaries. Schoffel & Ebert (1988) had worked in the same problem earlier, and investigated the number of cells that were formed, as a function of the channel-width. They compared their results with the experimental work of Strehlow *et al.* (1972), and they reported satisfactory agreement. The algorithm that they used was based on McCormack's method.

Another problem that has been the subject of numerical studies is the simulation of oblique detonation waves. Such detonations can be generated, for example, in supersonic flow of a combustible mixture over a long wedge. In this problem, the

oblique shock that is formed at the tip of the wedge turns upward due to dilatation of the gas caused by the reaction that takes place behind the shock. There is an important question associated with this flow, and it has to do with the stability of the oblique wave. If the detonation is stable, one should expect that the asymptotic structure of the shock is an oblique ZND wave. Nonetheless, this structure might not be realizable for a variety of wedge-angles and detonation parameters. For a detailed discussion of the possible configurations see, among others, Buckmaster (1990) and Shepherd (1994). An asymptotic treatment of this problem in the hypersonic limit has been presented by Powers & Stewart (1992). A definitive answer has yet to be given to the problem determining the stability boundaries of such flows.

Cambier *et al.* (1989) and Glenn & Pratt (1988) carried numerical simulations for the problem mentioned above, but their grid was too coarse (of the order of 100×100 cells). As a result, the reaction region was not well-resolved in their simulations. Li *et al.* (1994), performed simulations for the same problem using the FCT algorithm on a 450×150 grid. More recently, Grismer (1995) worked on a similar problem with a Roe's solver. In his simulations the wedge was curved in such a way that the resulting detonation front should theoretically be straight. His grid, however, was of the order 200×200, and his results seemed to be underresolved.

It is worth mentioning that the study of detonations induced by a wedge has attracted a lot of attention because of the concept of the oblique detonation wave engine. The idea is to use the thrust from the wave for propulsion purposes. The problem of premixing the fuel in a safe way has hampered, so far, the construction of such an engine.

In the present work, two different problems are studied numerically. The first one is the two-dimensional detonation in a narrow channel. Simulations of this problem will help demonstrate the effectiveness of the proposed scheme and to make comparisons with previous results. They will also help to gain new insight on the various mechanisms that govern the propagation of two-dimensional detonations, and in particular the effect of the vorticity generated at the detonation front. The second problem is the flow generated by an impulsively started wedge. This problem is studied numerically because of the important practical applications associated with it, such as the design of scramjet engines. High-resolution simulations of this problem using state-of-the-art algorithms have not been published yet. But first,

two tests on non-reacting flows are presented. These simulations are performed for diagnostic purposes. They demonstrate the suitability of the developed algorithm for the study of compressible, inert flows. The simulations presented in this chapter were performed on either a VAX-alpha machine or an SGI-onyx system.

4.2 Preliminary Tests with Non-Reacting Flows

The first test is the problem of double Mach reflection. This is a classical test, used by many authors to validate a numerical scheme and to make comparisons with other schemes; see, for example Woodward & Colella (1984). A strong planar shock diffracts from a 30° wedge. The velocity behind the shock is so high that the shocked fluid particles do not have enough time to turn. The turn is thus achieved via the triple-point mechanism. The shock that emanates from the triple point perpendicular to the wedge is the Mach stem. The flow behind the Mach stem is subsonic in the shock-attached frame. The shock that connects the triple point and the tip of the wedge is the reflected shock. The triple-point structure essentially plays the role of an additional ramp on which regular reflection can occur. The shock Mach number for the numerical test is $M_s = 10.0$. The medium ahead of the shock is quiescent and has the following thermodynamic properties:

$$p = 1.0 \ , \qquad \rho = 1.4 \ , \qquad \gamma = 1.4.$$

All quantities have been made dimensionless with respect to these values. The computational domain is shown in Fig. 4.1a. It consists of 180 × 90 cells. The length of the domain is $x = 3.0$. The height of the domain at the tip of the ramp is $y = 2.0$. The shock is initially located at $x = 0.10$. The CFL number for this simulation is set to 0.8.

Results for the density at $t = 0.20$ are shown in Fig. 4.1b. In this figure there are 25 contours in the range $1.4 \leq \rho \leq 19.81$. It can be verified from this figure that all the features of the flow, such as the transverse shock wave and the slip line, are well resolved. The results for the structure of the flow as obtained by the proposed scheme are in good agreement with the results that can be found in Woodward & Colella (1984).

The second test is the diffraction of a shock from a corner. A planar shock is propagating in a channel with a recess at a given point. As soon as the shock reaches the corner, an expansion fan and a shear layer are formed. The shock gets curved and vorticity is generated. The shock Mach number for this problem is taken to be $M_s = 5.0$. As in the first test, the medium ahead of the shock is quiescent and has the following thermodynamic properties:

$$p = 1.0 , \qquad \rho = 1.0 , \qquad \gamma = 1.4.$$

The computational domain has the shape of a rectangle and consists of 120×160 cells. Reflecting-wall conditions are imposed at the top and bottom boundaries. Outflow conditions are imposed at the right boundary. The corner is assumed to be located at the center of the left boundary. At this boundary inflow conditions are given at the upper half (at the upper 80 cells), and reflecting-wall conditions are assigned at the lower part. Initially, the shock is located at the upper half of the left boundary, and is about to diffract. The CFL number for this simulation is 0.8.

Results for the pressure and density at $t = 0.08$ are plotted in Figs. 4.2a and 4.2b, respectively. In these figures, there are 30 pressure contours in the range $0.13 \leq p \leq 29.6$, and 30 density contours in the range $0.06 \leq \rho \leq 5.0$. It can be verified that all the important features of the flow, as identified experimentally by Bazenhova *et al.* (1984), are captured.

These two tests help to demonstrate that the proposed algorithm is suitable for accurate numerical simulations of compressible flows with strong shocks. The smearing of all discontinuities has been kept in satisfactory levels: a discontinuity, either parallel or oblique to the cell-boundaries, never occupies more than three cells. After these preliminary results, a detailed study of two-dimensional detonations is presented.

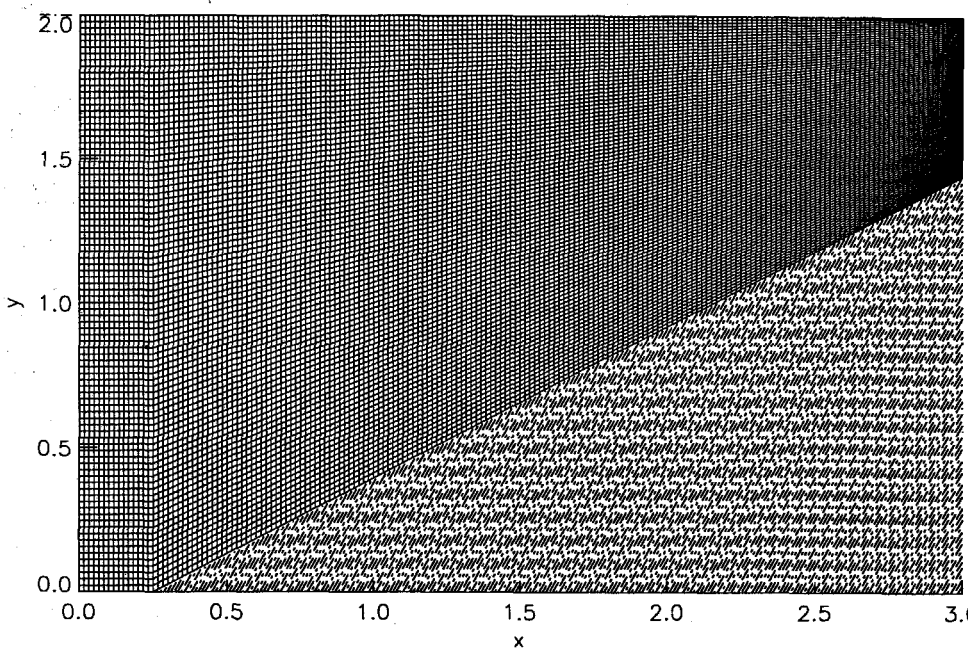

FIG.4.1a The computational domain for the double Mach reflection problem, consisting of 180×90 cells.

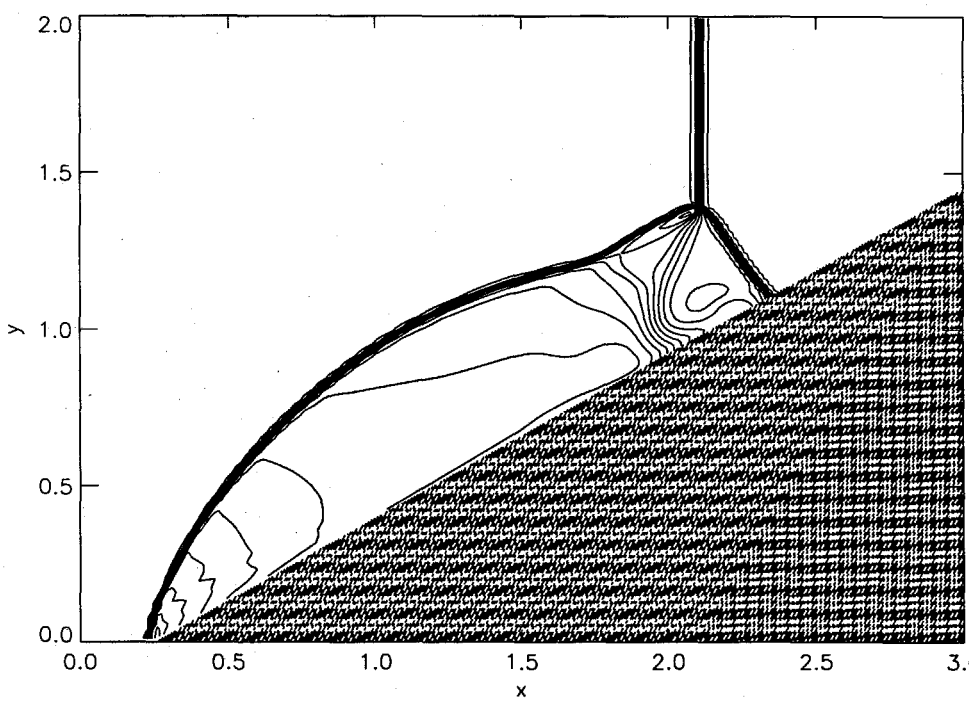

FIG.4.1b Density contours at $t = 0.20$ for the double Mach reflection problem. There are 25 contours in the range $1.4 \leq \rho \leq 19.81$.

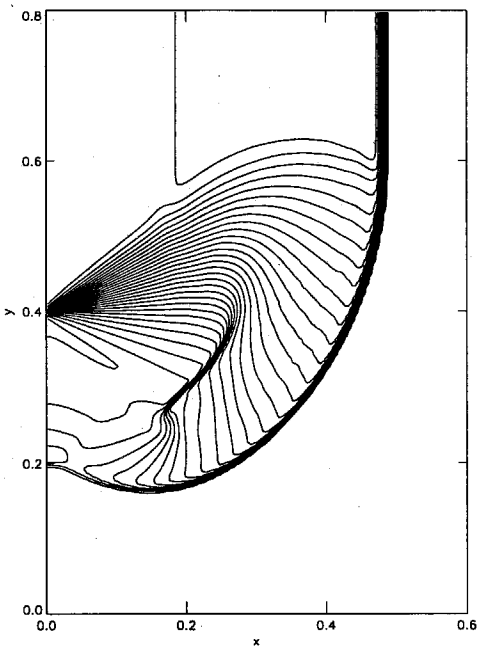

FIG.4.2a Pressure contours at $t = 0.08$ for the problem of a shock diffracting from a corner. There are 30 contours in the range $0.13 \leq p \leq 29.6$.

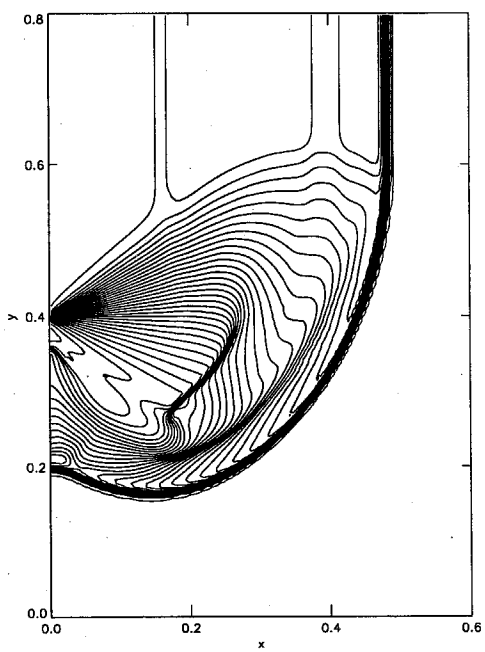

FIG.4.2b Density contours at $t = 0.08$ for the problem of a shock diffracting from a corner. There are 30 contours in the range $0.06 \leq \rho \leq 5.0$.

4.3 Numerical Study of Detonations in Channel Flows

A set of numerical experiments is performed for the study of the instabilities that are developed in two-dimensional detonations. The computational domain is a rectangle. Periodic conditions are imposed at the top and bottom boundaries and inflow conditions are imposed at the left boundary. Finally, outflow conditions are prescribed at the right boundary. The flow at this boundary is subsonic. The problem of evaluating the fluxes across the boundary becomes underdetermined when one or more curves of the invariant manifolds lie outside the computational domain. Therefore, an a priori condition needs to be imposed, but in such way that no artificial wave-reflections occur at the boundary.

In the present work this is achieved by copying the values from the boundary cells to their corresponding dummy cells. By doing so, two conditions are satisfied. First, all the invariant curves lie inside the computational domain except

$$(t, \mathbf{x}) \in t \times \Re^N : \frac{\mathrm{d}\mathbf{x}}{\mathrm{d}t} = \mathbf{u} - a\,\mathbf{n} + \mathbf{u}_- ,$$

which lies outside. Second, each term of the characteristic equation that holds on the above curve, namely

$$\frac{\mathrm{D}p}{\mathrm{D}t} - \rho\, a \frac{\mathrm{D}}{\mathrm{D}t}(\mathbf{u} \cdot \mathbf{n}) = 0 ,$$

becomes identically zero, thus overcoming the underdeterminacy problem.

The initial condition is a transversally perturbed, planar ZND wave, propagating in a quiescent medium. For a given choice of parameters the one-dimensional ZND profile has been computed numerically (the procedure has been explained in Chapter 2) and it is assigned to each longitudinal station throughout the width of the domain. The perturbation is a sinusoidal variation of the amplitude of the post-shock values of the flow variables in the transversal direction, and it is employed to trigger the instabilities faster than the truncation error would.

It should be mentioned that the ZND wave is assumed to propagate to the left (hence the use of inflow condition at the left boundary), and it is considered to be stationary with respect to the laboratory frame. This means that if the flow was indeed steady, as postulated by the ZND theory, the position of the shock front would be constant.

It is a common practice to employ explicit artificial dissipation mechanisms for compressible flow simulations. The use of these mechanisms is necessary because the implicit viscosity of a scheme, which arises from the discretization of the equations and the monotonicity constraints, is not adequate for the stabilization of strong shocks, especially in cases where the shocks are moving slowly with respect to the grid. For a detailed discussion on this topic; see Colella & Woodward (1984).

No explicit dissipation mechanism, however, needs to be employed in the proposed unsplit scheme, even though the leading shock fronts in detonations are typically very strong *, and they are moving slowly with respect to the grid. It is worth noticing that, to the author's best knowledge, explicit artificial viscosity terms have been used in all previously published results of two-dimensional detonations. These terms deemed necessary in the vicinity of either the leading shock, or the transverse shock waves. For example, Bourlioux & Majda (1991) had applied front-tracking for the leading shock, but artificial viscosity was used to stabilize the transverse waves.

In the present study five different cases have been considered. These cases correspond to different selections for the overdrive and the activation-energy parameter, and are presented below. In all cases the variables and the parameters of the system have been made dimensionless by reference to the uniform state ahead of the detonation front. The values of the specific heat ratio, γ, and the heat release coefficient, q_0, have been set at:

$$\gamma = 1.2 \,, \qquad q_0 = 50.0 \,.$$

As usual, the half-reaction length of the steady ZND profile, $L_{1/2}$, has been selected to be the characteristic length-scale. The characteristic length-scale divided by the sound speed ahead of the shock provides the characteristic time-scale. The spatial

* The shock Mach number of the fronts in the cases considered in the present study is of the order of 10.

resolution is 20 points per $L_{1/2}$, and the CFL number has been set at $CFL = 0.7$. The sinusoidal transversal perturbation has amplitude equal to 0.2% of the value of the respective variable. The wavelength of the perturbation is one unit-length, for all cases considered.

4.3.1 Case A

This is a case of high activation energy and strong overdrive. The values of these parameters are set as follows:

$$E_a = 50.0 , \qquad f = 3.0 .$$

Given these values, the stiffness coefficient of the system is $K = 30.06$. The computational domain for this simulation is 30 unit-lengths long and 10 unit-lengths wide. The ZND wave is initially located at $x = 25.0$.

The corresponding one-dimensional case is linearly stable, *i.e.*, there are no linearly unstable longitudinal modes. The transversal perturbations, however, grow and interact with the truncation error, and transverse waves are eventually generated. These waves lead to the formation of the familiar cellular patterns. As mentioned earlier, the explosions generated by the collisions of the transverse waves release large amounts of heat that allow the conservation of these patterns.

Contour plots for this case are presented in Fig. 4.3. In these plots, 30 contour levels of the pressure, temperature, and vorticity are plotted, equally distributed between the extremal values. Furthermore, 11 contours of the reactant mass fraction are plotted, with contour levels at $z = 0.01, 0.1, 0.2, \ldots,$ 0.9, 0.99. There are several contour plots taken at different times. The time difference between two consecutive plots is one time unit. Additionally, schlieren-type snapshots of the above variables are presented in Fig. 4.4. The expression "schlieren-type snapshot" implies snapshots of the norm of the gradient vector of a variable.

It can been observed in these figures that three shock waves and a contact surface emanate from each triple point. The shock waves are the Mach stem and the incident shock, which are part of the leading front, and the transverse wave. The contact surface emanating from the triple point is a rolled-up vortex sheet.

The vorticity plots reveal that when two triple points collide, the vortex sheets detach from the structure of the leading front and travel downstream. Vorticity is also generated by the curvature of the shock. A large part of this vorticity is annihilated by the dilatation of the fluid within the reaction zone. The vorticity plots also suggest that the vortices behind the reaction front interact with each other: small vortices are absorbed by large ones. The diffusion of these vortices is determined completely by the implicit artificial viscosity of the scheme, because there are no viscosity terms in the system of equations under consideration. By comparing results taken at different times, one can verify that collisions of triple points give birth to new triple points that move along the leading shock front until they collide, too.

It is also interesting to mention that there is an induction region behind the shock. The material in this region reacts very slowly, as it can be observed in the plots of the temperature and the reaction variable. The length of this region varies in the transversal direction, but it is usually of the order of one unit-length. Beyond the induction region the material reacts almost completely and the temperature rises substantially. The zone where most of the reaction takes place typically occupies a few tenths of a unit-length in the longitudinal direction.

The dimensionless shock pressure, according to the ZND solution, is $p_s = 126.36$. During the numerical simulation the shock pressure goes as high as $p_s = 384.79$, almost three times higher than the ZND value. This maximum value is reached when explosions occur. The results obtained in the present study are in good qualitative agreement with the results presented by Bourlioux & Majda (1991).

4.3.2 Case B

In this case, the activation energy is kept the same and the overdrive factor is lowered:

$$E_a = 50.0 , \qquad f = 2.0 .$$

The stiffness coefficient for this detonation is $K = 99.76$. The computational domain for this simulation is the same as in Case A, *i.e.*, 30 unit-lengths long and 10 unit-lengths wide. The initial ZND wave is located at $x = 25.0$.

The corresponding one-dimensional flow is linearly stable. Consequently, longitudinal instabilities do not grow and they are expected to decay with time. The main features that can be observed in the flow-field of the previous case are also present in this detonation, *i.e.*, triple points collide, releasing large amounts of energy. The rolled-up vortex sheets that emanate from the triple points move downstream after these explosions, and interact with each other.

But there are also some new features in the flow-field. The transverse waves are stronger and their length is considerably larger than in Case A. Furthermore, the reaction zone can be much longer, up to six unit-lengths long. This occurs at the parts of the flow that are characterized by large amounts of vorticity. It is observed that strong vorticity impedes the reaction process. The shock pressure, as predicted by the ZND theory, is $p_s = 84.79$, but the simulation showed that it can go as high as $p_s = 179.87$ during an explosion.

Contour plots for this case are presented in Fig. 4.5. There are 30 contours of the flow variables in each plot, equally distributed between the extremal values. Furthermore, the plots of the reactant mass fraction consist of 11 contours at levels mentioned earlier. Schlieren-type snapshots of the flow variables are presented in Fig. 4.6. For this detonation, contour plots of the temperature field, taken at nearby times, are given in Fig. 4.7. Each plot contains 20 contours, equally distributed between the extremal values. These plots serve to visualize the process of the triple-point collisions and the explosions that take place in the front.

4.3.3 Case C

In this case the overdrive factor is lowered even more:

$$E_a = 50.0 , \qquad f = 1.6 .$$

The stiffness coefficient for this detonation is $K = 230.75$. The computational domain for this simulation is, as usual, 30 unit-lengths long and 10 unit-lengths wide. The initial ZND wave is located at $x = 25.0$. Contour plots and schlieren-type snapshots of the flow variables for this problem are presented in Figs. 4.8 and 4.9, respectively. The format of these figures is the same as in the previous cases.

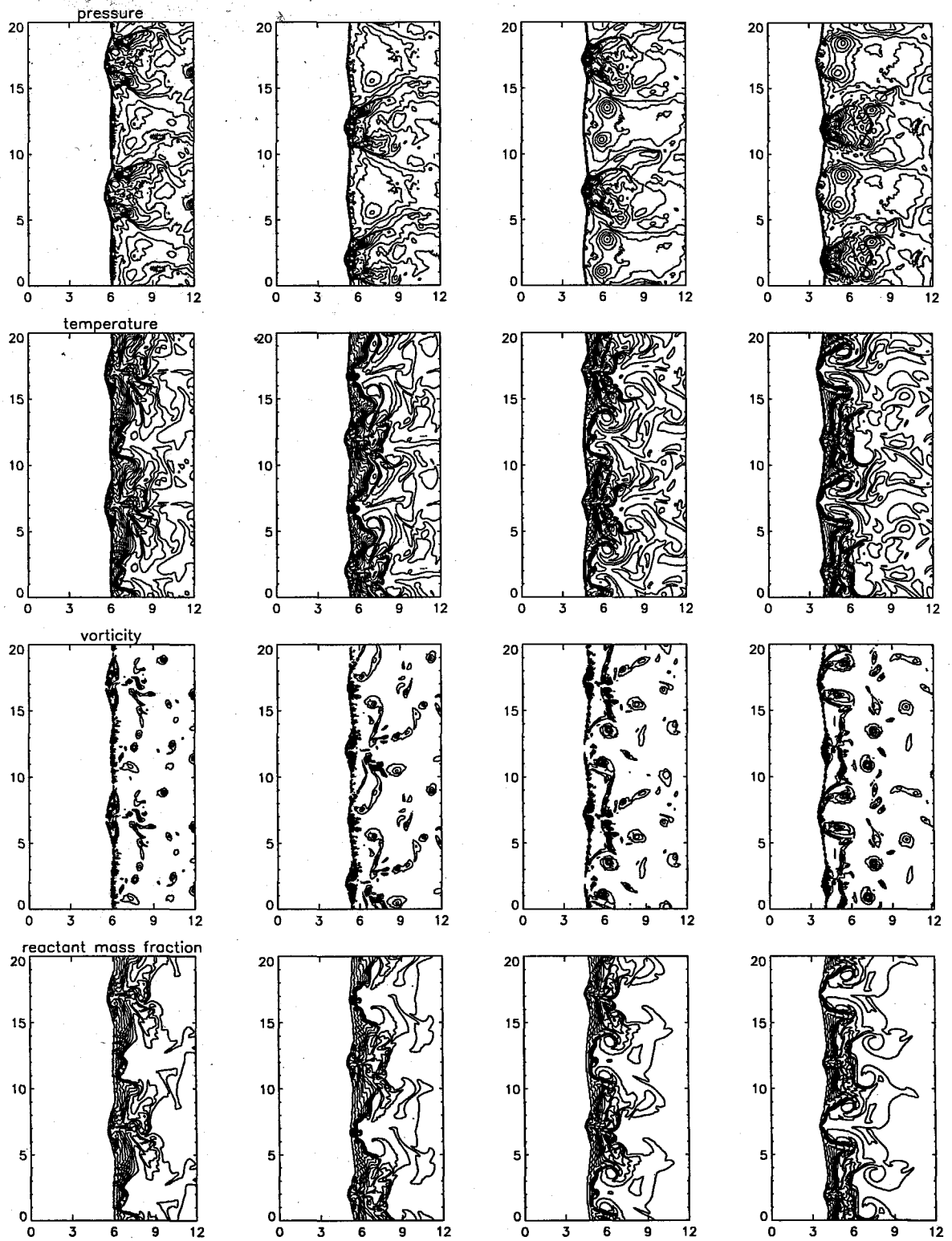

FIG.4.3a Case A: contour plots of the flow variables of the detonation. Results taken at times, from left to right, $t = 42.0, 43.0, 44.0, 45.0$. Two periods in the y-direction are plotted.

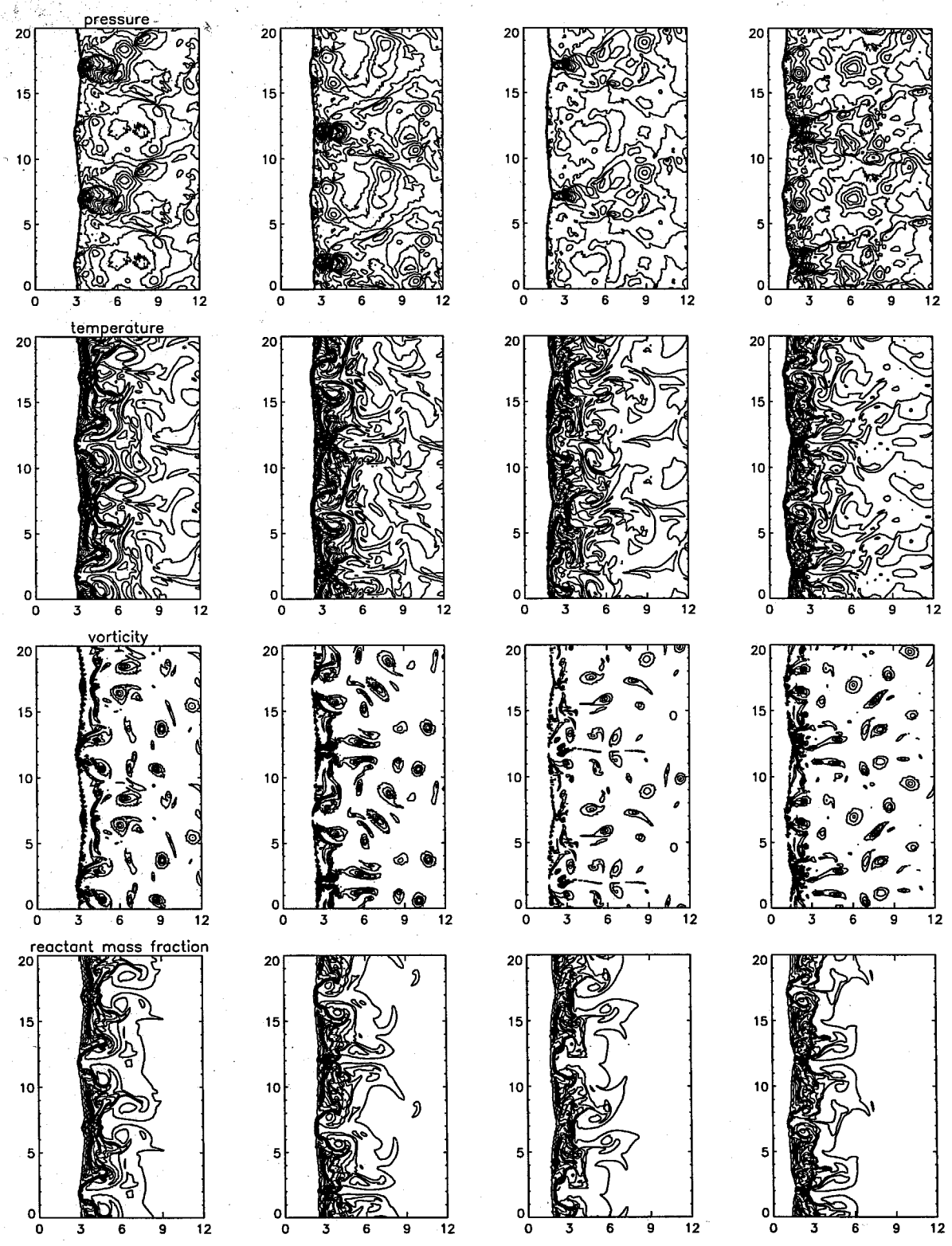

FIG.4.3b Case A: contour plots of the flow variables of the detonation. Results taken at times, from left to right, $t = 46.0, 47.0, 48.0, 49.0$. Two periods in the y-direction are plotted.

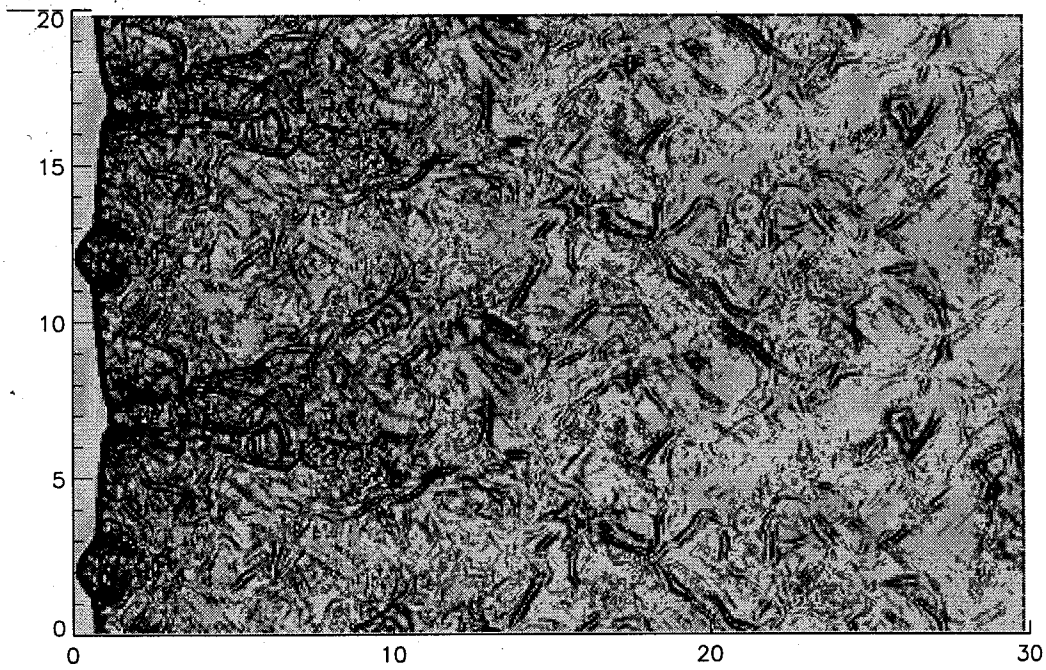

FIG.4.4a Case A: schlieren-type image of the pressure field of the detonation. Results taken at $t = 50.0$. Two periods in the y-direction are plotted.

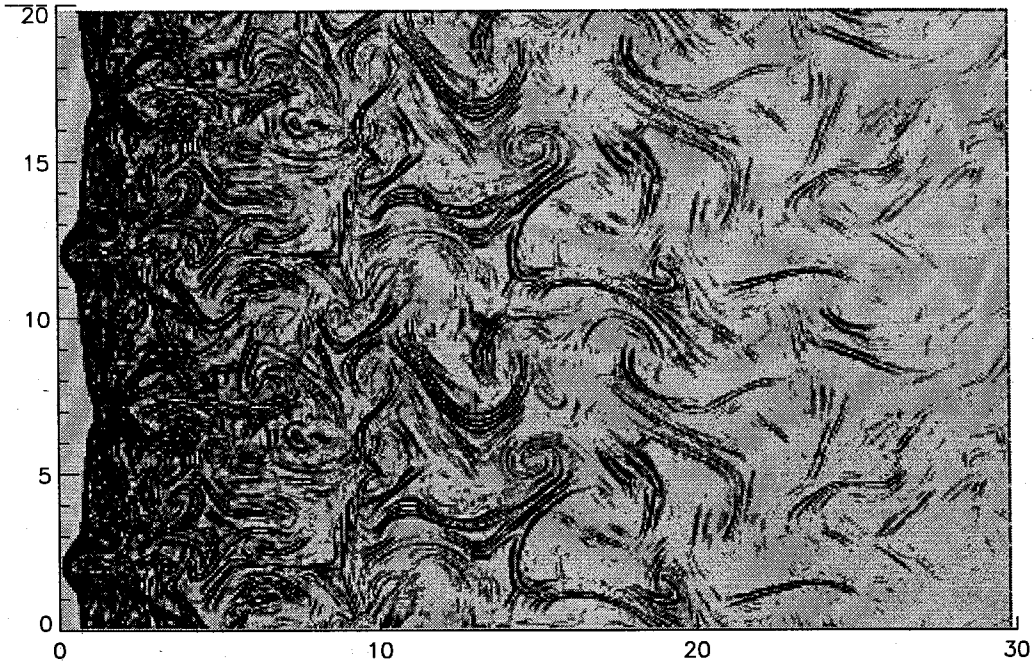

FIG.4.4b Case A: schlieren-type image of the temperature field of the detonation. Results taken at $t = 50.0$. Two periods in the y-direction are plotted.

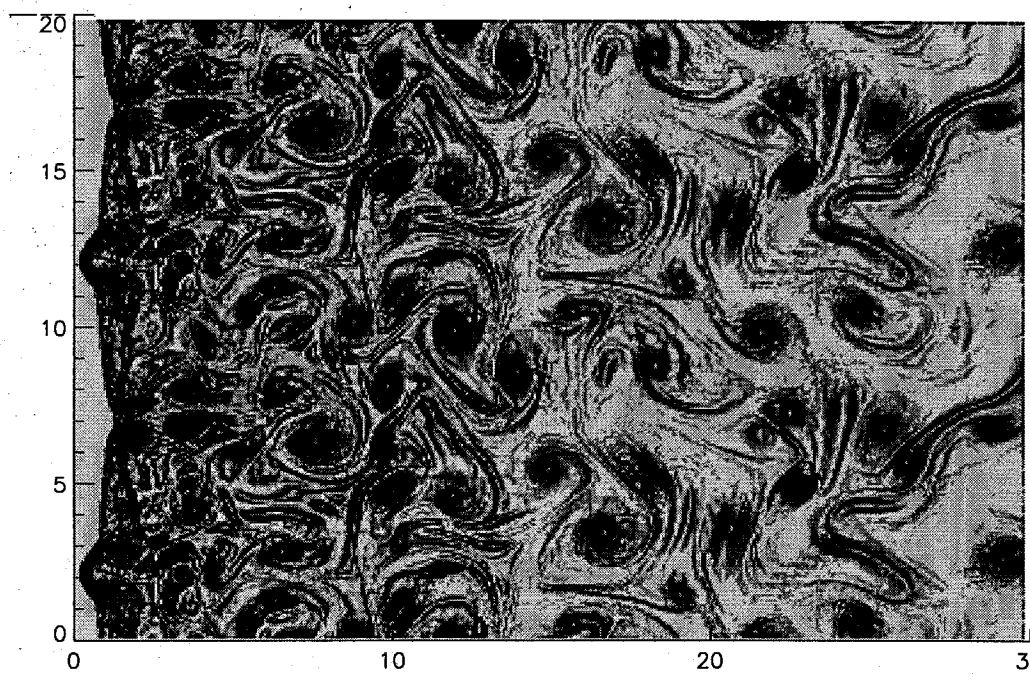

FIG.4.4c Case A: schlieren-type image of the vorticity field of the detonation. Results taken at $t = 50.0$. Two periods in the y-direction are plotted.

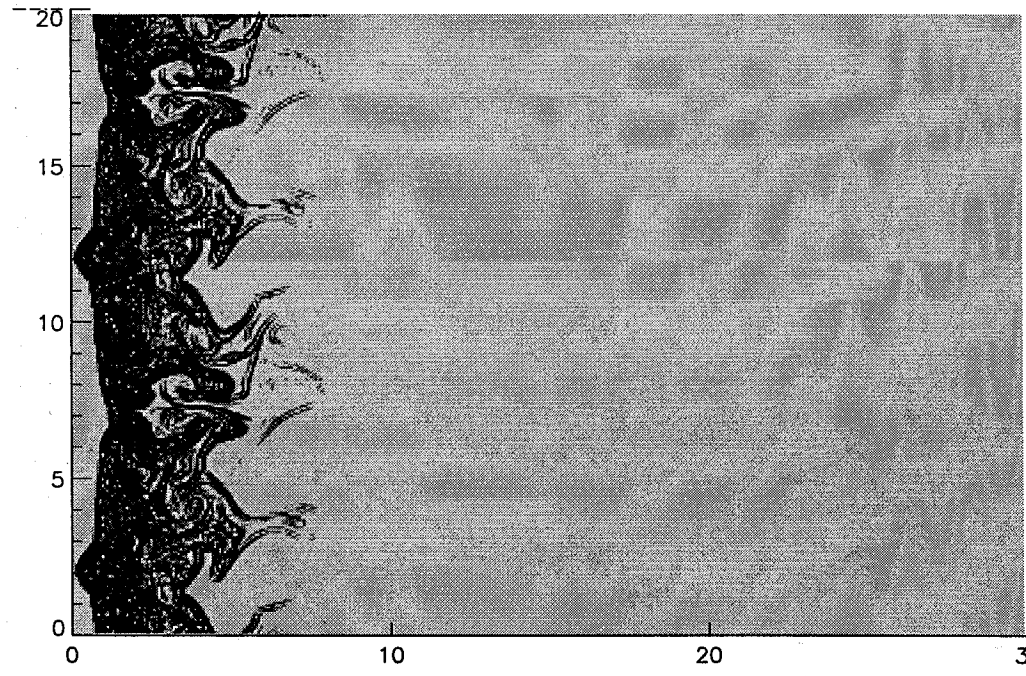

FIG.4.4d Case A: schlieren-type image of the reactant mass fraction of the detonation. Results taken at $t = 50.0$. Two periods in the y-direction are plotted.

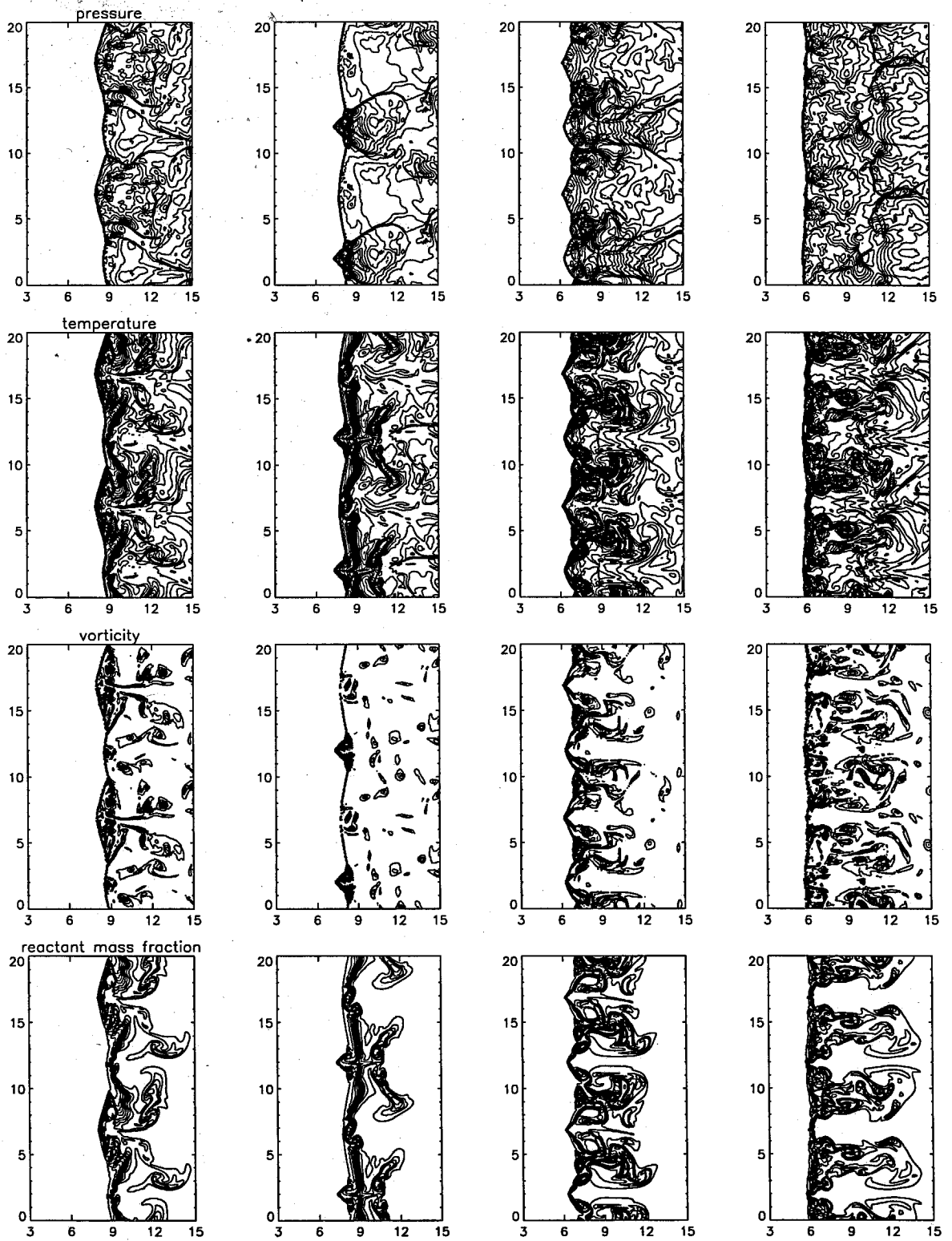

FIG.4.5a Case B: contour plots of the flow variables of the detonation. Results taken at times, from left to right, $t = 42.0, 43.0, 44.0, 45.0$. Two periods in the y-direction are plotted.

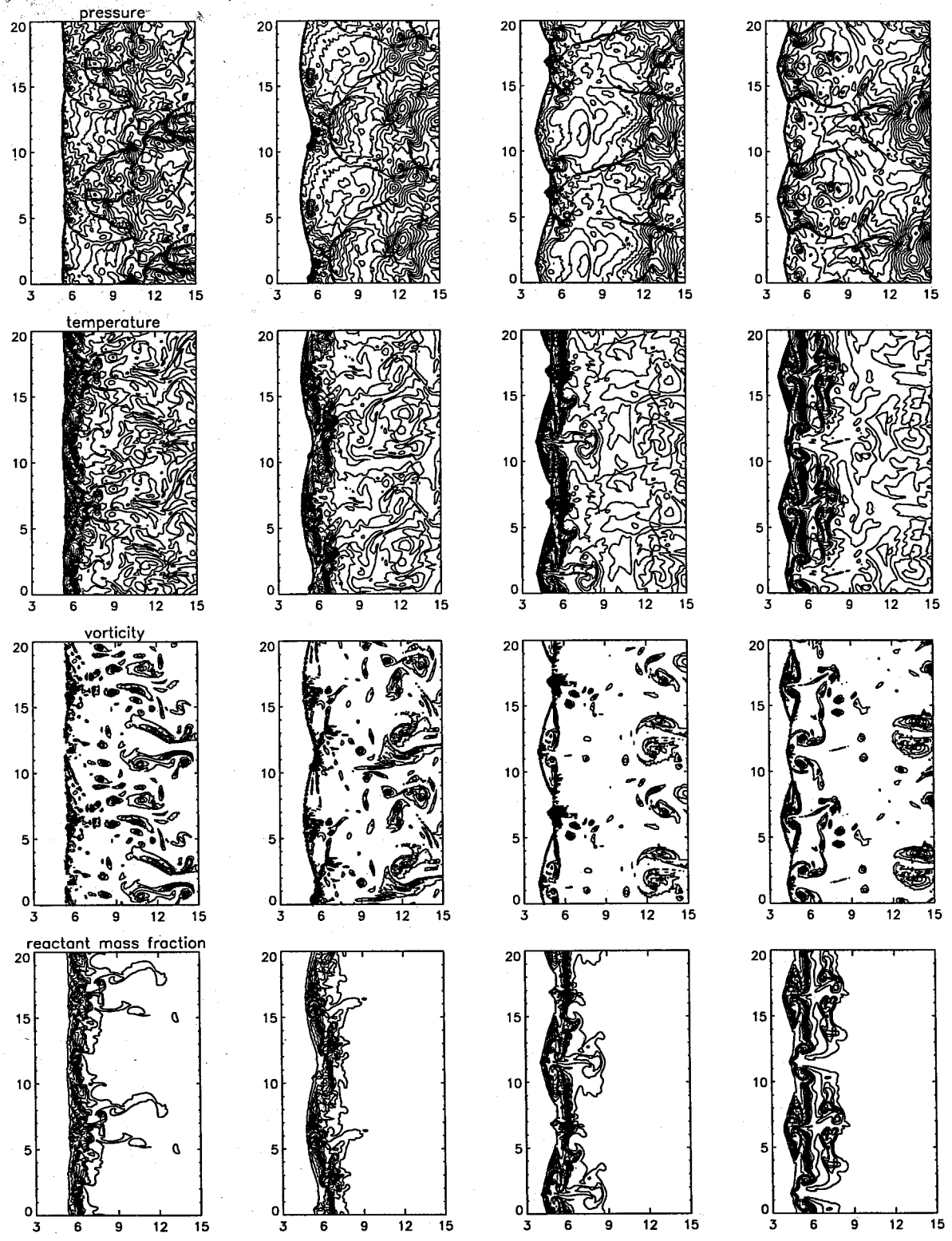

FIG.4.5b Case B: contour plots of the flow variables of the detonation. Results taken at times, from left to right, $t = 46.0, 47.0, 48.0, 49.0$. Two periods in the y-direction are plotted.

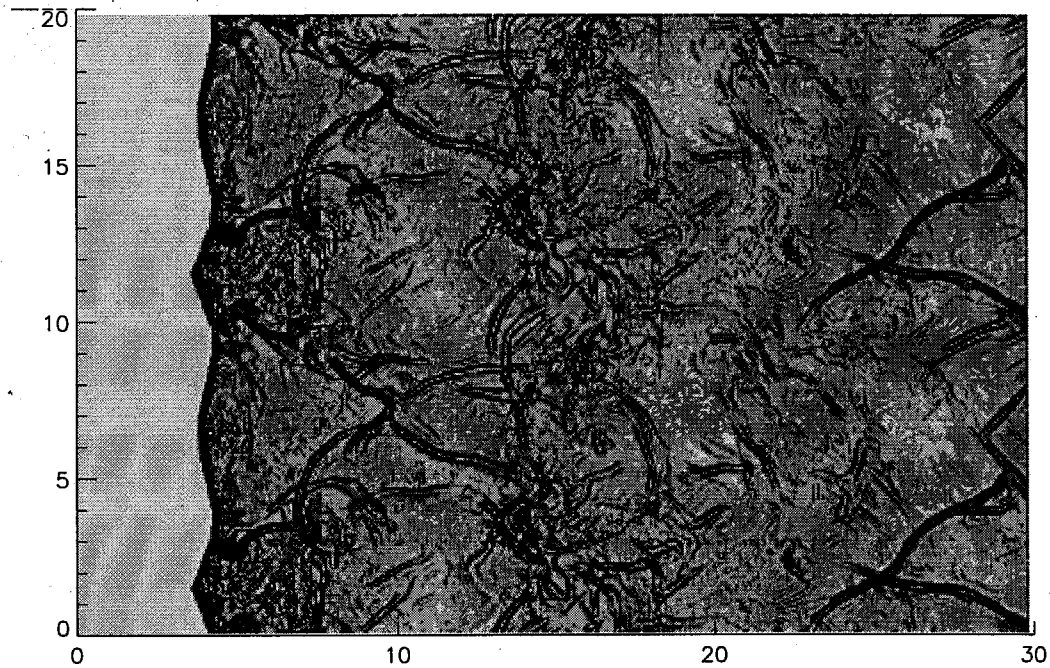

FIG.4.6a Case B: schlieren-type image of the pressure field of the detonation. Results taken at $t = 50.0$. Two periods in the y-direction are plotted.

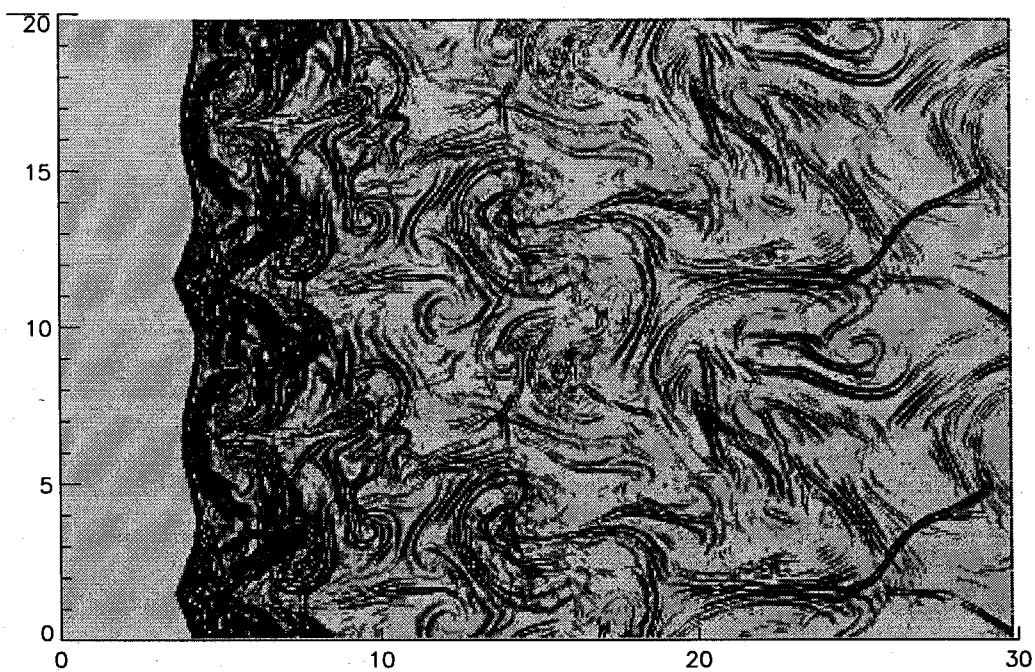

FIG.4.6b Case B: schlieren-type image of the temperature field of the detonation. Results taken at $t = 50.0$. Two periods in the y-direction are plotted.

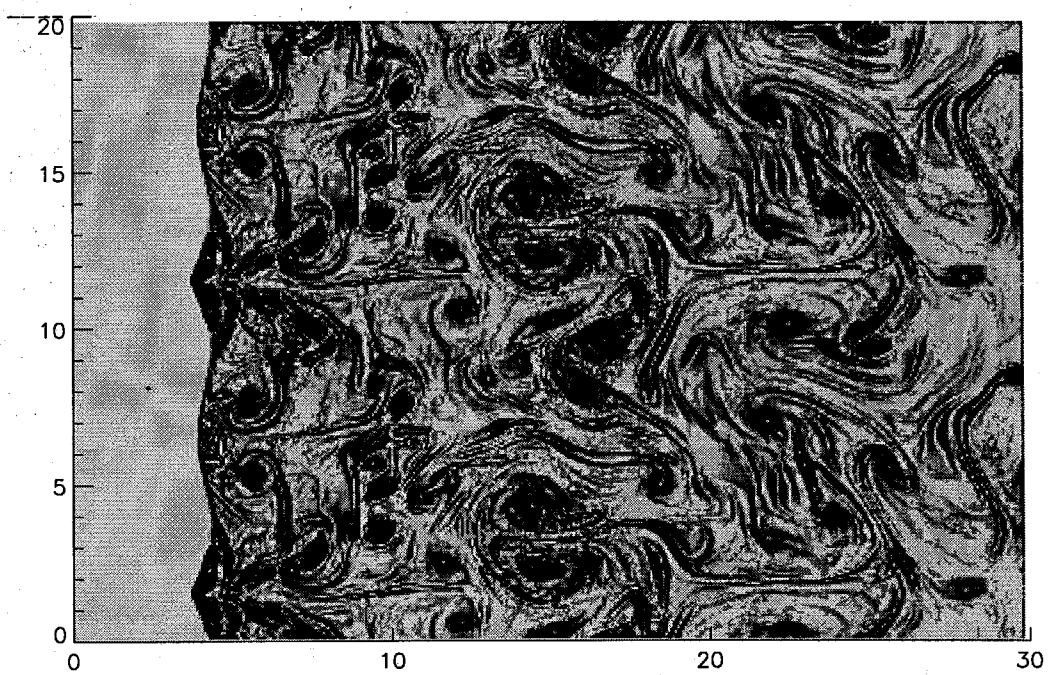

FIG.4.6c Case B: schlieren-type image of the vorticity field of the detonation. Results taken at $t = 50.0$. Two periods in the y-direction are plotted.

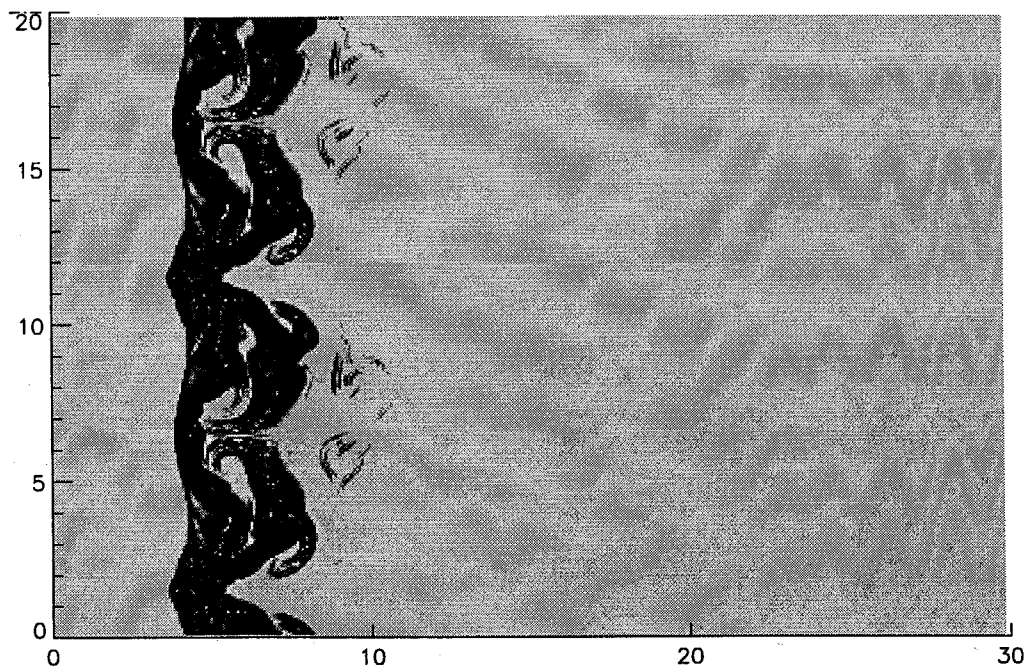

FIG.4.6d Case B: schlieren-type image of the reactant mass fraction of the detonation. Results taken at $t = 50.0$. Two periods in the y-direction are plotted.

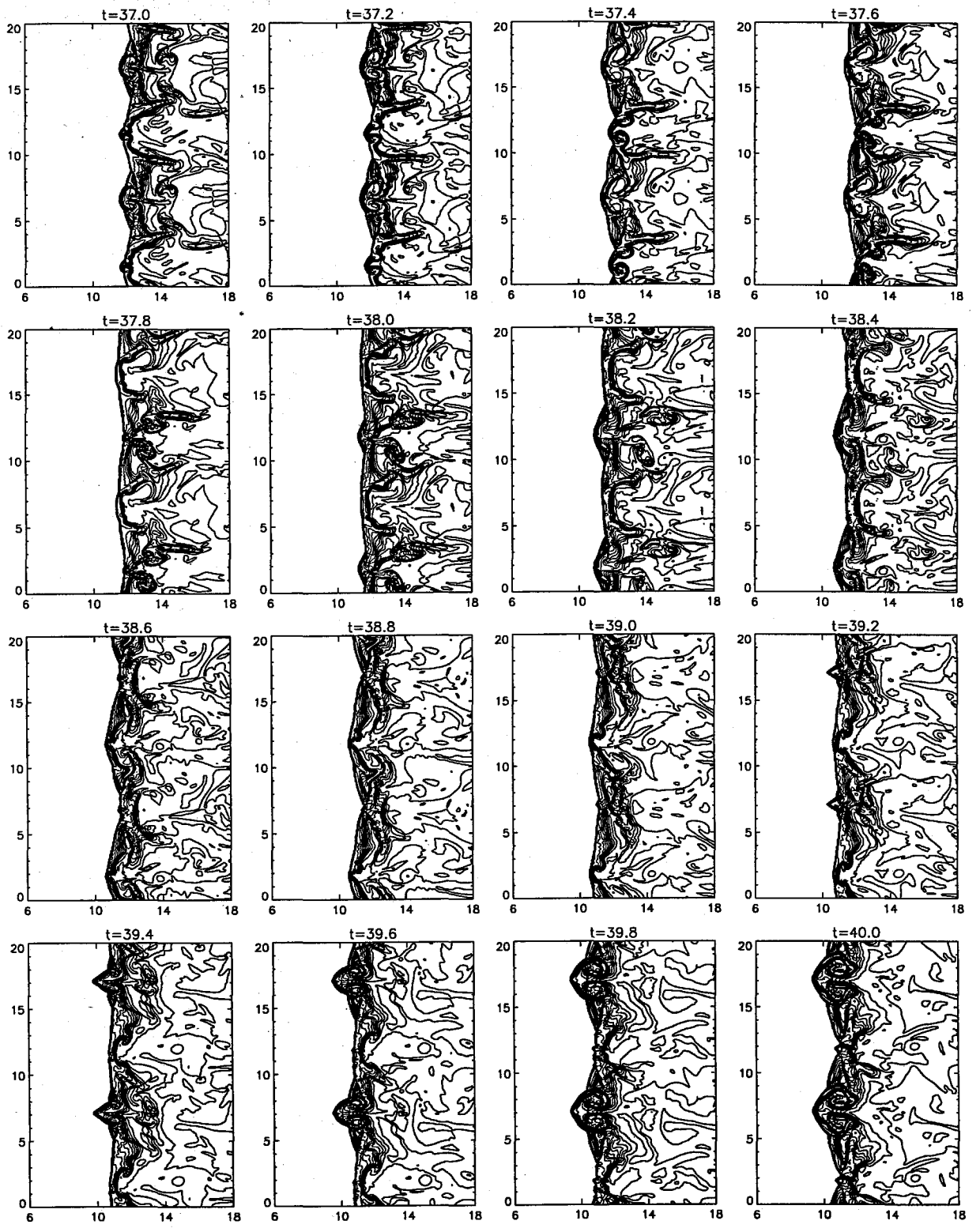

FIG.4.7 Case B: contour plots of the temperature field of the detonation, taken at various times. Two periods in the y-direction are plotted.

The corresponding one-dimensional flow is linearly unstable, with one unstable mode that results to a pulsating detonation (see the results in Chapter 2). The two-dimensional flow patterns, however, are more complicated. As in the previous cases, there is strong vorticity generation near the front, which is partially annihilated inside the reaction zone by the fluid dilatation. The reaction zone can occupy as many as 7 unit-lengths. The shock pressure of the ZND solution is $p_s = 67.35$. As discussed in Chapter 2, the shock pressure can go as high as $p_s = 98.6$ in the one-dimensional case, but its maximum value during the two-dimensional simulation is $p_s = 241.5$.

The new feature in this case is the formation of pockets of unreacted material behind the main front. Initially the unreacted material is located near the front, but the temperature is not high enough for the medium to burn completely. The incident shock and the Mach stem of the triple points, which are part of the main front, do not have the same strength. The temperature, therefore, behind the two shocks is not the same. The material behind the Mach stem burns fast. The material behind the incident shock burns slowly, and some portions of it are "trapped" in the vortex sheet that emanates from the triple point, and transported to the core of the sheet. Consequently, the vortex core consists of almost unreacted material at low temperature. It is surrounded by fast-burning material, and it detaches from the main front when a triple-point collision occurs.

The detached vortex cores are the small pockets of unreacted material that are convected downstream by the flow. Eventually these pockets burn, and the temperature of the material rises. Two shock waves emerge from the temperature rise. One is travelling towards the main front, and the other one is travelling away from it. The shock that travels towards the front collides with the neighboring transverse waves and with the main front, as soon as it gets there. Pockets of unreacted material had not been observed in higher overdrives, and they were not present in the corresponding one-dimensional case. They are a product of the interaction of transversal and longitudinal instabilities. It is worth noticing that pockets of unreacted material had been observed in one-dimensional detonations for low overdrives, near the CJ point. In the regime of low overdrives, the one-dimensional conservation equations exhibit chaotic behavior. The mechanism for formation of unreacted pockets in these detonations is different and it has been explained in Chapter 2.

Results for this case have been published by Cai (1995) who designed a hybrid algorithm consisting of an ENO scheme for regions of high gradients and a spectral scheme for smoother regions. His computational domain was wider (20 unit-lengths) than the one of the present study, and he imposed reflecting conditions at the top and bottom boundaries, instead of periodic conditions. His numerical results appear to be in qualitative agreement with the results of the present study.

4.3.4 Case D

Subsequently, the overdrive factor is lowered even more, to the regime where the one-dimensional problem has 5 unstable longitudinal modes:

$$E_a = 50.0 , \qquad f = 1.2 .$$

The stiffness coefficient for this detonation is $K = 871.42$. The computational domain of the simulation is 60 unit-lengths long and 10 unit-lengths wide. The initial ZND wave is located at $x = 5.0$. Contour plots and schlieren-type snapshots of the flow variables for this problem are given in Figs. 4.10 and 4.11, respectively. The format of these figures is the same as in the previous cases.

The two-dimensional analysis of Erpenbeck (1964) reveals that this detonation is unstable at arbitrarily short wavelengths. The transversal instabilities, combined with the longitudinal ones, are expected to lead to complicated patterns. In the early stages, the evolution of the flow-field resembles the equivalent one-dimensional process, *i.e.*, the shock pressure and temperature drop below the ZND values and, as a consequence, the reaction zone stays temporarily behind the hydrodynamic shock. Later on, the material burns fast due to thermal runaway, resulting to high over-pressures. This similarity to the one-dimensional case suggests the fact that in early times the evolution process is dominated by the longitudinal instabilities.

Once the transversal instabilities grow and start dominating the flow, the structures on the flow-field become very complicated. At the front, strong triple-point collisions occur, thus generating new systems of shock waves. In the wake of the leading front there are strong vortical structures. Pockets of unreacted material are constantly created and subsequently burn. These pockets are much larger than the pockets encountered in Case C. The ones observed in the present case are long chunks of unburnt material, almost parallel to the main front. Sometimes they can span the width of the channel.

The transverse waves of the triple points are strong and can be more than 10 lengths long. Transverse-wave collisions are encountered very often. The shock waves that are formed from these collisions interact with the vortical structures that are convected downstream from the main front. As a result, the flow-field for this detonation is very complicated and without any evident regularity, even far behind the leading front. According to the ZND theory the shock pressure is $p_s = 50.49$. In the present simulation the maximum value observed is $p_s = 220.0$. This test case was also investigated by Bourlioux & Majda (1991). Their results are in good qualitative agreement with the results obtained in the present study.

4.3.5 Case E

Finally, a case of low activation energy and low overdrive factor is presented. These parameters are set as follows:

$$E_a = 10 , \qquad f = 1.2 .$$

The stiffness coefficient for this case is $K = 3.124$. The computational domain is 60 unit-lengths long and 10 unit-lengths wide, *i.e.*, it consists of 1200×200 points. The initial ZND wave is placed at $x = 55.0$. The corresponding one-dimensional flow is stable, as one might expect for such a low activation energy. Results for this case are presented in Figs. 4.12 and 4.13, with the usual format. One can notice that the transverse waves are weaker and shorter, than the transverse waves of the previous cases. As a result, the vortex sheets are more regularly distributed in the wake of the front. The shock pressure of the ZND solution is $p_s = 50.49$, but it is found out that the maximum shock pressure during the simulation goes as high as $p_s = 144.62$. Contour plots of the temperature field for this detonation, taken at nearby times, are given in Fig. 4.14. Each plot contains 20 contours among the extremal values. It can be verified from these plots that the structure of the main front repeats itself in time. This case had been studied earlier by Bourlioux & Majda (1991) and Quirk (1995). Their results agree qualitatively with the results of the present study. Those results show that the geometry of the main front and the vorticity distribution are perfectly symmetrical about the horizontal line that intersects the main front at points of triple-point collisions. Cai (1995) had also studied this case.

It is worth noticing that simulations of the above cases with different resolutions (10 and 15 points per unit length) produced qualitatively the same but quantitatively different results. This is typical in the simulations of highly unstable (chaotic) flows, because only the instabilities whose wavelength is larger than the cell size can be captured numerically.

It should be mentioned that different widths of the computational domain have also been considered. The cases discussed above have also been computed in domains that were 5 and 15 unit lengths wide. It was observed that the size of the structures that are present in the flow-field depends on the width of the domain. It was found out that at given times there are many triple points distributed along the front. Their strength, however, is not the same. The explosions that occur when the two strongest triple points collide will dominate and spread along the front, "consuming" the other (weaker) triple points. This results in the formation of one cellular structure in the computational domain. The size of this structure scales equals the width of the domain. This can be verified at the results presented in Fig. 4.15. Contour plots of the pressure and temperature for the detonation of Case B with varying widths are presented in this figure, with the usual format. Three different domain-widths have been considered, namely 5, 10, and 15 unit lengths. Front track when the domain width is 10 unit length is presented in Fig. 4.15a, where the cellular structure of the detonation can be observed.

A summary of the description of the numerical simulations for the cases considered above is given in the following table:

Case	E_a	f	1-D linear stability	2-D behavior
A	50.0	3.0	stable	regular vortical structures, no unburnt pockets
B	50.0	2.0	stable	wide reaction zone, regular vortical structures, no unburnt pockets
C	50.0	1.6	1 unstable mode	complicated vortical structures, long transverse waves, small unburnt pockets
D	50.0	1.2	5 unstable modes	strong triple-point collisions, very long transverse waves, complicated vortical structures, large unburnt pockets
E	10.0	1.2	stable	regular vortical structures, small unburnt pockets

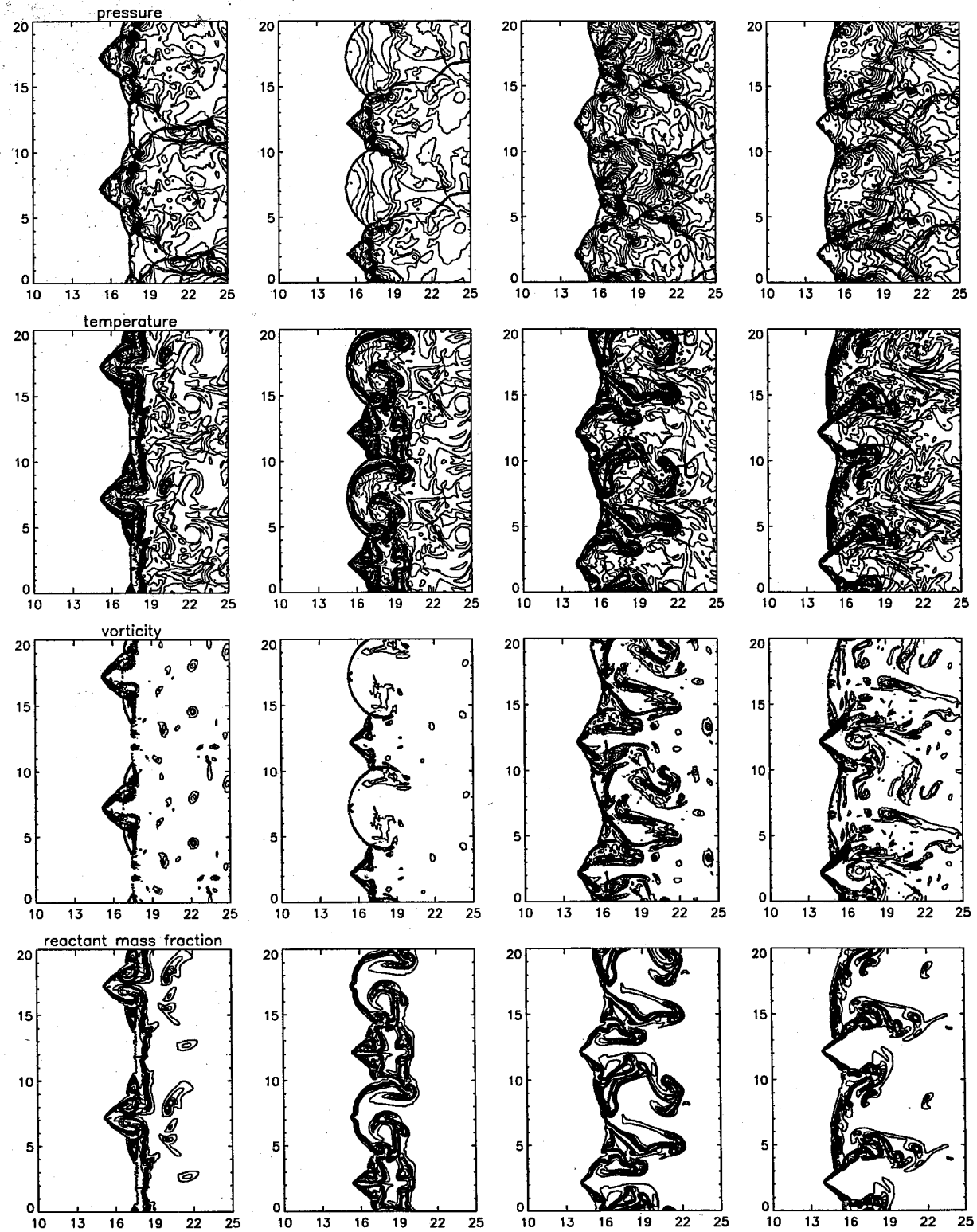

FIG.4.8a Case C: contour plots of the flow variables of the detonation. Results taken at times, from left to right, $t = 31.0, 32.0, 33.0, 34.0$. Two periods in the y-direction are plotted.

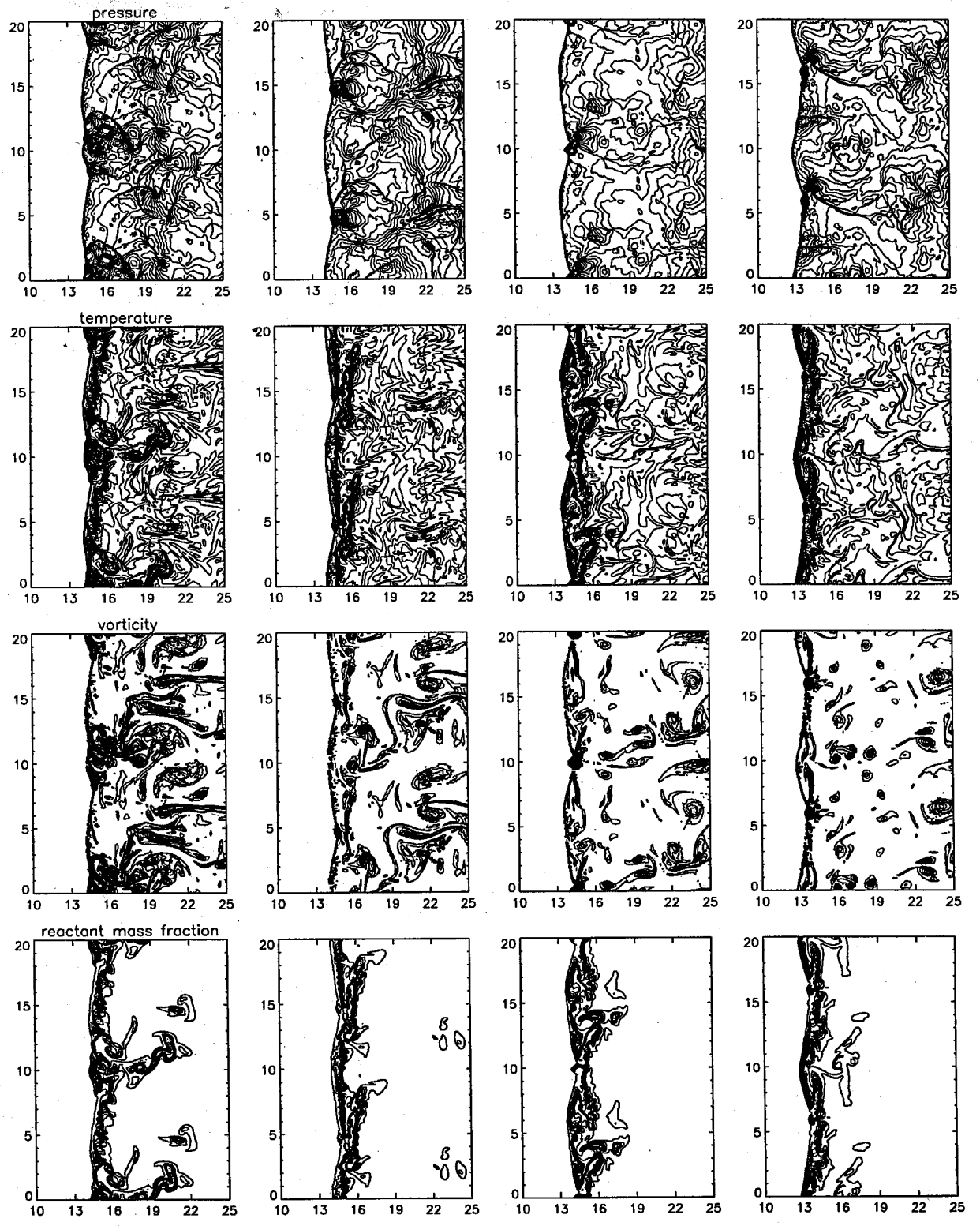

FIG.4.8b Case C: contour plots of the flow variables of the detonation. Results taken at times, from left to right, $t = 35.0, 36.0, 37.0, 38.0$. Two periods in the y-direction are plotted.

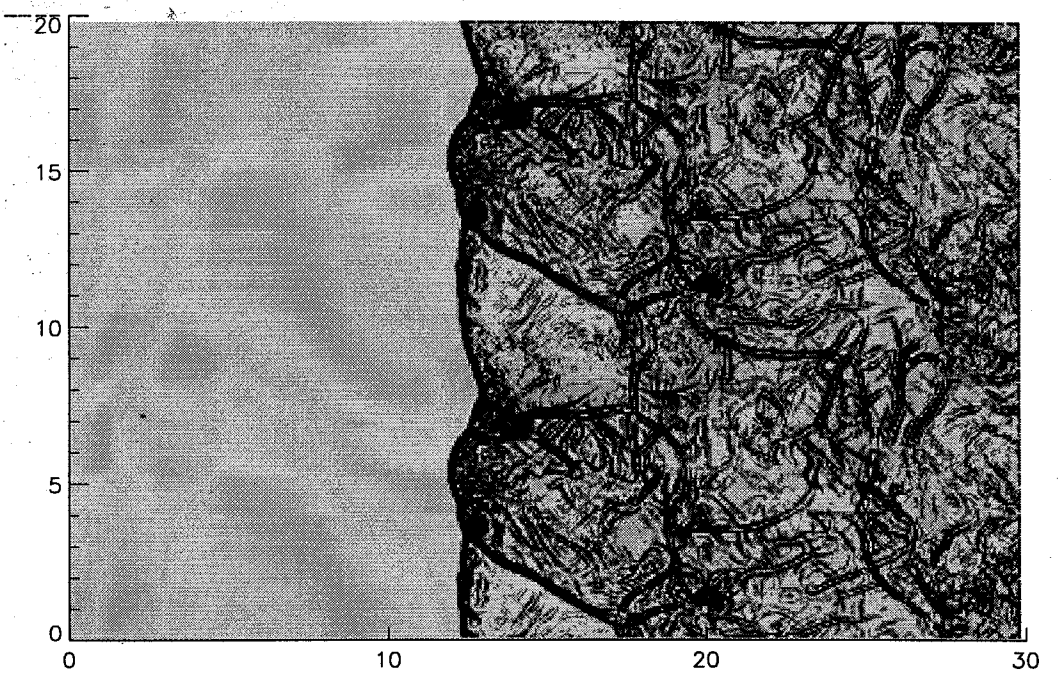

FIG.4.9a Case C: schlieren-type image of the pressure field of the detonation. Results taken at $t = 39.0$. Two periods in the y-direction are plotted.

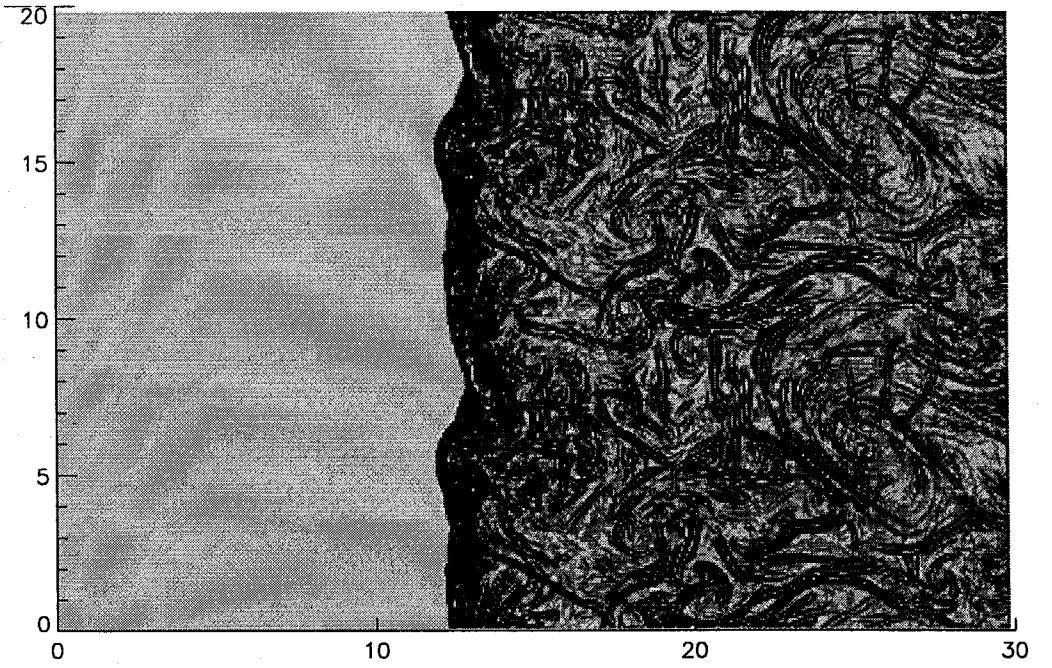

FIG.4.9b Case C: schlieren-type image of the temperature field of the detonation. Results taken at $t = 39.0$. Two periods in the y-direction are plotted.

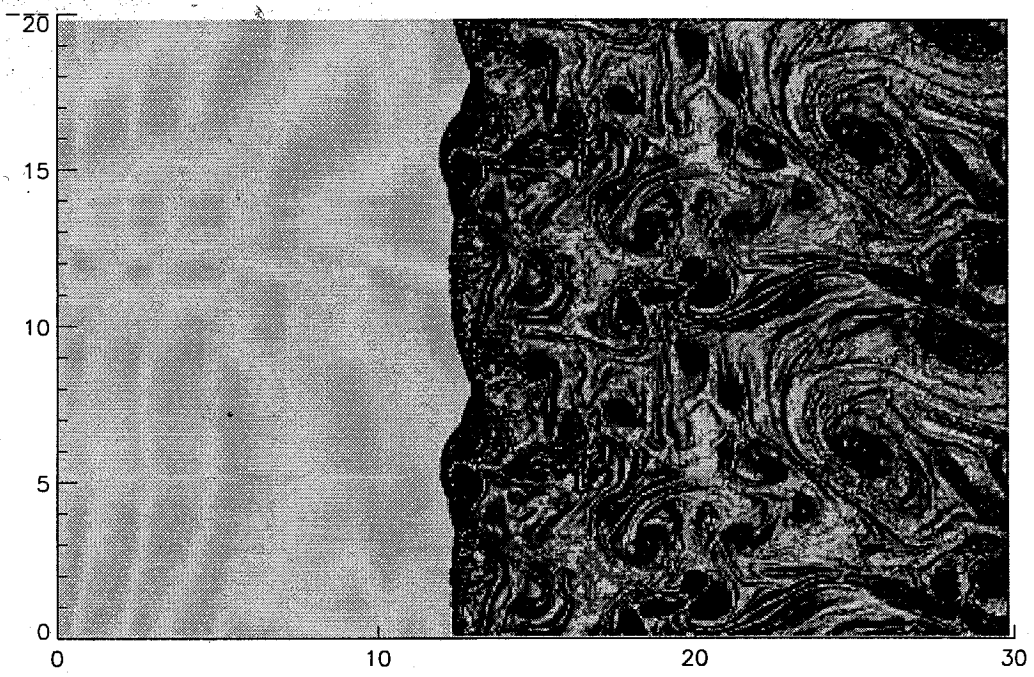

FIG.4.9c Case C: schlieren-type image of the vorticity field of the detonation. Results taken at $t = 39.0$. Two periods in the y-direction are plotted.

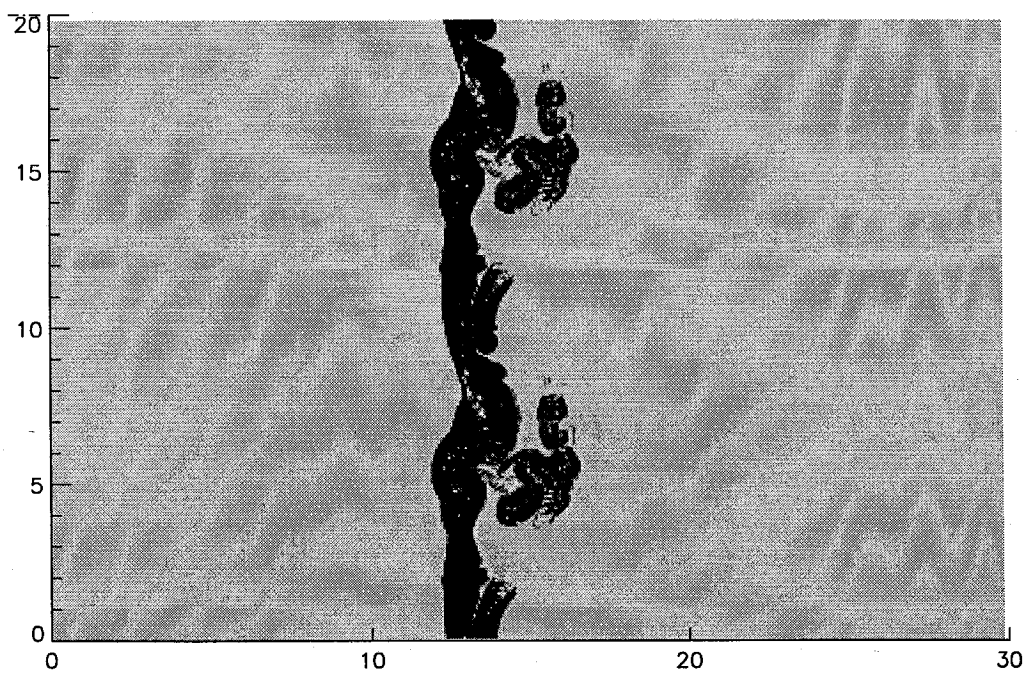

FIG.4.9d Case C: schlieren-type image of the reactant mass fraction of the detonation. Results taken at $t = 39.0$. Two periods in the y-direction are plotted.

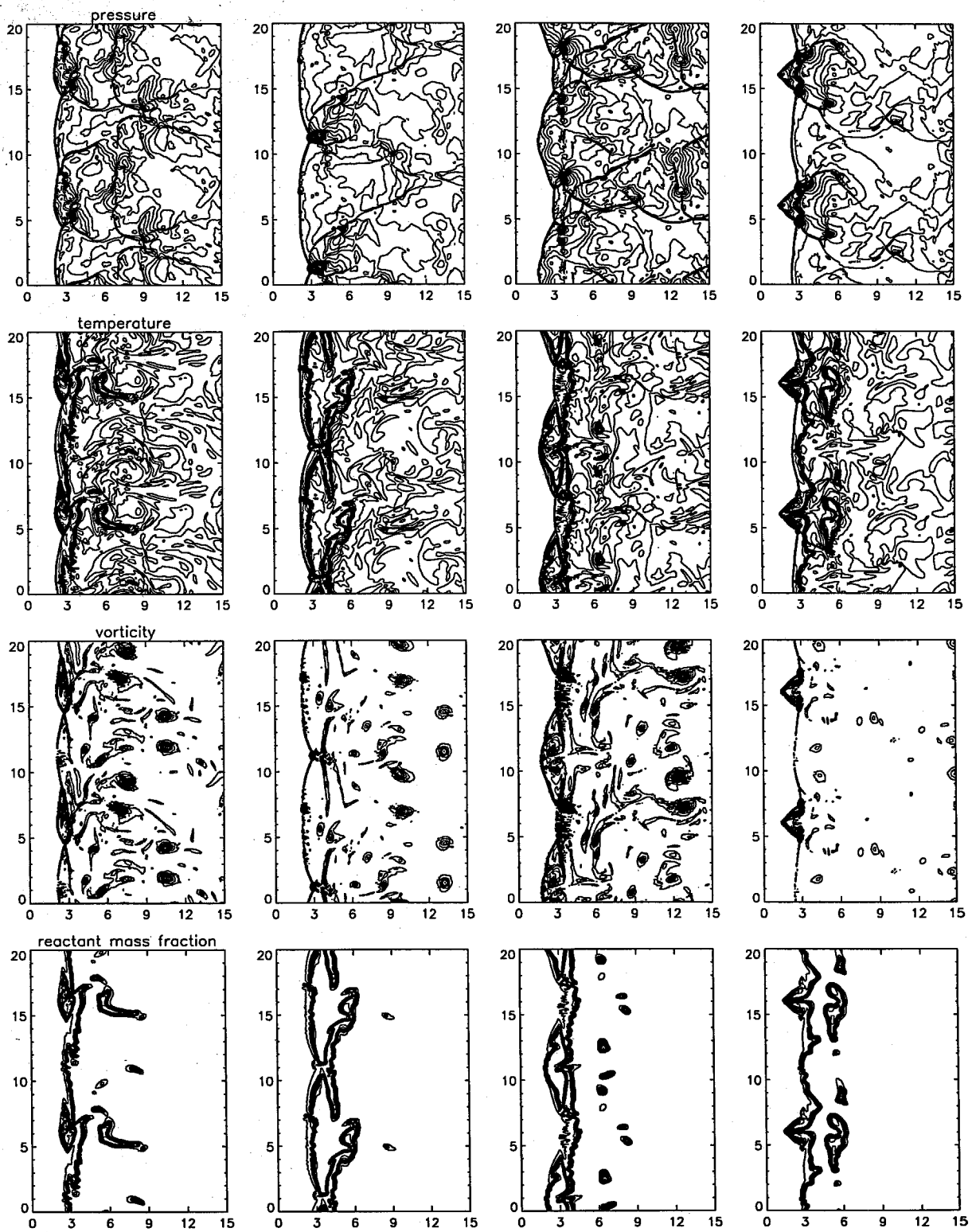

FIG.4.10a Case D: contour plots of the flow variables of the detonation. Results taken at times, from left to right, $t = 32.0$, 33.0, 34.0, 35.0. Two periods in the y-direction are plotted.

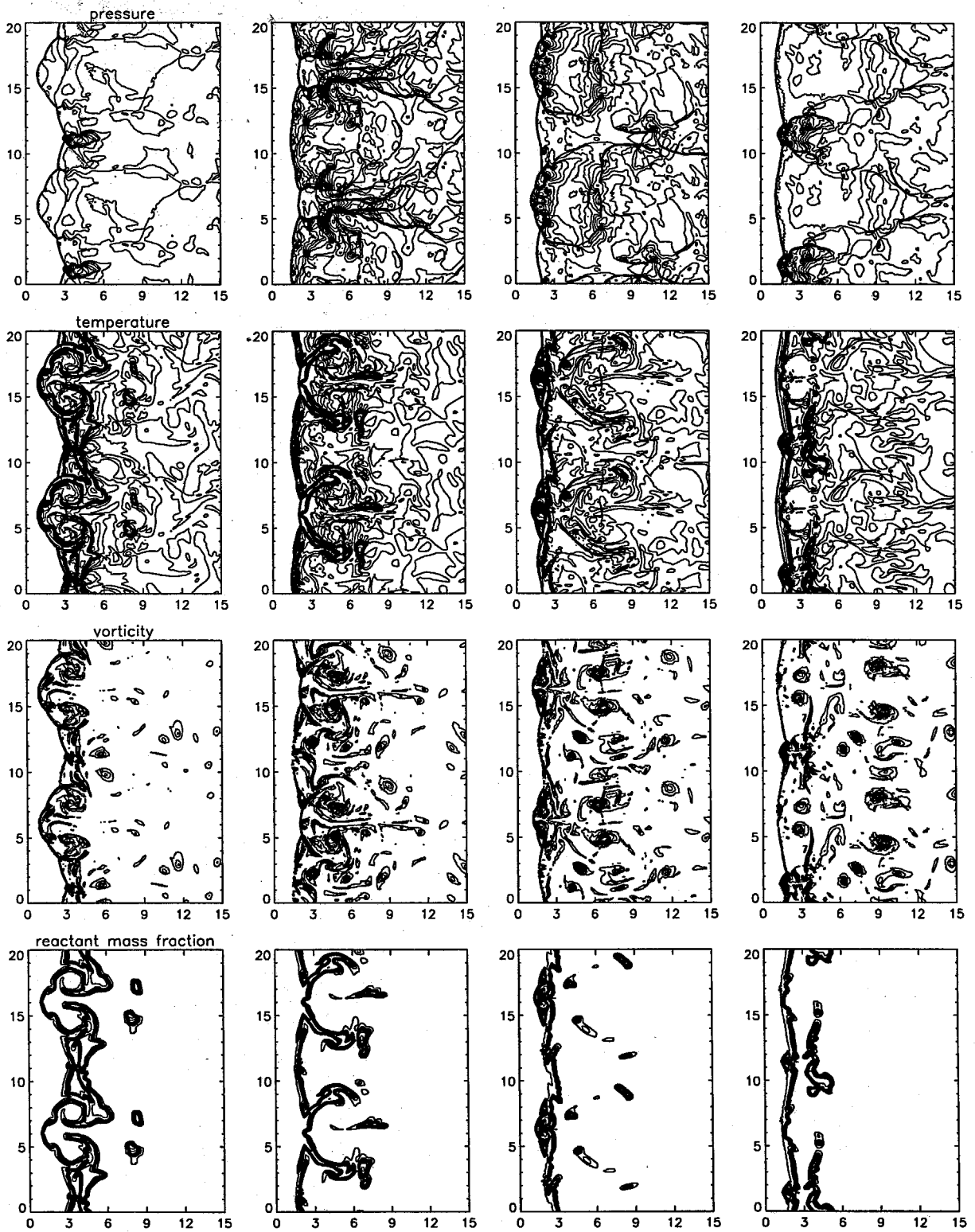

FIG.4.10b Case D: contour plots of the flow variables of the detonation. Results taken at times, from left to right, $t = 36.0, 37.0, 38.0, 39.0$. Two periods in the y-direction are plotted.

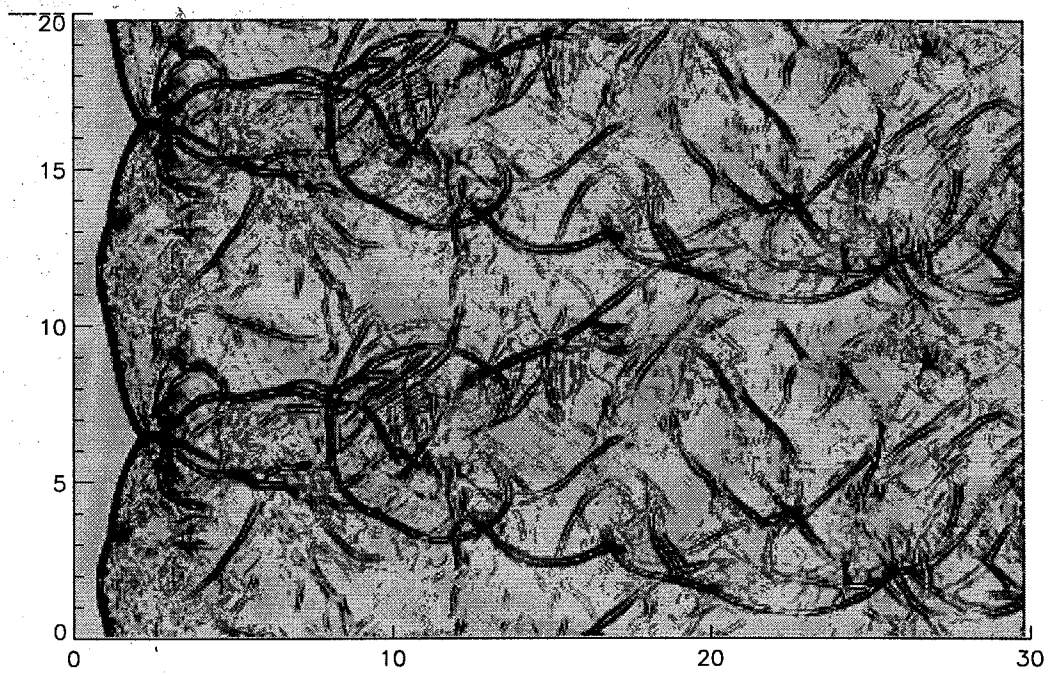

FIG.4.11a Case D: schlieren-type image of the pressure field of the detonation. Results taken at $t = 40.0$. Two periods in the y-direction are plotted.

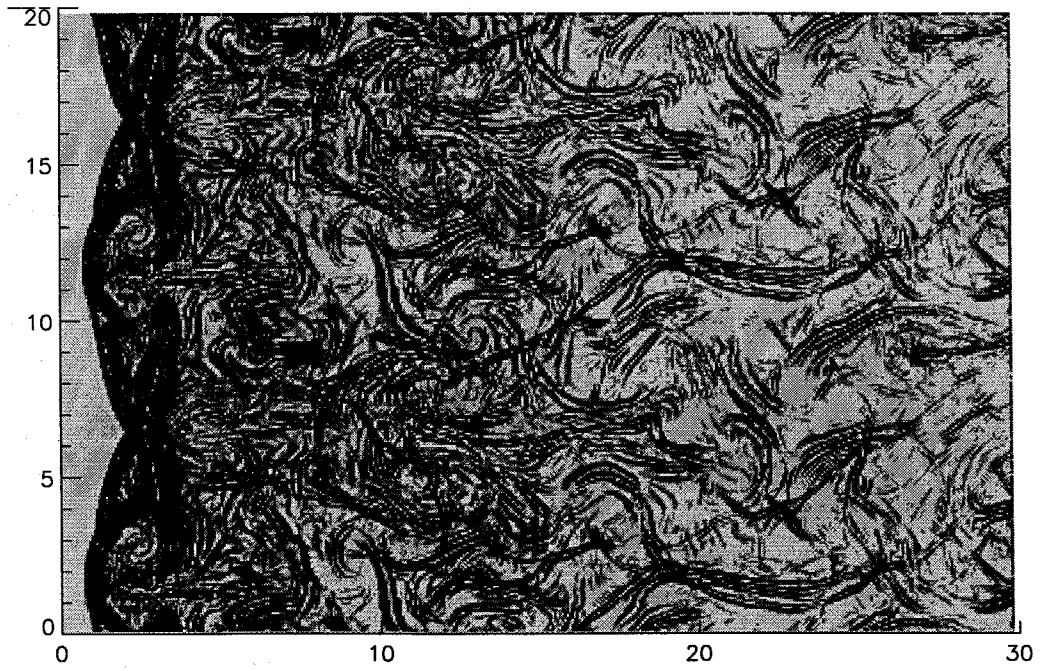

FIG.4.11b Case D: schlieren-type image of the temperature field of the detonation. Results taken at $t = 40.0$. Two periods in the y-direction are plotted.

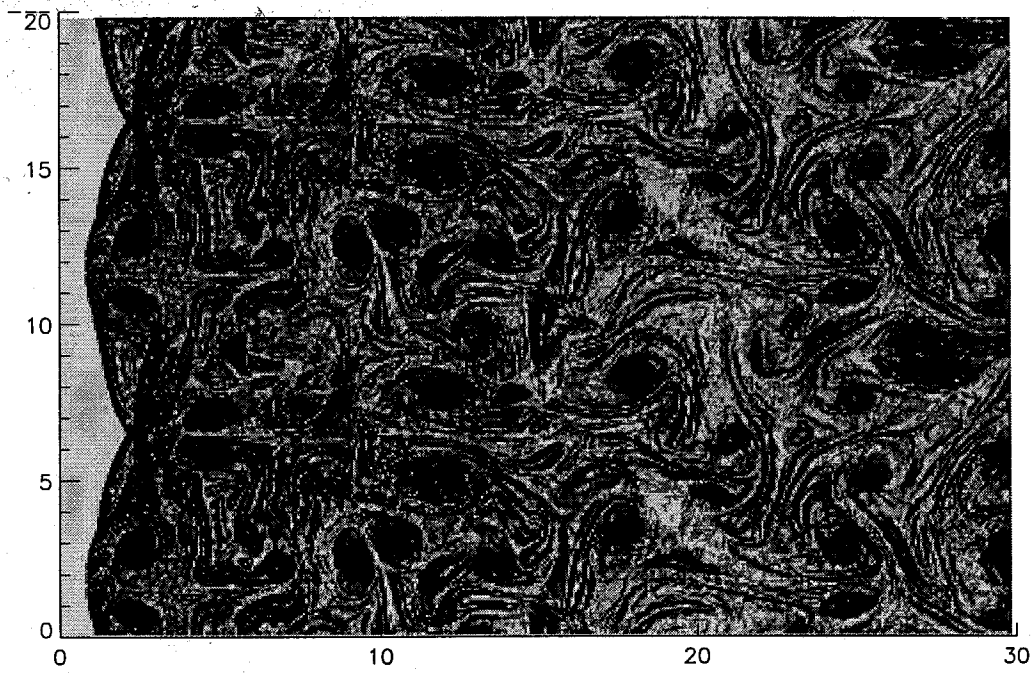

FIG.4.11c Case D: schlieren-type image of the vorticity field of the detonation. Results taken at $t = 40.0$. Two periods in the y-direction are plotted.

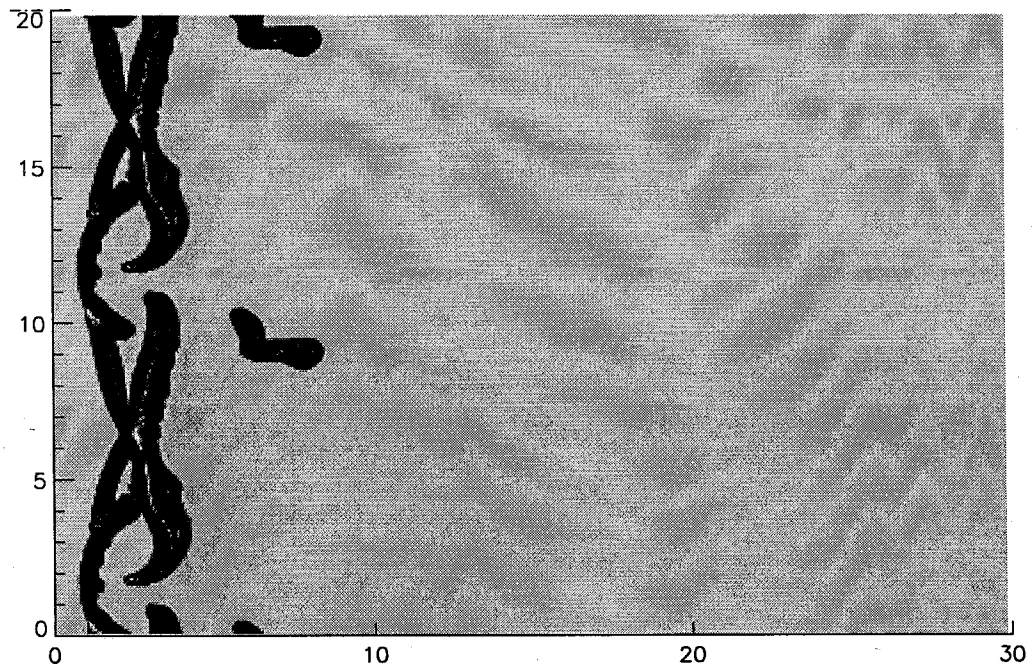

FIG.4.11d Case D: schlieren-type image of the reactant mass fraction of the detonation. Results taken at $t = 40.0$. Two periods in the y-direction are plotted.

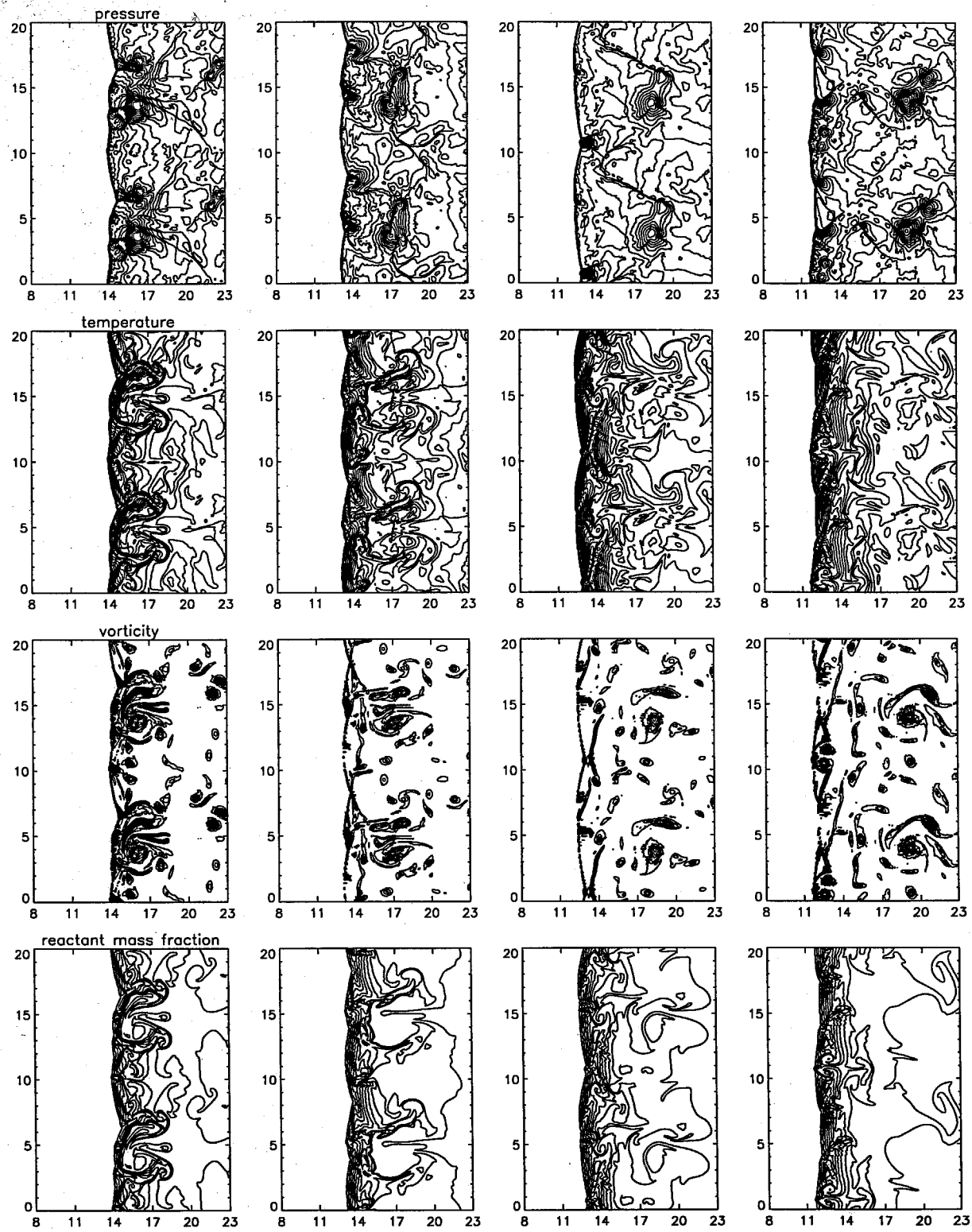

FIG.4.12a Case E: contour plots of the flow variables of the detonation. Results taken at times, from left to right, $t = 52.0, 53.0, 54.0, 55.0$. Two periods in the y-direction are plotted.

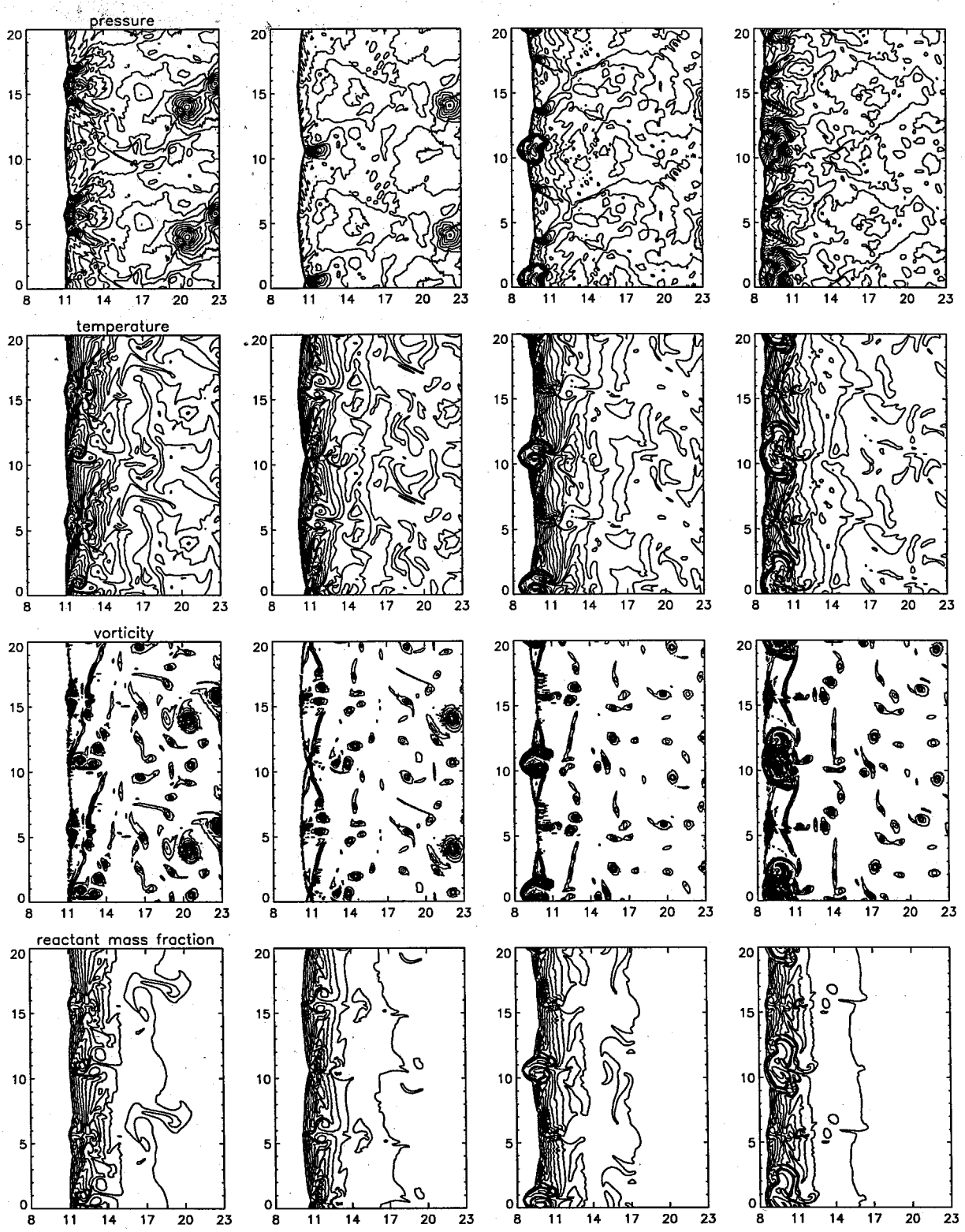

FIG.4.12b Case E: contour plots of the flow variables of the detonation. Results taken at times, from left to right, $t = 56.0, 57.0, 58.0, 59.0$. Two periods in the y-direction are plotted.

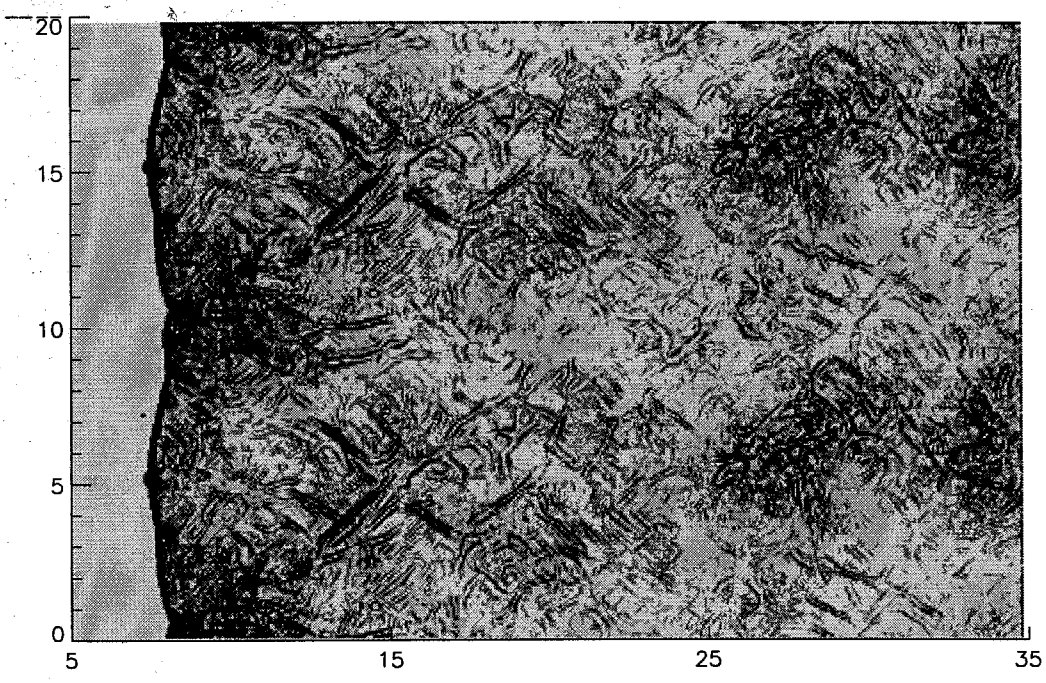

FIG.4.13a Case E: schlieren-type image of the pressure field of the detonation. Results taken at $t = 60.0$. Two periods in the y-direction are plotted.

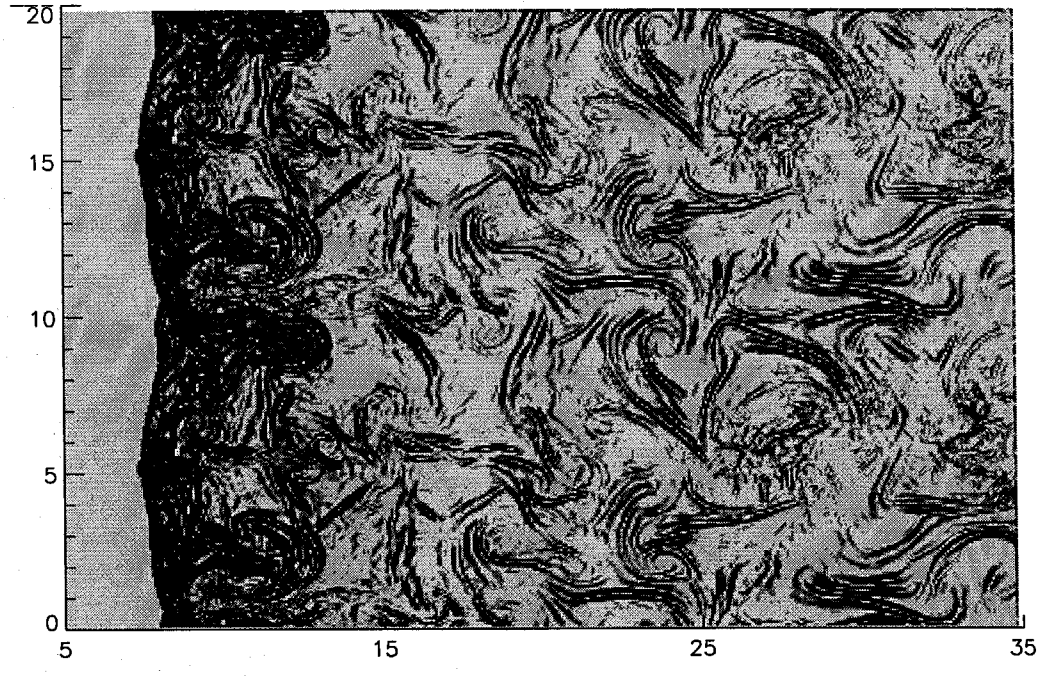

FIG.4.13b Case E: schlieren-type image of the temperature field of the detonation. Results taken at $t = 60.0$. Two periods in the y-direction are plotted.

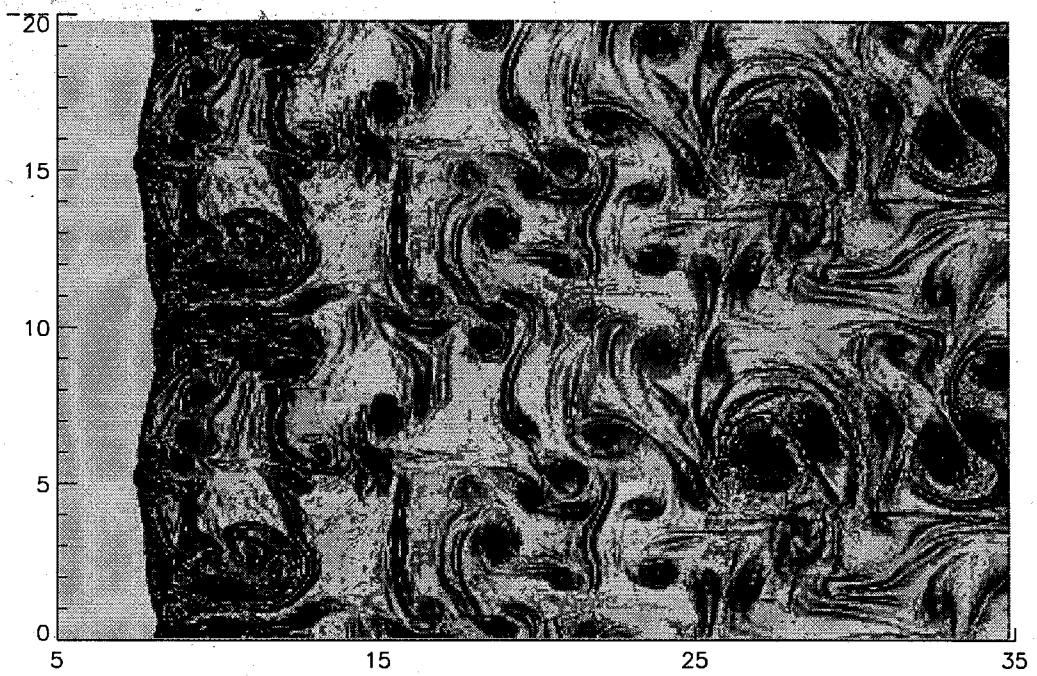

FIG.4.13c Case E: schlieren-type image of the vorticity field of the detonation. Results taken at $t = 60.0$. Two periods in the y-direction are plotted.

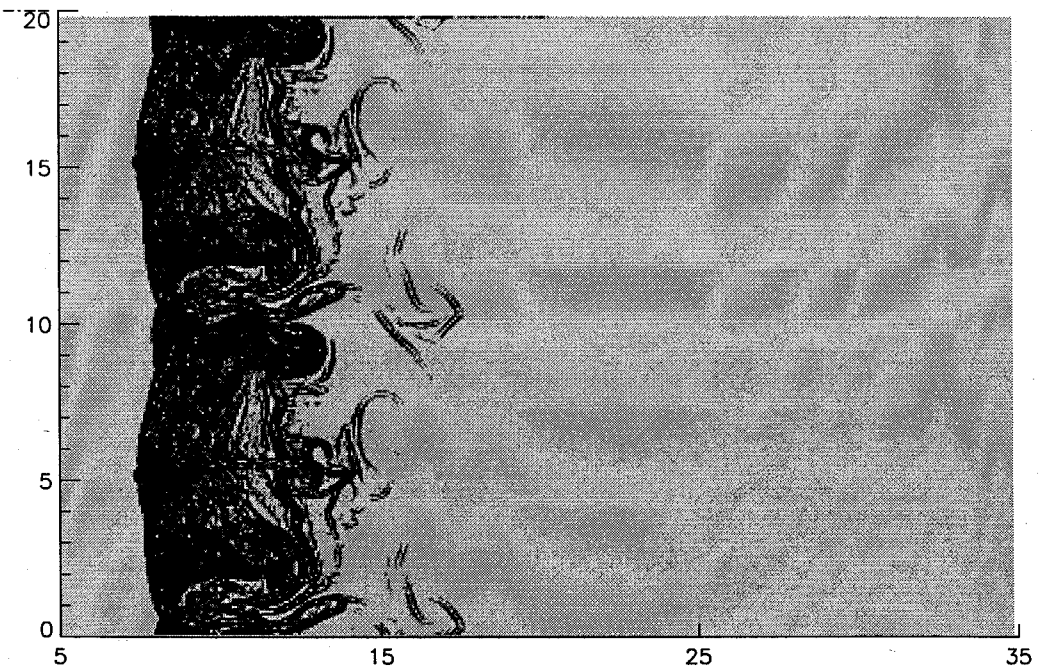

FIG.4.13d Case E: schlieren-type image of the reactant mass fraction of the detonation. Results taken at $t = 60.0$. Two periods in the y-direction are plotted.

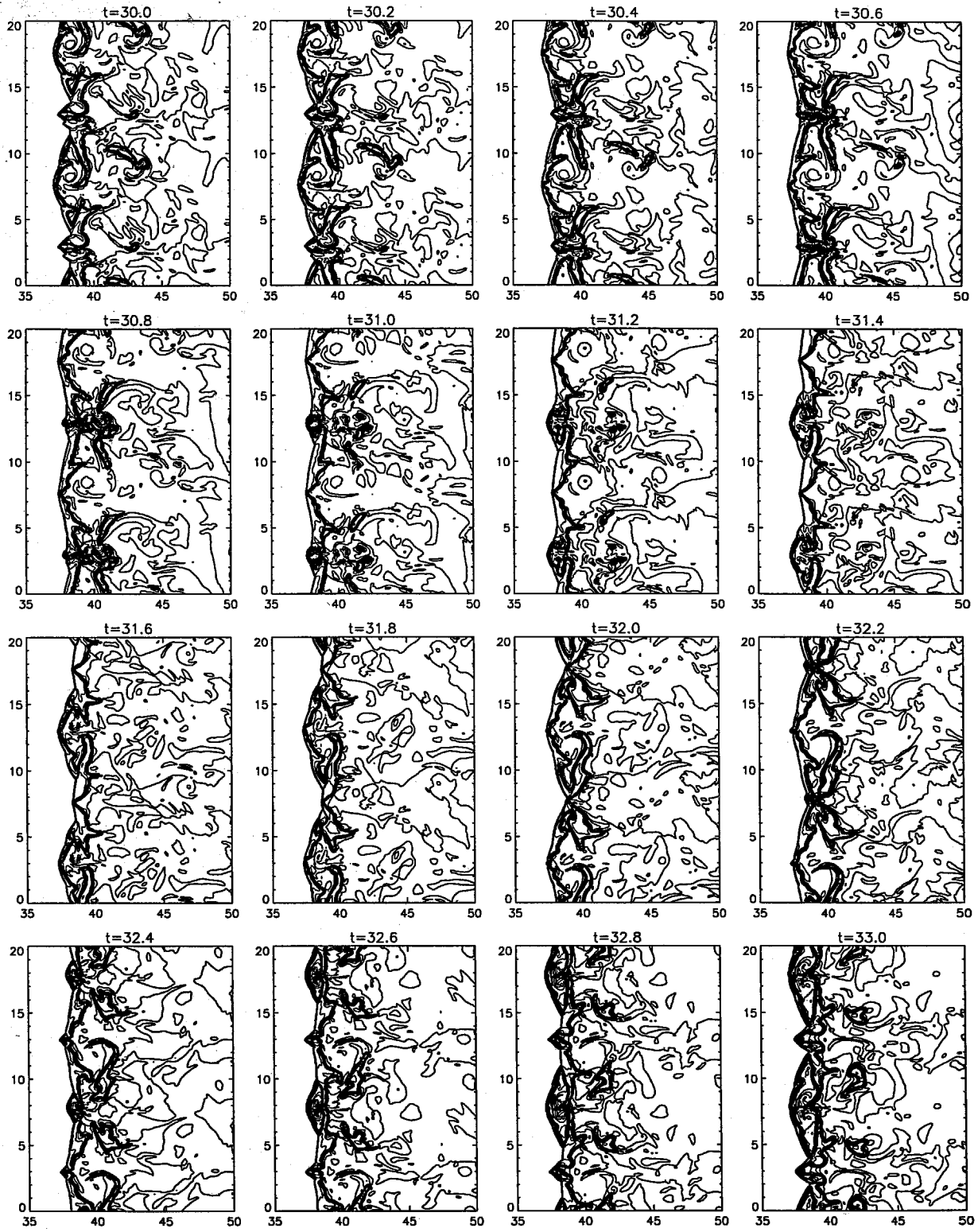

FIG.4.14 Case E: contour plots of the temperature field of the detonation, taken at various times. Two periods in the y-direction are plotted.

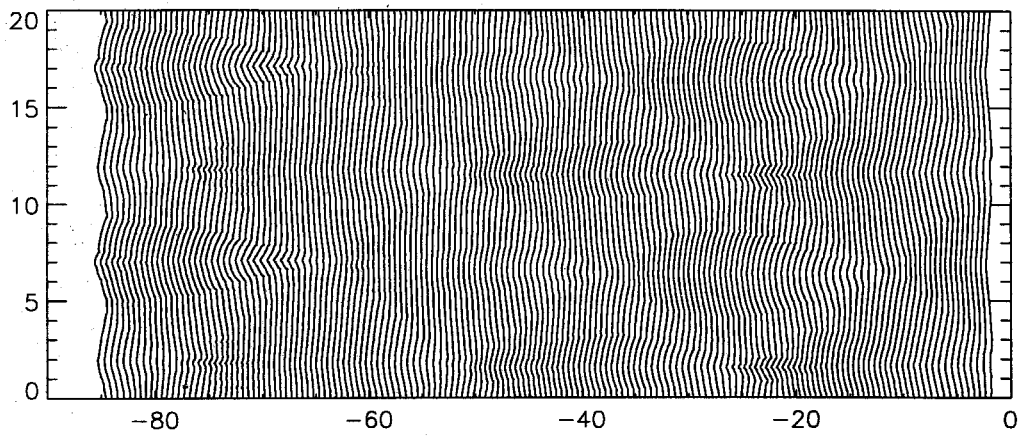

FIG.4.15a Case B: front track. The shock propagates to the left. Width of the domain, 10 unit lengths. Two periods in the y-direction are plotted.

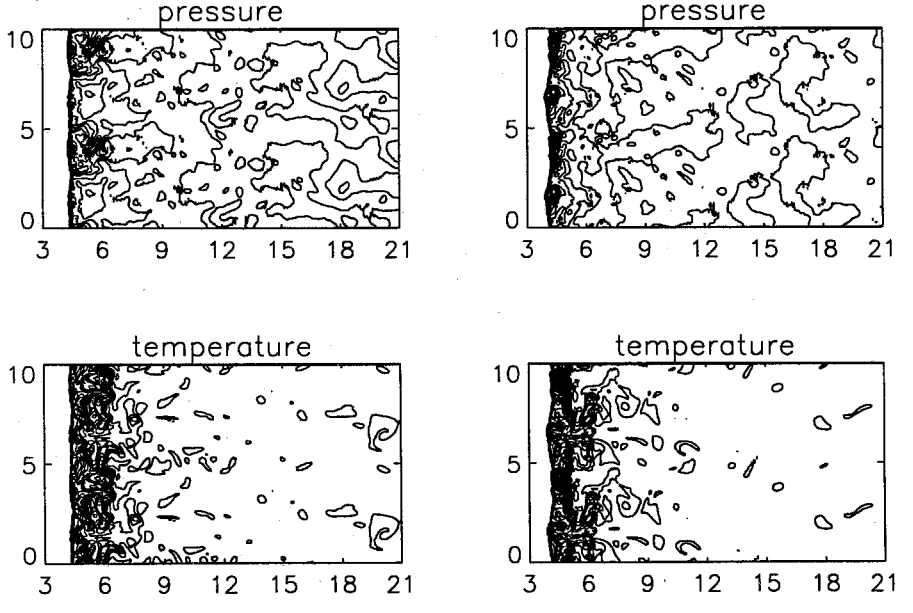

FIG.4.15b Case B: contour plots of the pressure and temperature fields of the detonation, taken at $t = 48.0, 49.0$. Width of the domain, 5 unit lengths. Two periods in the y-direction are plotted.

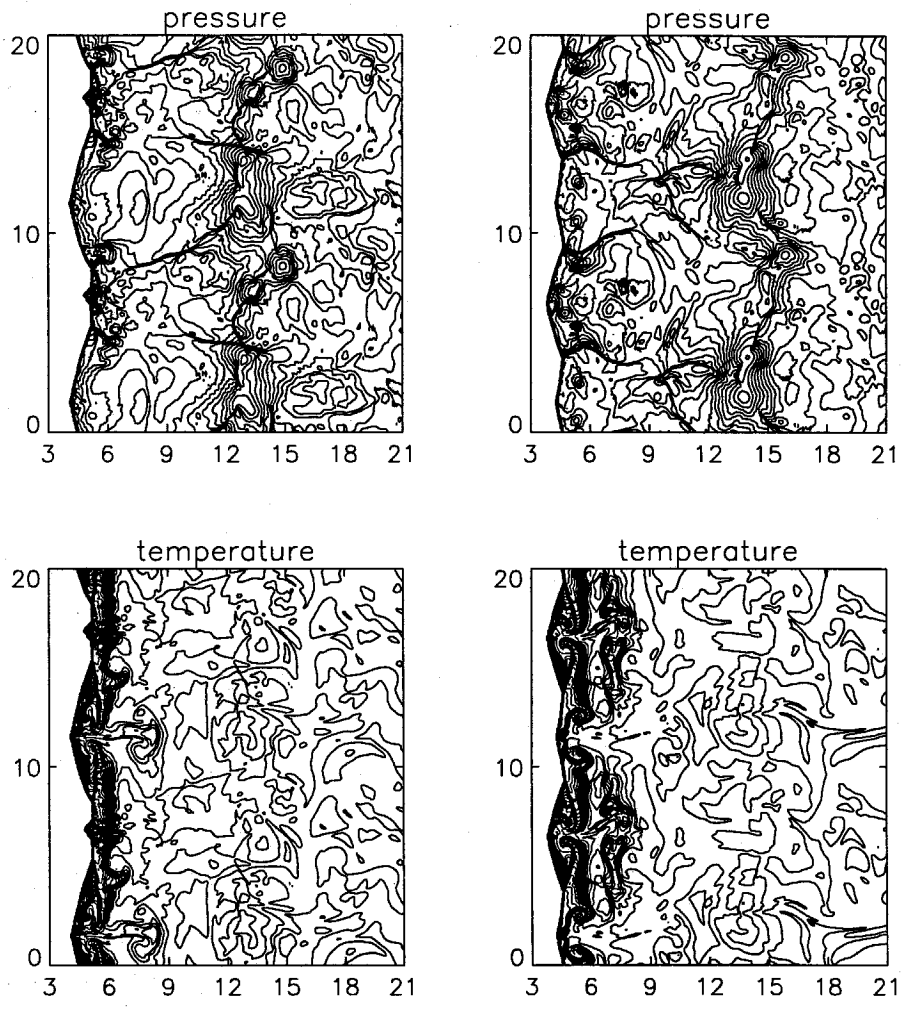

FIG.4.15c Case B: contour plots of the pressure and temperature fields of the detonation, taken at $t = 48.0, 49.0$. Width of the domain, 10 unit lengths. Two periods in the y-direction are plotted.

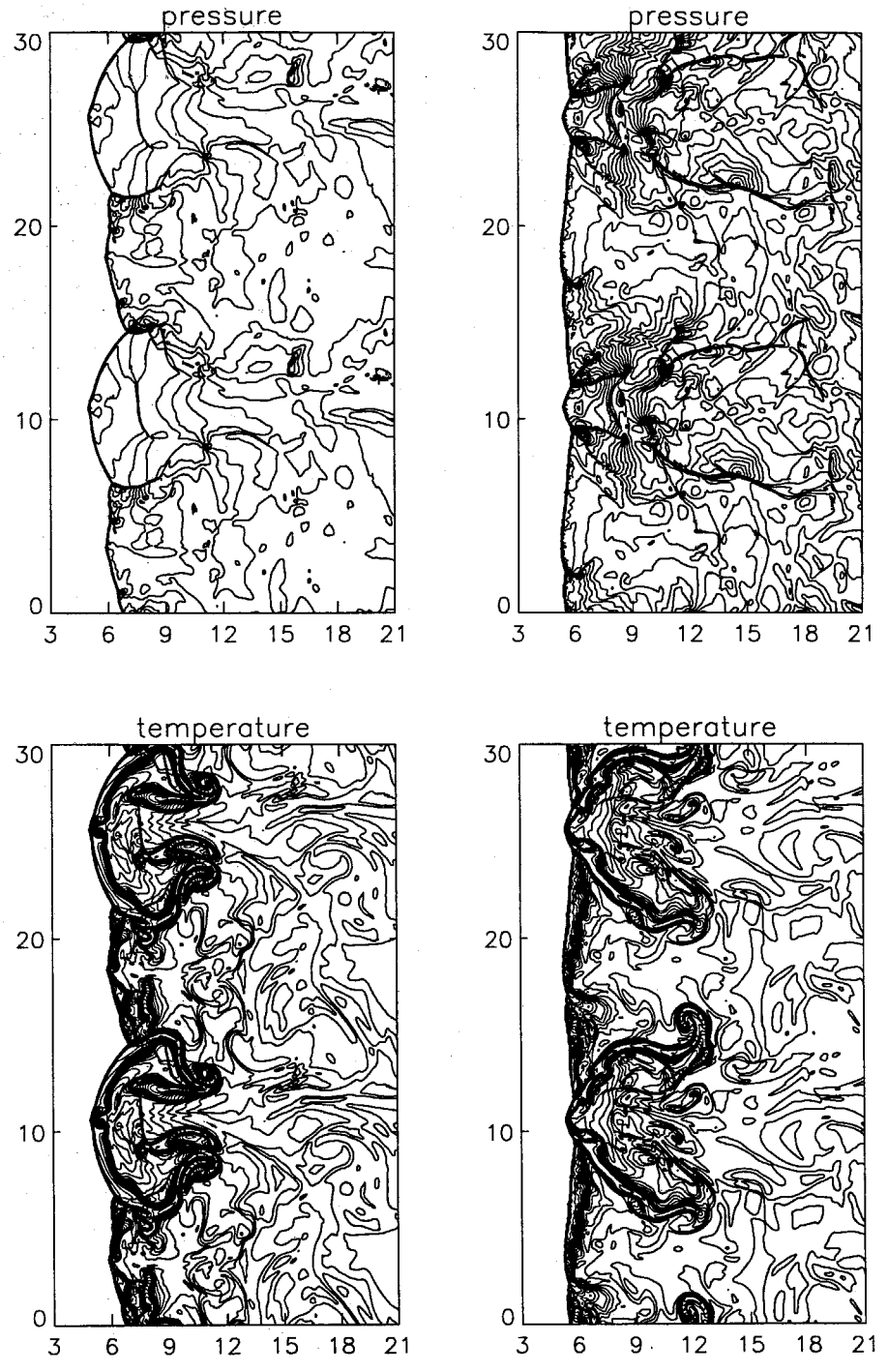

FIG.4.15d Case B: contour plots of the pressure and temperature fields of the detonation, taken at $t = 48.0, 49.0$. Width of the domain, 15 unit lengths. Two periods in the y-direction are plotted.

4.4 Numerical Study of Wedge-Induced Detonations

In this section, numerical simulations of wedge-induced detonations, using the proposed unsplit scheme, are presented. The wedge is placed instantly in uniform flow of a reactive gas. A shock is immediately formed at the wedge. If the surrounding gas were inert, this shock would oblique, at a prescribed angle with respect to the centerline of the wedge. But because the gas is assumed to be reactive, the shock is curved due to the dilatation of the reacting material behind the shock. A detonation might be established downstream if the shock temperature is high enough.

The wedge angle, θ, is an important parameter of this problem. It is expected that for small wedge angles the shock turns smoothly and the flow far downstream consists of an oblique ZND wave, *i.e.*, a ZND wave with a non-zero transversal velocity component. For small wedge angles, both the inert and the equilibrium shock-polars admit solutions for the shock angle, β. The shock near the tip is essentially inert and its angle can be computed from the inert shock-polar. The angle of the ZND wave, far downstream, can be computed from the equilibrium shock-polar. Given the state ahead of the shock, denoted by the subscript "1", one can determine the flow variables behind the shock, denoted by the subscript "s", by employing the standard kinematic relations for oblique shocks:

$$F \equiv \frac{1+\gamma M_{1n} \pm \sqrt{(M_{1n}^2-1)^2 - 2(\gamma+1)M_{1n}^2\, q_0/(c_p T_1)}}{(\gamma+1)M_{1n}^2}\,, \tag{4.1a}$$

$$\frac{\rho_1}{\rho_s} = F = \frac{\tan(\beta-\theta)}{\tan\beta}\,, \tag{4.1b}$$

$$p_s = p_1 + u_1^2(1-F)\sin^2\beta\,, \tag{4.1c}$$

where M_{1n} is the normal Mach number ahead of the shock:

$$M_{1n} \equiv \frac{u_1 \sin\beta}{\sqrt{\gamma T}}\,. \tag{4.2}$$

For wedge angles larger than a certain value (but small enough so that the equilibrium shock-polar admits a solution for β), the shock can not turn smoothly, and a strong explosion is expected to occur on the front. This explosion is caused by the interaction of pressure waves inside the reaction zone. These pressure waves are emitted from the points at which the material near the wedge burns rapidly due to thermal runaway.

4.4.1 Detonation induced by long wedges

Three different cases have been examined numerically. Schematic of the geometrical configuration and the computational domain is given in Fig. 4.16. The wedge is assumed to be long so that the wedge corner has no effect on the flow-field near the reaction zone. Inflow conditions have been assigned at the left boundary and at the first 7 cells of the bottom boundary. Reflecting conditions have been assigned at the rest of the bottom boundary, and outflow conditions have been assumed at the top and right boundaries. The flow at these boundaries is supersonic, and one must ensure that all information for the evaluation of the boundary fluxes comes from inside the domain. This is performed by copying the values from the boundary cells to their corresponding dummy cells.

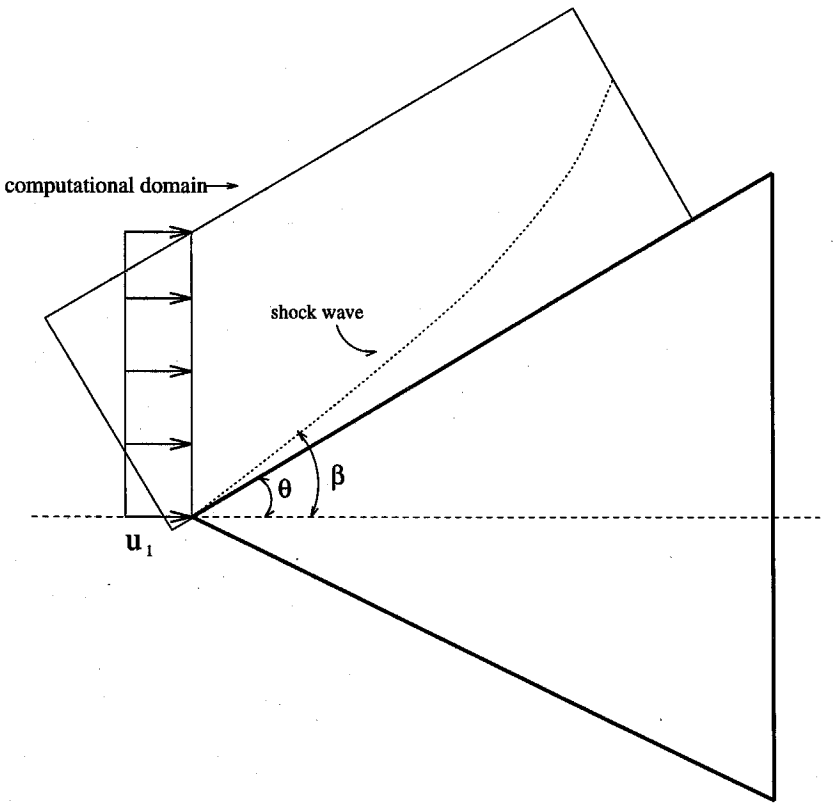

FIG.4.16 Schematic of the computational domain for the problem of a detonation induced by a long wedge.

The values of the specific heat ratio, γ, and the heat release coefficient, q_0, are set as follows:

$$\gamma = 1.2\,, \qquad q_0 = 50\,.$$

Upstream, the pressure and density of the gas are equal to unity. All the variables and parameters of the system of equations have been made dimensionless with respect to this upstream state. The results of the simulations are plotted with the same format that was used in the previous section, *i.e.*, contour plots of the pressure, temperature, vorticity, and reactant mass fraction are presented. Each plot consists of 30 contours, equally distributed between the extremal values, except of the plots of the reactant mass fraction which contain 11 contours, at the levels $z = 0.01\,, 0.1\,, 0.2, \ldots,$ 0.9, 0.99. The CFL number for these simulations is set to 0.70.

Case A

This is a low activation energy case:

$$E_a = 10\,, \qquad K = 3.1245\,.$$

As a first test, the wedge angle is set to $\theta = 20°$. The upstream velocity of the gas is $u_1 = 12.171$. Given these parameters and upstream conditions, the theoretical prediction is that far downstream this detonation reduces to an oblique ZND wave of overdrive factor $f = 1.2$ and at an angle $\beta = 34.02°$. The equivalent channel-flow problem was examined in the previous section (case E).

The computational domain consists of 960 × 400 cells. This corresponds to a nominal resolution of 8 points per half-reaction length for the steady (ZND) solution. In this simulation the shock wave turns smoothly until it reaches the asymptotic angle. Contour plots for this case are presented in Fig. 4.17a. These plots are taken at $t = 24.0$. No change on the flow variables is observed at later times, which implies that the part of the flow-field that is covered by the computational domain reaches a steady state.

In the area near the tip of the wedge, the shock is essentially inert. The pressure and particle velocity in this region are almost constant along a streamline, and the gas reacts due to the phenomenon of thermal runaway. The temperature increase across the oblique shock is small and, consequently, the source term in the species equation remains too small to initiate rapid reaction. This source term, however, is not zero, so the material burns very slowly.

The region of slow burning is the induction zone. At the end of the induction zone, the temperature has risen high enough to initiate and sustain fast burning of the gas. As a result of the fast burning of the material near the wedge, pressure waves are transmitted to the shock front. These waves interact with the slow-burning region behind the shock, causing the fluid particles to burn faster and dilate, and the shock front to turn. Recall that the phenomenon of thermal runaway was also encountered in the study of one-dimensional detonations near the CJ point. It is responsible for the formation of pockets of unreacted material in such flows, as discussed in Chapter 2.

Next, the wedge angle is increased to $\theta = 27°$. This is the maximum angle for which the equilibrium shock-polar admits a solution for β. For a detonation of overdrive factor $f = 1.2$ to occur, the upstream velocity has to be $u_1 = 9.255$. The asymptotic limit of the shock angle is readily found to be $\beta = 53.7°$. The computational domain for this simulation consists of 1020×402 cells, with a nominal resolution of 6 points per half-reaction length. Contour plots of the variables for this problem, at $t = 50.0$, are given in Fig. 4.17b. It can be observed in these plots that several triple points have been formed along the leading front. These triple points move with different velocities. Therefore, collisions between the triple points will eventually occur (most likely outside the area covered by the computational mesh), thus forming the cellular structures that were studied in the previous section. Formation of triple points should have been observed in the previous simulation (when $\theta = 20°$), had the computational domain been large enough.

Case B

The activation energy and the stiffness coefficients are now set at:

$$E_a = 50 , \qquad K = 99.762 .$$

The wedge angle is $\theta = 20°$. The upstream velocity is $u_1 = 20.58$. Theoretically, the shock angle tends asymptotically to a shock angle $\beta = 27.9°$. At this limit the detonation is an oblique ZND wave of overdrive factor $f = 2.0$. The equivalent channel-flow problem was also examined in the previous section (case B).

Three different resolutions have been used for this problem. In the first test the computational domain consists of 285×60 cells, Fig. 4.18a. In the second test it

consists of 570×120 cells, Fig. 4.18b. In the final test it consists of 1140×240 cells, Fig. 4.18c, corresponding to a nominal resolution of 6 points per half-reaction length of the one-dimensional, steady-state solution. Again, the shock turns smoothly until it reaches a steady state, very close to the asymptotic limit. The results presented in Figs. 4.18 are taken at $t = 18.0$. By this time, the solution has already reached the steady state. It is expected, however, that formation of triple points occurs further downstream. Unfortunately, the current constraints on the computational resources did not allow the use of a domain large enough to include the region where triple-point formations occur. It can be observed that the same steady-state solution has been computed with all three meshes. As expected, the shock profiles on the coarse meshes are more smeared than the ones on the fine mesh.

Next, the wedge angle is increased to $\theta = 35°$, which is near the maximum angle for which the equilibrium shock-polar admits a solution. As before, three different mesh sizes have been used for this problem, consisting of 560×64 cells, 560×128 cells, and 1140×240 cells, respectively. The finer computational domain corresponds to a nominal resolution of 8 points per half-reaction length. The upstream velocity is $u_1 = 11.509$. The asymptotic limit is a detonation with overdrive factor $f = 1.2$ and at an angle $\beta = 56.8°$. Results for this simulation, taken at $t = 50.0$, are given in Figs. 4.18d, 4.18e, and 4.18f. The flow can not turn smoothly in this case, because of the high value of the wedge angle.

As a result, a strong explosion takes place at the front. The center of the explosion is a triple point. The incident shock and the Mach stem are the two parts of the main front, below and above the triple point respectively. Another shock emanates from the triple point, the reflected shock, which hits the wedge and reflects back. Additionally, a contact discontinuity (shear layer) is formed between the Mach stem and the reflected shock. The material behind the incident shock burns due to thermal runaway, but the material behind the Mach stem burns fast because of the high temperature rise due to the explosion. Consequently, there is a strong density and temperature gradient across the shear layer. The shear layer becomes unstable very quickly and generates strong vortical structures that are convected downstream, as seen in 4.18f. Diffusion in these simulations is introduced by the discretization of the equations and the truncation error of the scheme. Consequently, the size and the velocity of the vortical structures are determined by the the size of the grid and the implicit artificial viscosity of the algorithm. The convective Mach

number for the shear layer lies between $0.5 \sim 0.7$, so the layer can be considered slightly compressible.

It is worth mentioning that the flow between the incident shock and the wedge is steady. Furthermore, the region between the shear layer and the Mach stem is subsonic in the vicinity of the triple point. A sonic line emanates from the triple point and moves along the shear layer. After some distance the sonic line turns upward and ends up in the Mach stem. Beyond this pocket, the flow becomes supersonic and should have all the typical characteristics of planar detonations, such as formation of colliding triple points and transverse waves, and vorticity generation at the main front. Qualitatively, the results on the three different meshes are the same. Interestingly, the location of the explosion at the front is the same regardless of resolution. The results on the coarse meshes, however, are more diffusive than than the ones on the fine mesh: the shock profiles are more smeared, and the structures of the shear layer and the reaction zone are not sufficiently resolved.

Since the equilibrium shock-polar admits a solution for the shock angle β, it is expected that far downstream the Mach stem reduces to an oblique ZND wave, at an angle $\beta = 56.8°$. The instability mechanisms that were encountered in detonations in channel flows (and lead to the formation of triple points) should also appear on the flow-field of oblique detonations: as demonstrated in the previous section, two-dimensional detonations are intrinsically unstable. This region, however, is too far downstream to be included in the computational domain.

It should be noted that for higher wedge angles, the equilibrium shock polar can not give a solution for β. In such situations, a strong explosion of the main front is also expected to occur. But since there is no solution to the equilibrium shock-polar, the Mach stem can not reduce to an oblique ZND wave downstream, and it is everywhere curved. For even higher wedge angles, none of the shock-polars admits a solution, and the main front detaches from the wedge. Such high wedge angles have not been considered in the present work.

Case C

The activation energy is the same as in case B, but the stiffness coefficient has now been increased:

$$E_a = 50 , \qquad K = 230.75 .$$

The wedge angle is $\theta = 20°$. The upstream velocity is $u_1 = 18.051$. The theoretical prediction is that far downstream the detonation will be a ZND wave of overdrive factor $f = 1.60$ and at an angle $\beta = 28.5°$. The equivalent channel-flow problem was examined in case C of the previous section. The computational domain consists of 1200×200 cells, corresponding to a nominal resolution of 8 points per half-reaction length of the one-dimensional, steady-state solution. As in case B, the shock turns smoothly until it reaches a steady state. Contour plots of the flow variables are given in Fig. 4.19a. These results are taken at time $t = 18.0$. No change in the flow variables could be observed after that time. The shock angle at the right boundary is very close to the asymptotic limit $\beta = 28.5°$.

The case of a higher wedge angle, namely $\theta = 30°$, has also been considered. The computational domain consists of 1440×240 cells, corresponding to a nominal resolution of 8 points per half-reaction length. The upstream velocity is now set at $u_1 = 12.035$. Under this initial condition, the theoretical prediction is a detonation of overdrive factor $f = 1.6$, at a shock angle $\beta = 45.7°$. Results for this simulation, taken at time $t = 36.0$, are given in Fig. 4.19b. These results are similar to the ones obtained in the high-angle simulation of case B. The basic features that were encountered earlier on (such as the explosion on the front, the development of an unsteady shear layer, and the formation of a subsonic pocket behind the Mach stem in the vicinity of the triple point) can also be observed in this simulation.

It is worth mentioning that Li *et al.* (1994) also presented simulations for wedge-induced detonations using the FCT algorithm, on a domain of 400×150 cells. Their numerical results seem to agree qualitatively with the results obtained with the proposed unsplit algorithm. In particular, they also observed that for small wedge angles the main front turns smoothly, while an explosion occurs at the front if large wedge angles are considered. More detailed comparisons between the two studies can not be made because Li *et al.* considered a different combustion model and did not use dimensionless quantities for their simulations.

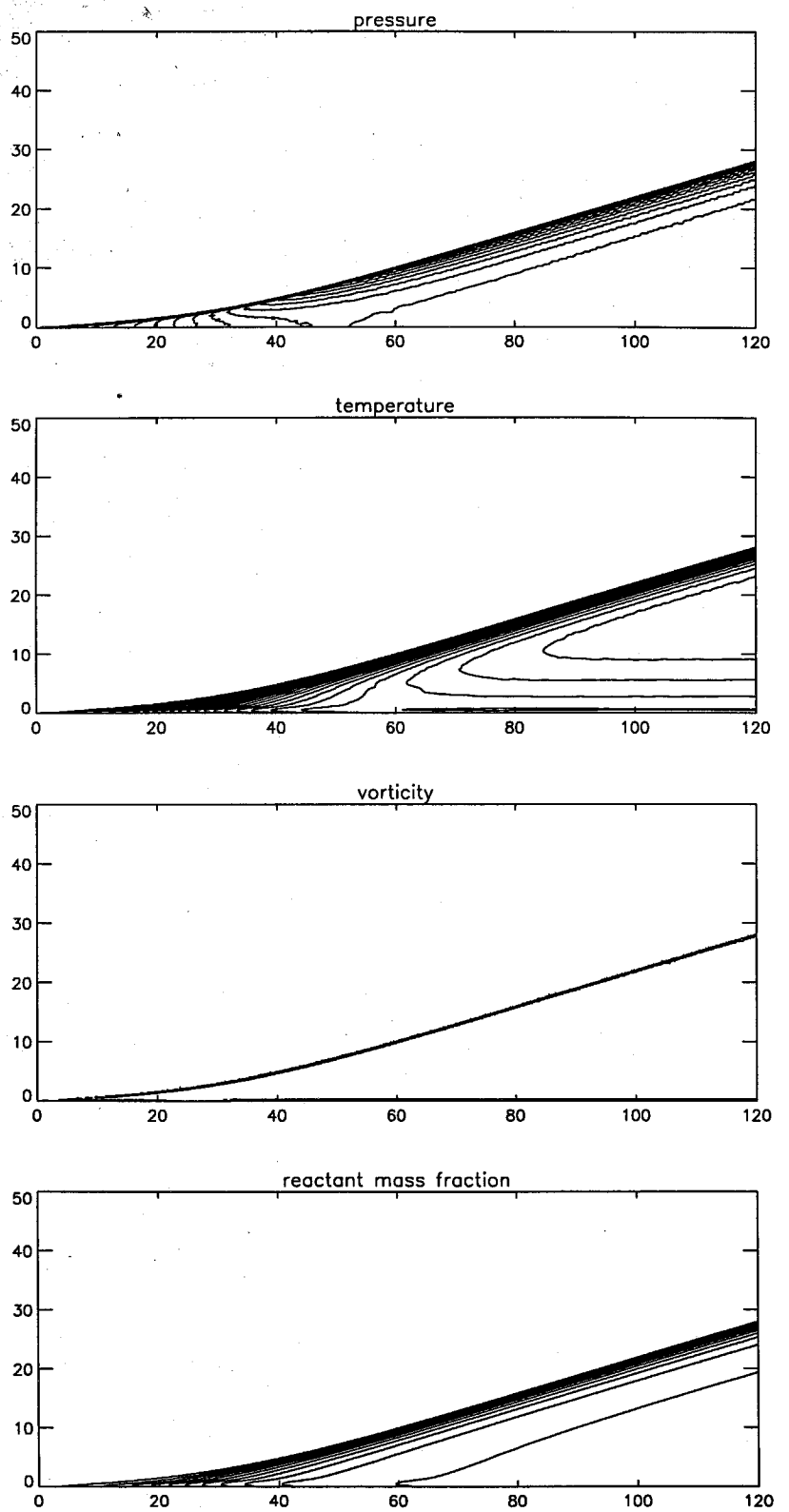

FIG.4.17a Case A, $\theta = 20°$: contour plots of the flow variables at $t = 24.0$.

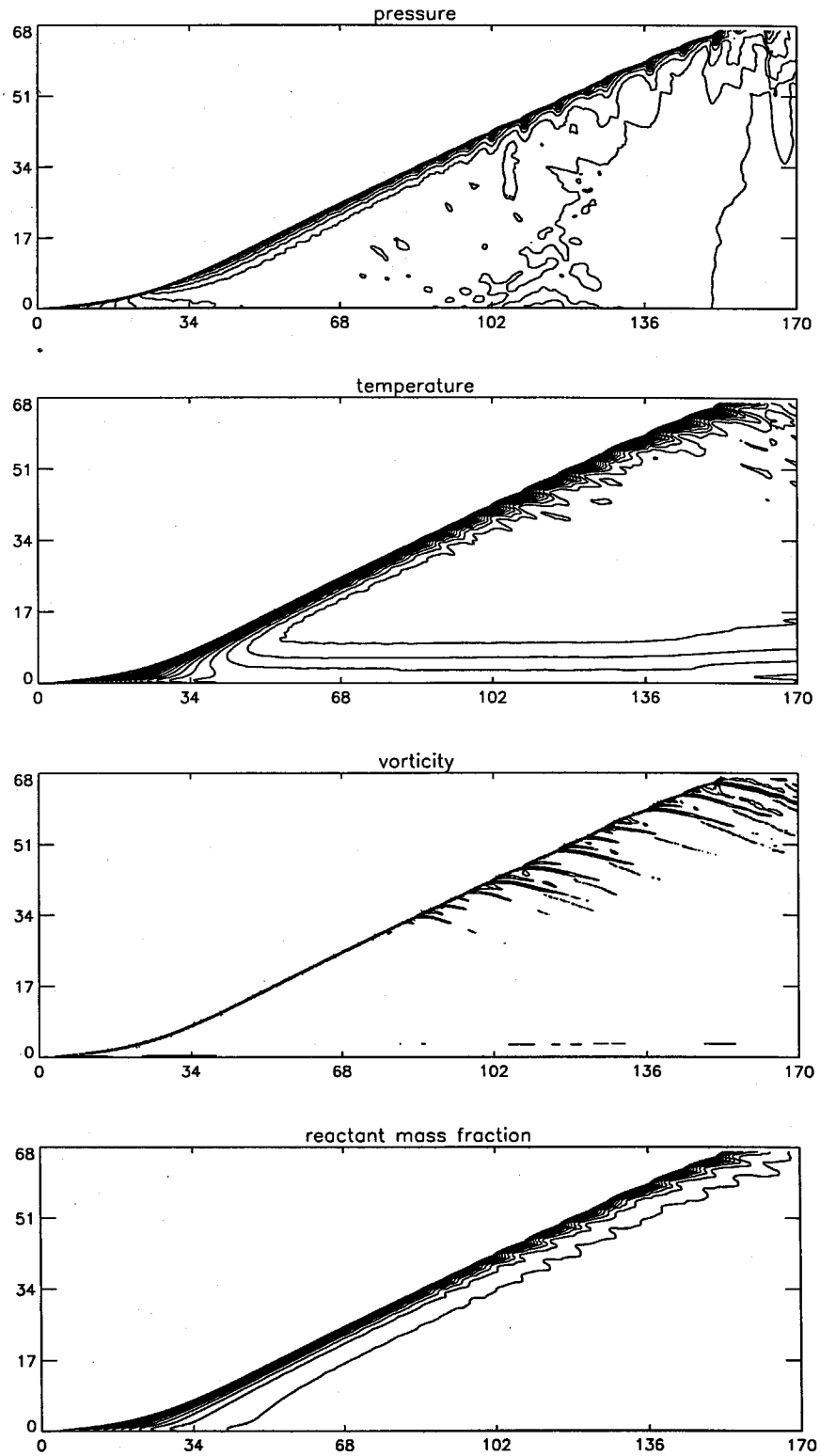

FIG.4.17b Case A, $\theta = 27°$: contour plots of the flow variables at $t = 50.0$.

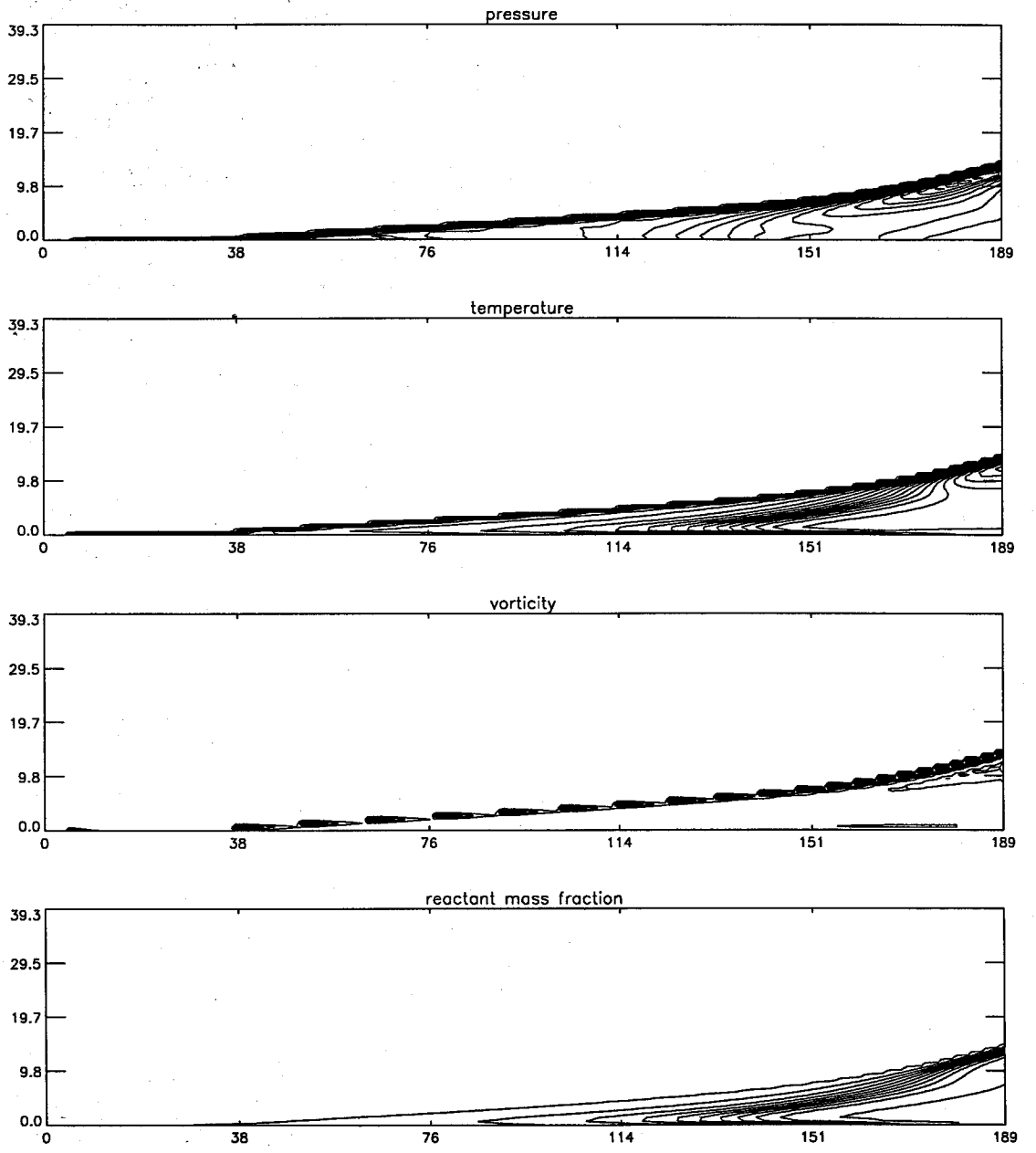

FIG.4.18a Case B, $\theta = 20°$: contour plots of the flow variables at $t = 18.0$. Resolution, 285×60 cells.

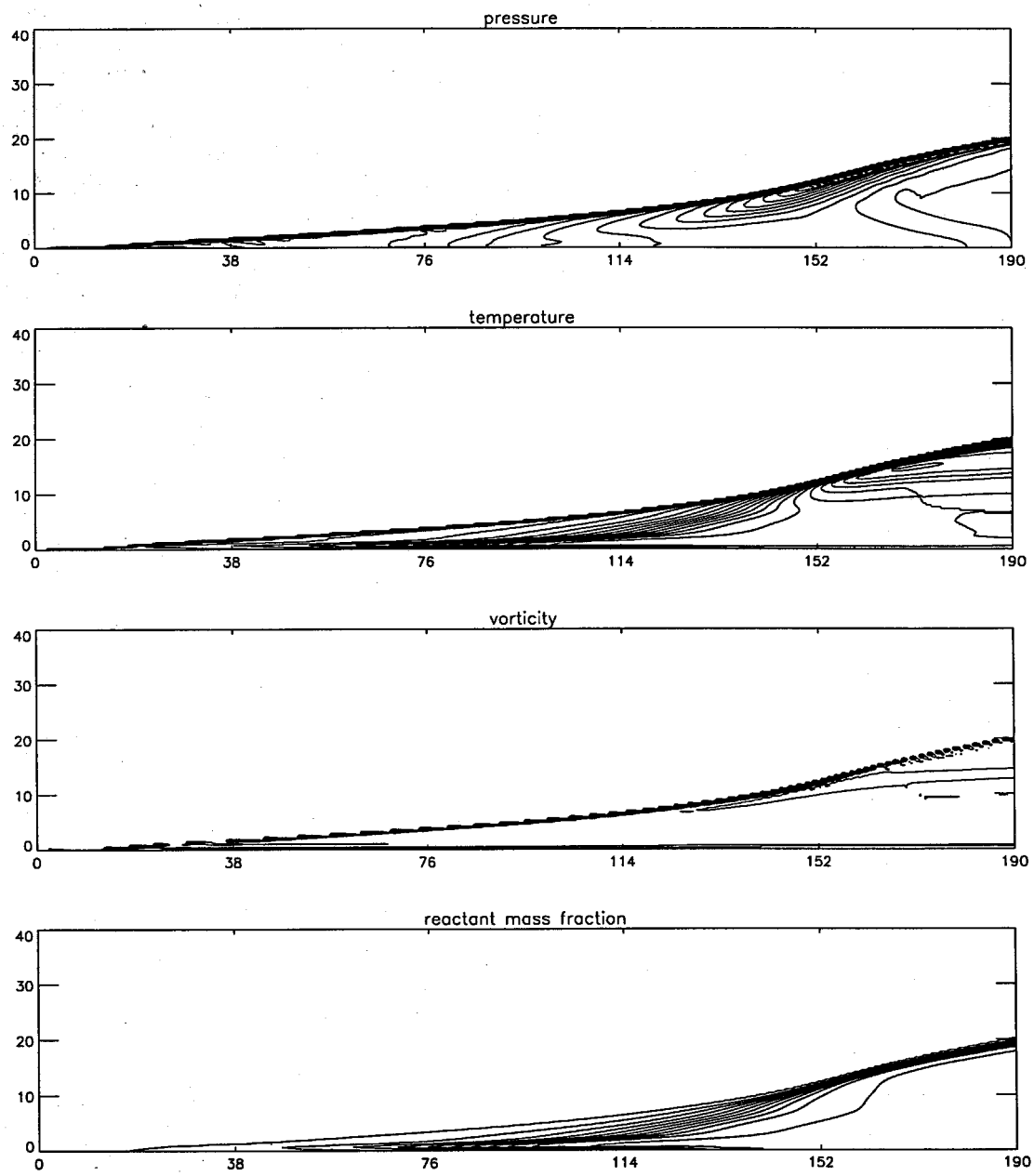

FIG.4.18b Case B, $\theta = 20°$: contour plots of the flow variables at $t = 18.0$. Resolution, 570×120 cells.

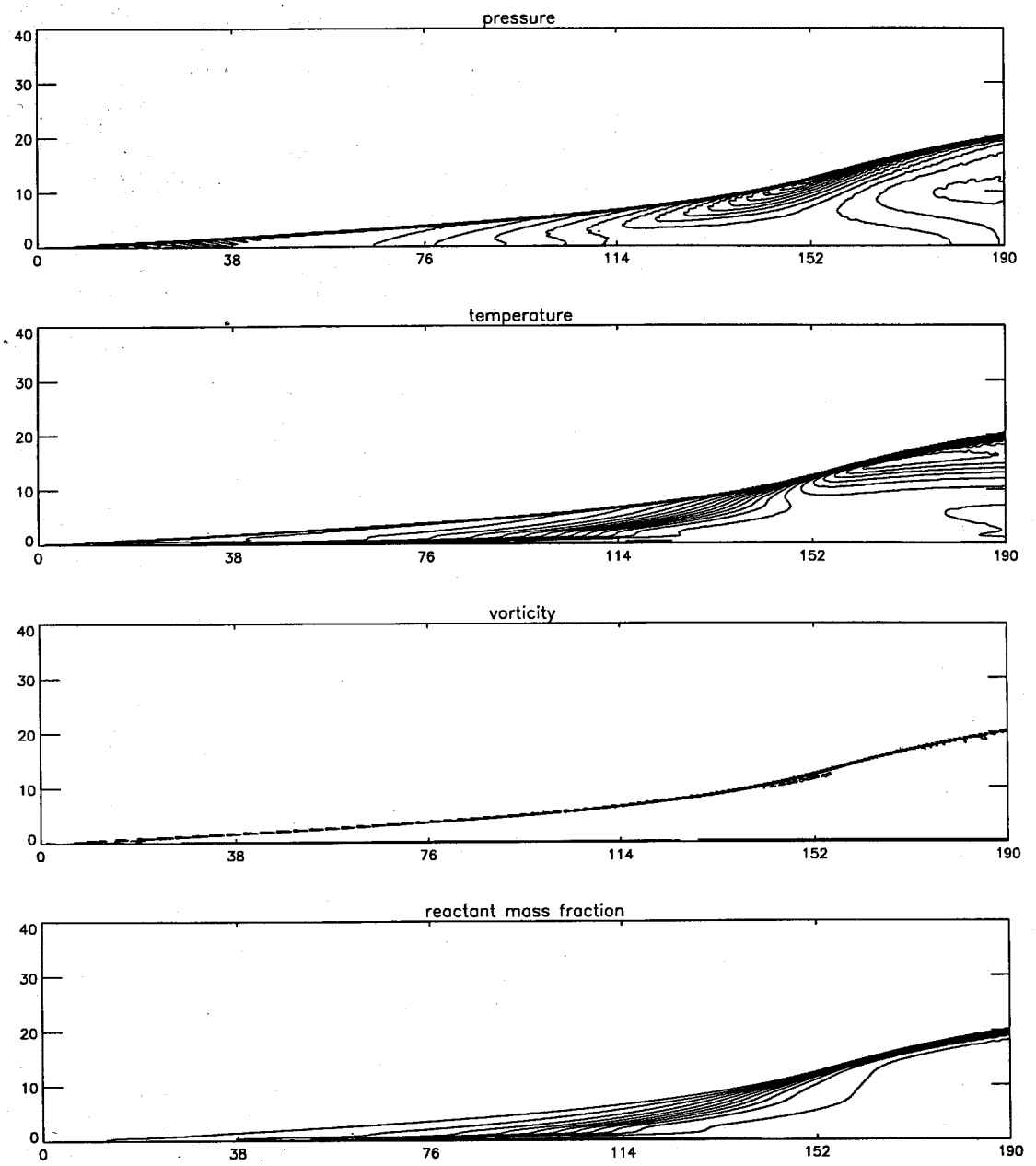

FIG.4.18c Case B, $\theta = 20°$: contour plots of the flow variables at $t = 18.0$. Resolution: 1140×240 cells.

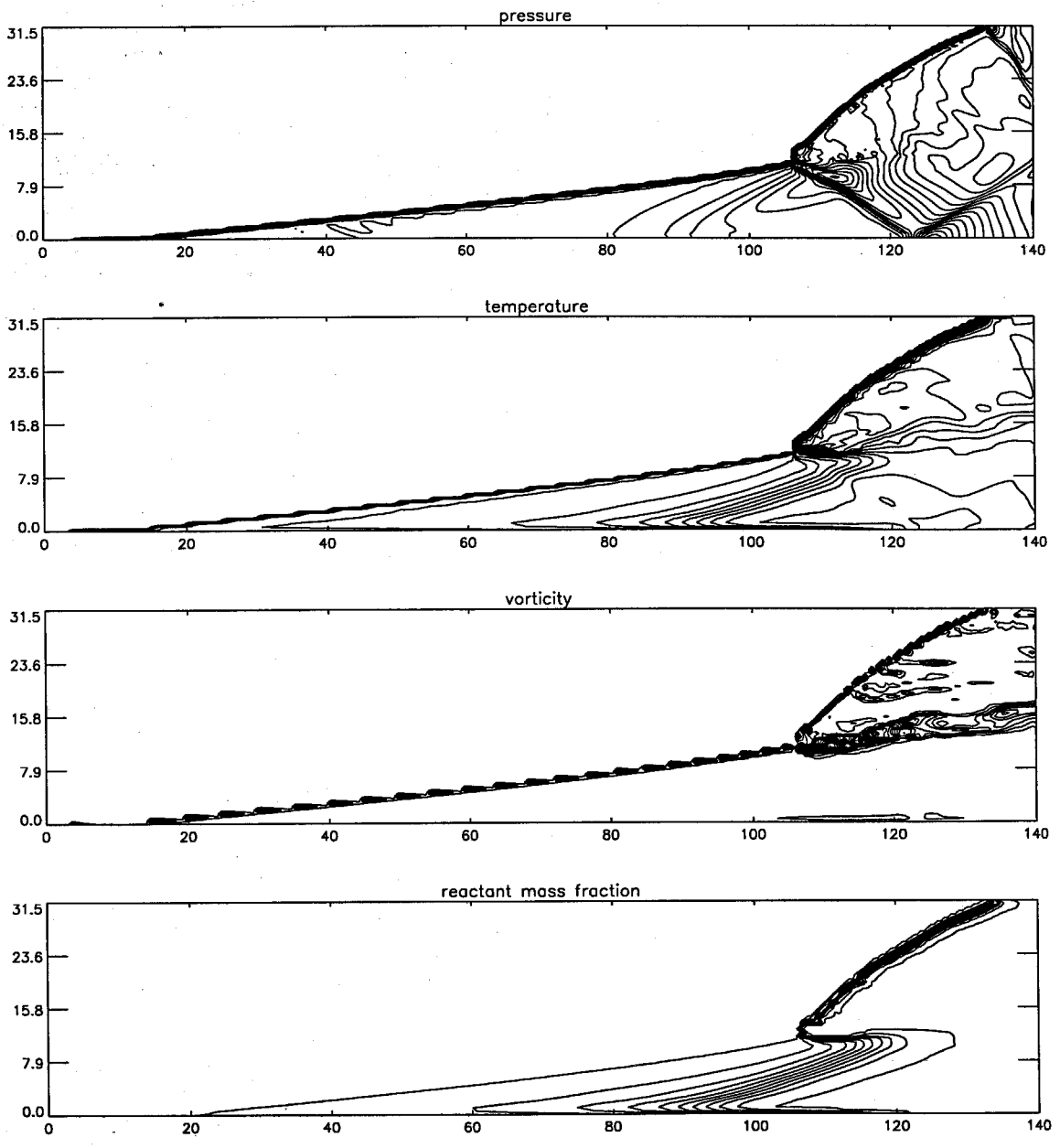

FIG.4.18d Case B, $\theta = 35°$: contour plots of the flow variables at $t = 50.0$. Resolution, 280×64 cells.

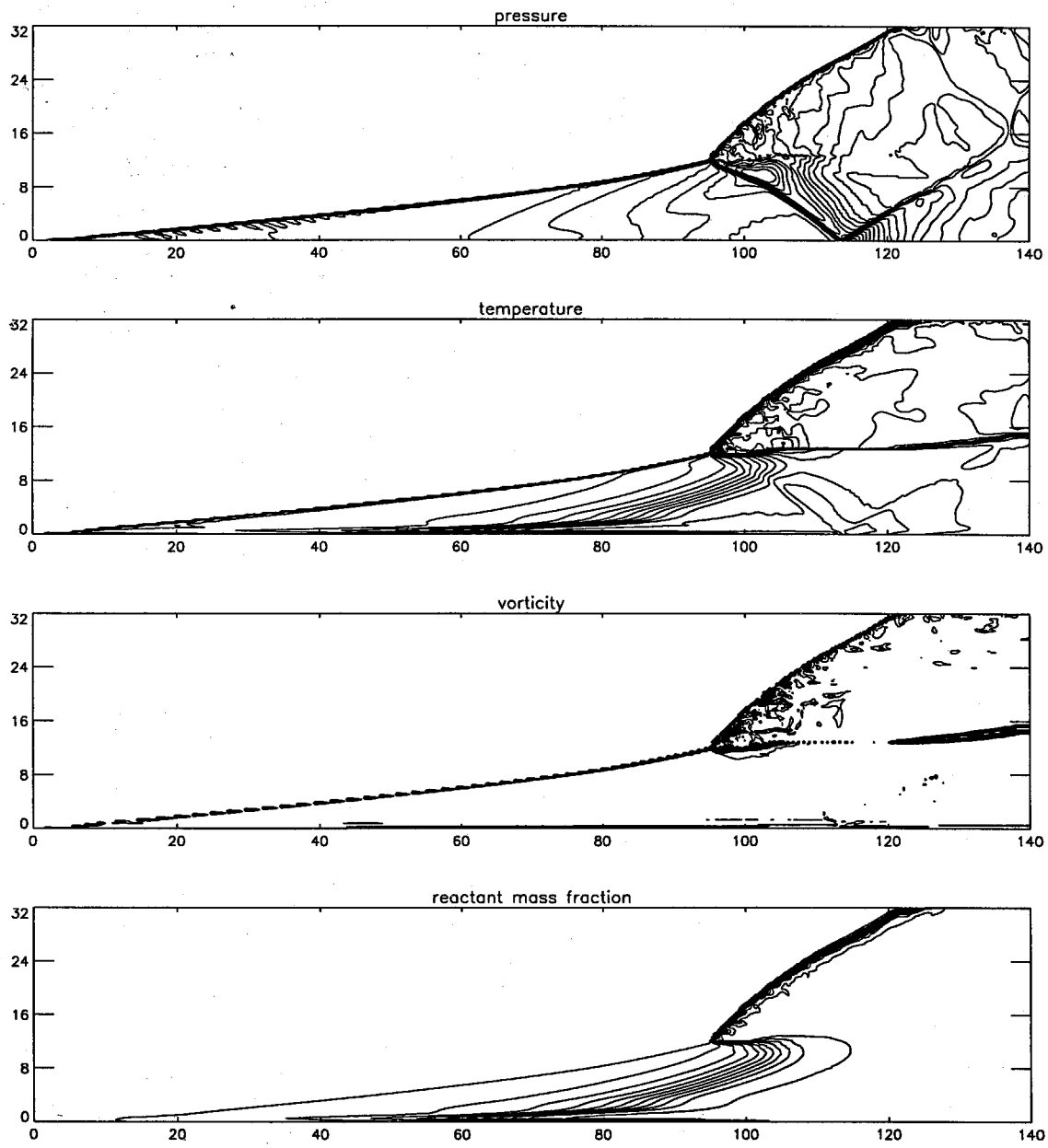

FIG.4.18e Case B, $\theta = 35°$: contour plots of the flow variables at $t = 50.0$. Resolution, 560×128 cells.

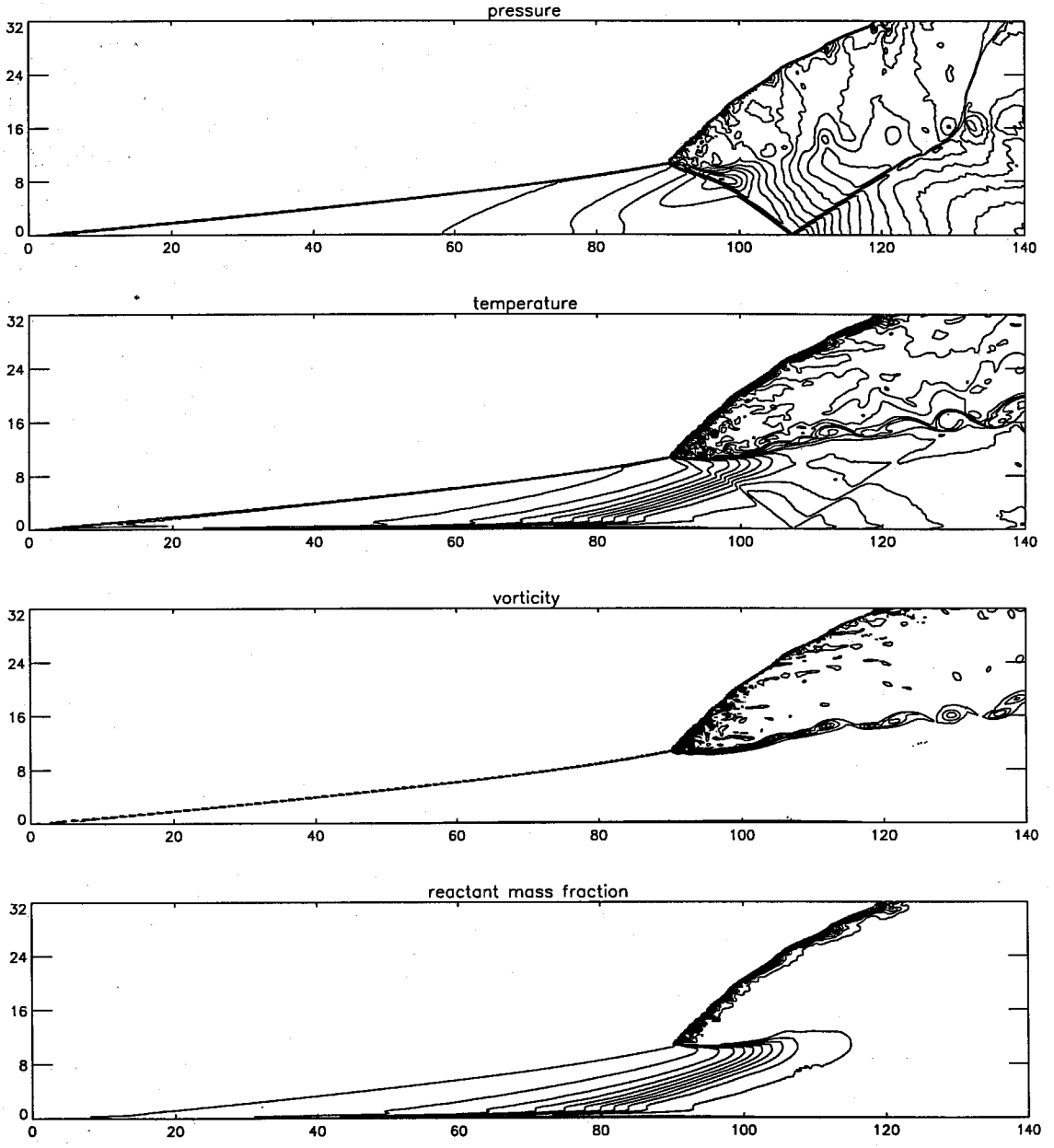

FIG.4.18f Case B, $\theta = 35°$: contour plots of the flow variables at $t = 50.0$. Resolution, 1120×256 cells.

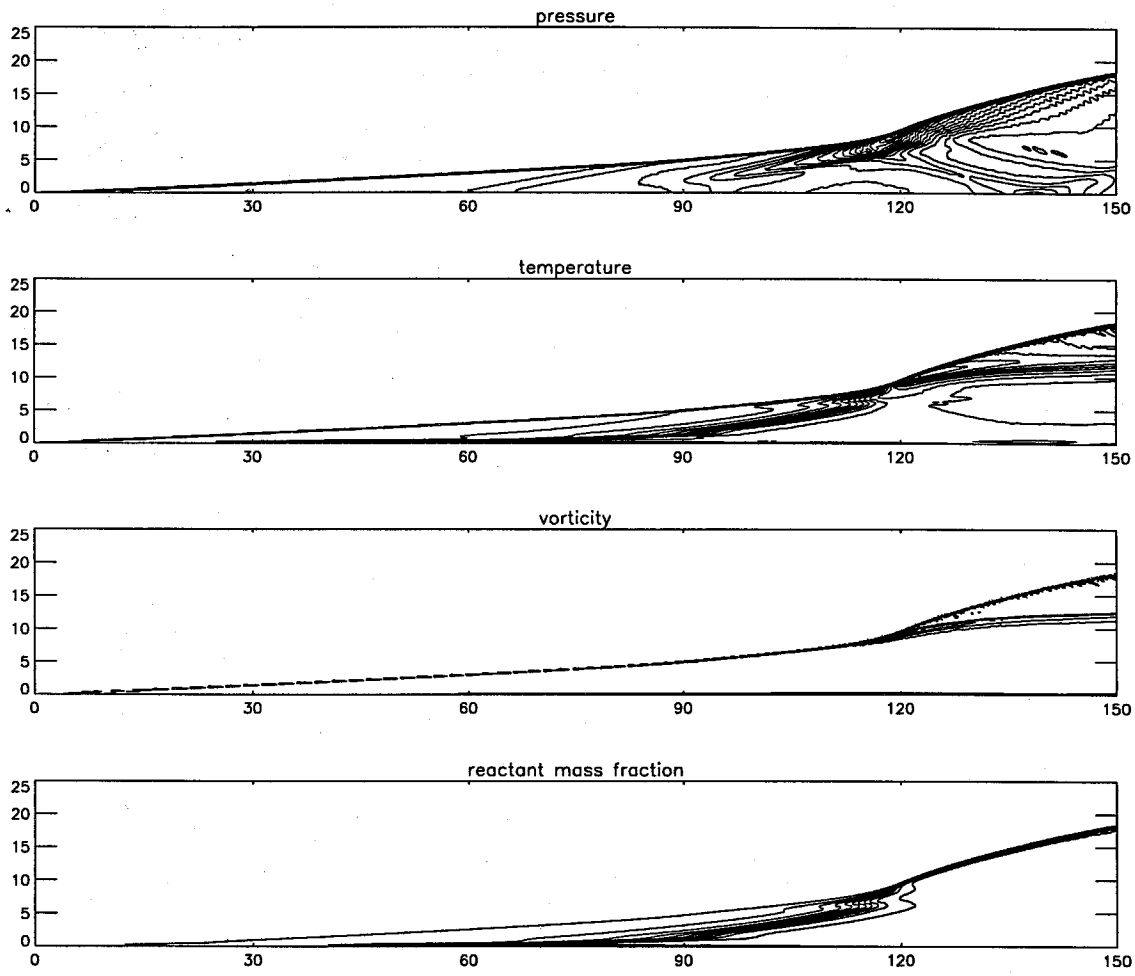

FIG.4.19a Case C, $\theta = 20°$: contour plots of the flow variables at $t = 18.0$.

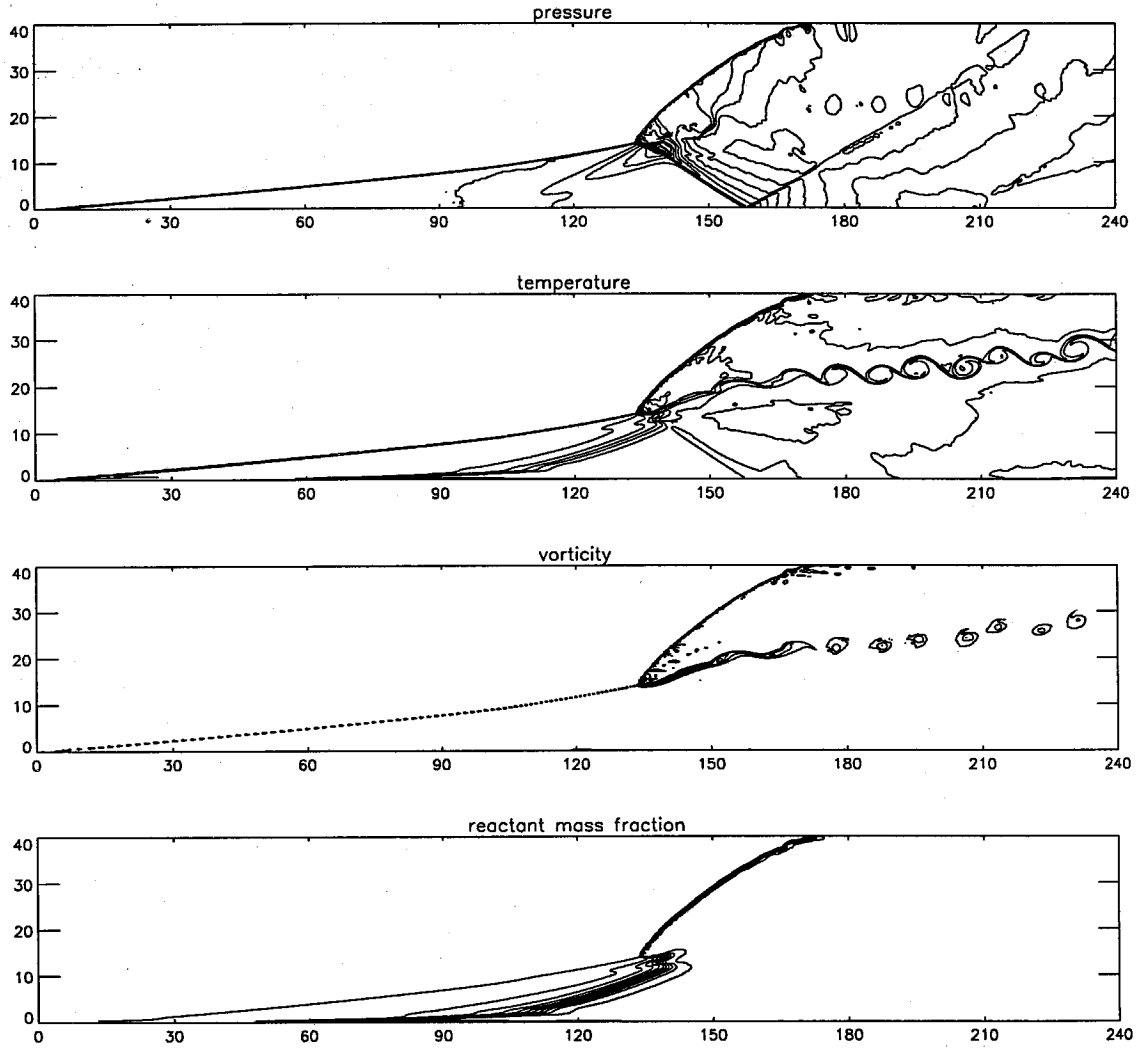

FIG.4.19b Case C, $\theta = 35°$: contour plots of the flow variables at $t = 36.0$.

4.4.2 Detonations induced by short wedges

In the cases examined in the previous subsection, it was assumed that the wedge is long enough for the explosion to take place upstream of the corner of the wedge. In such cases, the location of the explosion and the flow-field in that neighborhood are determined completely by the kinetics of the reaction. If, however, the wedge is not long enough, then the explosion will take place near the corner. The effect of the corner in such situations has also been studied numerically, and the results are described below.

The chemical reaction increases the temperature of the fluid, while the expansion at the corner decreases it. These two mechanisms "compete" against each other. Furthermore, by including the corner in the computational domain, a second characteristic length is introduced. This is the height of the wedge, $h_{\rm w}$, the first one being the half-reaction length. It is the combination of these two length-scales with the wedge angle that ultimately determines which of the two mechanisms will dominate.

In the numerical simulations, the activation energy and the stiffness coefficient are set at $E_{\rm a} = 50$ and $K = 99.762$, respectively. The wedge angle is $\theta = 35°$. The upstream state of the fluid is

$$p_1 = 1.0 \ , \qquad \rho_1 = 1.0 \ , \qquad u_1 = 11.509 \ .$$

The flow that is produced by these parameters and upstream conditions in the case of a long wedge was examined in the previous subsection; see Fig. 4.18d.

Three different wedge heights are considered. First, the wedge height is set at $h_{\rm w} = 70.0$. The computational domain consists of 930×330 cells. The length of the domain is 155.0, and its width from the upper wall of the wedge is 55.0. Results for this simulation, taken at $t = 46.0$, are shown in Fig. 4.20a. In this case the explosion occurs upstream with respect to the corner. The expansion at the corner does not affect the explosion because the flow in the corner is supersonic. The leading shock is expected to reduce far downstream to a CJ wave, just like the one-dimensional detonation initiated by a moving piston that comes suddenly to a rest.

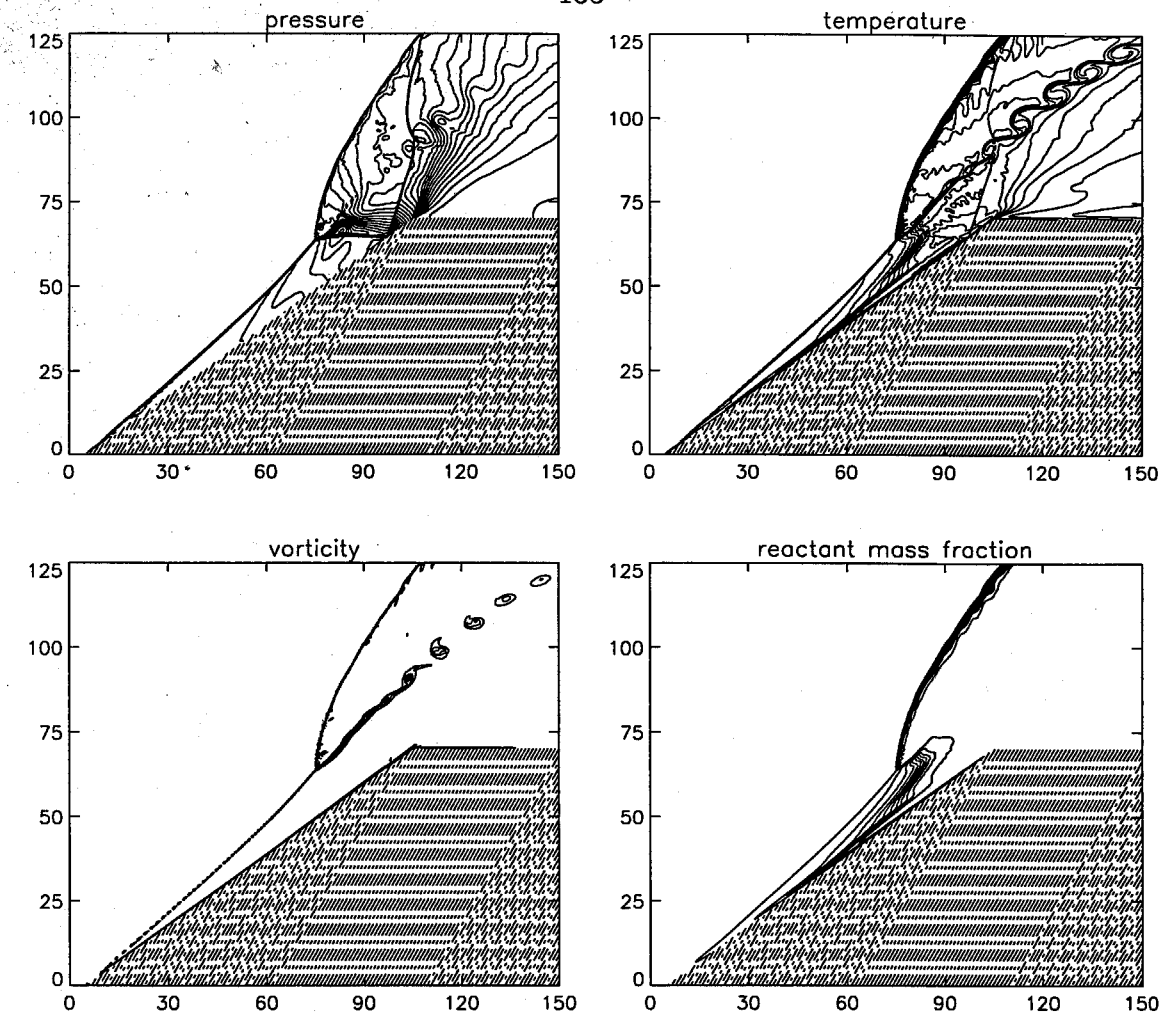

FIG.4.20a Flow past a wedge of height $h_w = 70.0$ and angle $\theta = 35°$. Contour plots of the flow variables at $t = 46.0$.

The flow-field in the neighborhood of the inert shock and the explosion is the same as in the corresponding case with a long wedge; see Fig. 4.18b. The interaction of the reflected shock with the shear layer causes the fluid to decelerate, thus forming another subsonic region in the flow-field, besides the one in the vicinity of the triple point. It is also worth mentioning that the expansion that takes place at the corner affects the evolution of the shear layer. As the fluid below the shear layer expands, the pressure and density drop, generating even higher entropy gradients across the layer. Therefore, the expansion at the corner leads to an increased amount of vorticity generation across the shear layer.

Subsequently, the wedge height is reduced to $h_w = 50.0$. The computational domain consists of 810 × 420 cells. The length of the domain is 135.0, and its width, as measured from the upper wall of the wedge, is 70.0. Results for this

simulation are shown in Fig. 4.20b. They are taken at time $t = 46.0$. In this case, the explosion takes place downstream of the corner. The flow in the subsonic area in the vicinity the triple point (between the Mach stem and the shear layer) is influenced by the expansion at the corner. Additionally, the expansion at the corner affects the curvature of the leading front and the reflected shock.

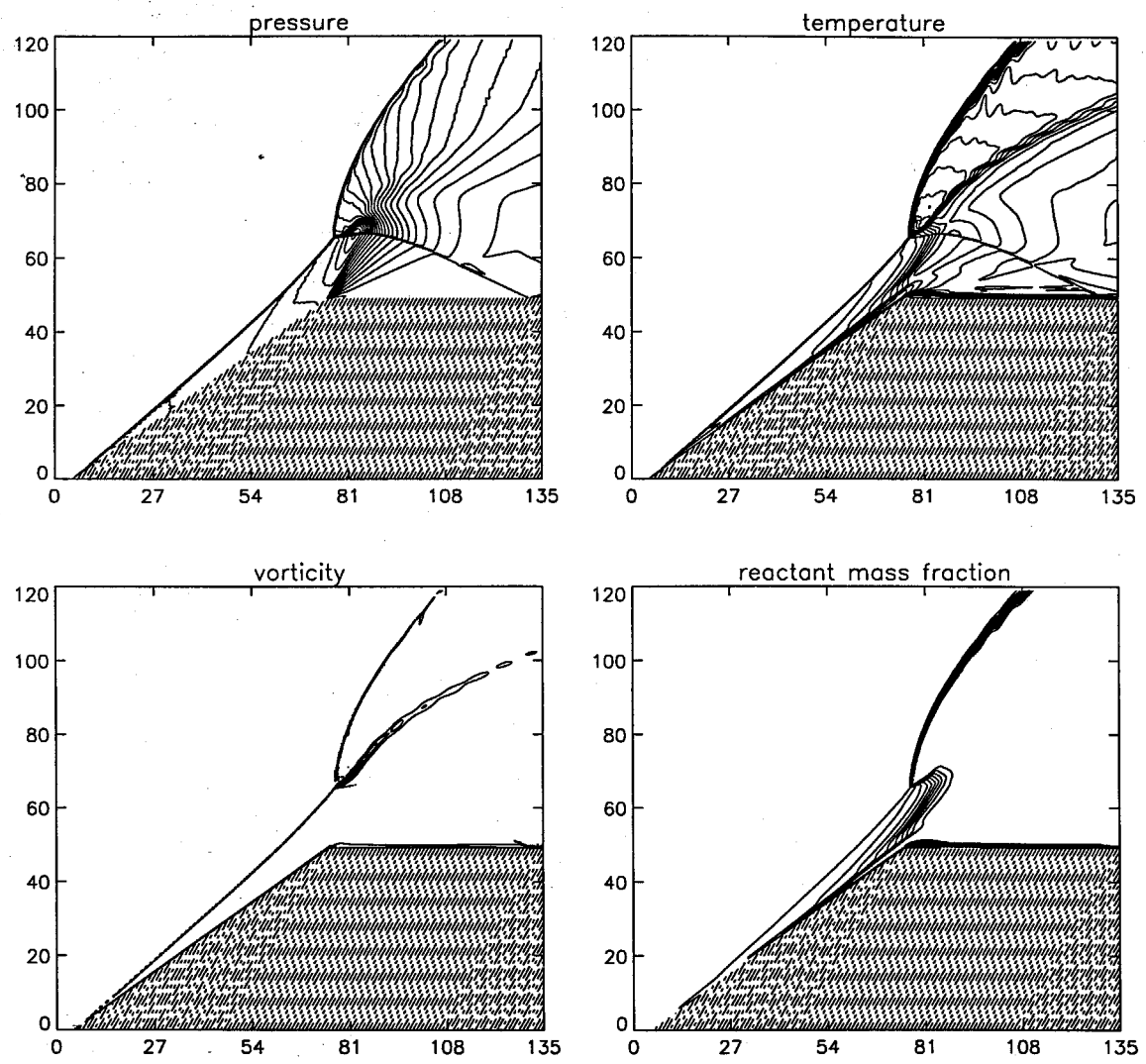

FIG.4.20b Flow past a wedge of height $h_w = 50.0$ and angle $\theta = 35°$. Contour plots of the flow variables at $t = 46.0$.

A fluid element moving parallel to the wedge does not have time to increase its temperature substantially, via the thermal-runaway mechanism, because of the small length of the wedge. Consequently, it remains almost unreacted when it reaches the head of the expansion. The expansion produces a further decrease of

the temperature which delays the initiation of the reaction even more. It is observed that the material on the upper wall of the wedge has remained only partially reacted (about 20%), as a result of the temperature decrease caused by the expansion at the corner.

As a final test, the wedge height is lowered further to $h_w = 25.0$. The simulation is performed on a domain of 1266×270 cells. The length of the domain is 210.0 and its width is 45.0. Results from this simulation, taken at $t = 10.0$, are presented in Fig. 4.20c. It is observed that the expansion at the corner reduces the temperature so much that the gas near the wedge remains almost unreacted because the time needed for rapid reaction via thermal runaway becomes very large. As a result, a detonation can not be established and the shock wave is expected to reduce to a Mach wave downstream. It is also observed that there is a small pocket of slightly reacted material near the wedge. It can be verified by looking at results taken at early times that the formation of this pocket is a transient phenomenon caused by the interaction of the shock wave and the expansion at the corner, in the beginning of the simulation. It is convected downstream with the fluid velocity. The minimum value of the reactant mass fraction inside the pocket is $z \simeq 0.9$. If the material reacted completely, pressure waves would be transmitted to the shock wave and a CJ detonation could be established. But it is observed that the reaction rate, $\dot{z} = -Kz \exp(-E_a/T)$, inside the pocket decays with time, which suggests that the reaction process will not be completed inside the pocket. After some time the pocket exits the computational domain, and the shock front eventually assumes a fixed position. No change in the flow variables can be observed after that. The material all along the wedge will remain only partially reacted, and a detonation will not be established.

4.5 Concluding Remarks

The proposed unsplit numerical scheme has been used for the numerical stufy of two-dimensional detonating flows. The scheme is based on a decomposition of the governing equations that is mathematically consistent, and appears to be capable of capturing important details of the structure of the resulting flow-fields, some of which have not been easy to document in the past. No explicit artificial viscosity mechanisms or any other of the usual "fixes" (such as entropy-fixes or flux-splitting) has been employed.

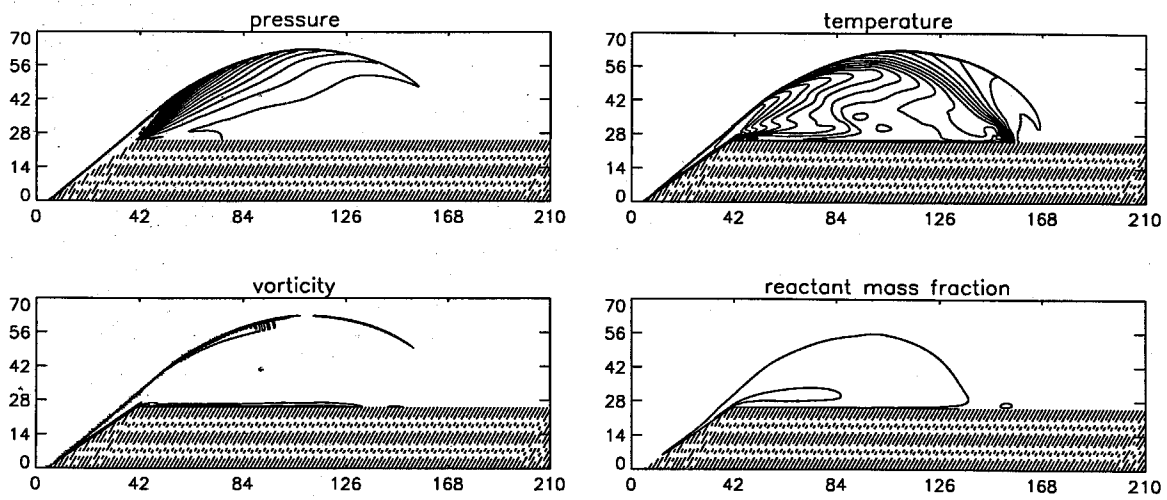

FIG.4.20c Flow past a wedge of height $h_w = 25.0$ and angle $\theta = 35°$. Contour plots of the flow variables at $t = 10.0$.

It was verified that two-dimensional detonations propagating in narrow channels are intrinsically unstable and exhibit chaotic behavior. They are characterized by the presence of cellular patterns. These patterns are formed by the transverse waves of the triple points of the main front. The slip lines emanating from the triple points are rolled-up vortex sheets. They detach from the leading shock when triple-point collisions occur. Vortical structures are also generated by the curvature of the shock but their strength reduces substantially within the chemical reaction zone.

Furthermore, a numerical study of shock-wedge induced detonations was also performed. It was demonstrated that, for small wedge angles, the shock that is attached to the wedge turns smoothly to an oblique ZND wave. For high wedge angles, however, such a smooth turn is not possible and an explosion takes place at the front. The center of the explosion is a stationary triple point. A shear layer emanates from the triple point. that eventually becomes unstable. The effect of the corner of the wedge was also studied numerically. It was shown that when the explosion of the leading front takes place upstream of the corner, the expansion at the corner does not affect the evolution of the front, which reduces to a CJ wave. When the explosion occurs downstream of the corner, the curvature of the front and the reaction process depend on the expansion at the corner. It appears that for wedge heights small enough, a detonation can not be established downstream, and the front decays downstream to a Mach wave.

CHAPTER 5

Future Directions

The subject of this work has been the design and implementation of unsplit schemes for the numerical solution of hyperbolic systems of conservation laws with source terms. For this purpose, new manifolds are defined in space-time, along which the conservation laws can be decomposed into the same characteristic ODE's as in the homogeneous one-dimensional case and solved numerically. These manifolds might be space-like, or time-like, depending on the local spatial gradients of the flow, but embed the curves along which the one-dimensional characteristic equations apply (exactly).

A particular version of the proposed algorithm has been applied successfully to the simulation of one-dimensional detonations and to the simulation of two-dimensional detonations propagating in narrow channels. It has also been employed for the numerical study of wedge-induced detonations. This scheme integrates all the terms of the governing equations simultaneously. No flux-splitting or other usual "fixes" are employed. Most important, no explicit artificial viscosity terms are needed for the stabilization of discontinuities, in contrast with conventional schemes.

Future directions include the extension of the algorithm for the numerical simulation of multi-component reacting systems. This will help study various problems arising in supersonic combustion, such as the effect of chain-branching. The better understanding of these mechanisms is very crucial to the design of the next-generation, high-speed propulsion systems. In order to treat with the considerable resolution requirement that are necessary in order to capture instabilities of very short wavelength, the proposed algorithms will be parallelized so that they can work in the environment of massively parallel supercomputers.

Additionally, the decomposition of the two-dimensional hyperbolic system that was described in Chapter 3 of the present work can be directly extended to hyperbolic systems in three space dimensions. This development will serve as the building block for the generalization of the algorithm to three-dimensional, chemically-reacting flows. It should be stressed that because such flows are highly non-linear phenomena, the third spatial dimension is expected to result in a richer dynamical behavior, with many more unstable modes than in the two-dimensional case. It is apparent, therefore, that three-dimensional simulations are necessary in order to get useful information about the initiation and propagation of instabilities and combustion fronts in these flows.

References

ABOUSEIF, G., AND TOONG, T.Y. [1982], "Theory of unstable one-dimensional detonations," *Combust. Flame*, Vol. **45**, pp. 67-94.

BARTHEL, H.O. [1972], "Reaction zone-shock front coupling in detonations," *Phys. Fluids*, Vol. **15**, pp. 43-50.

BARTHEL, H.O. [1974], "Predicted spacings in hydrogen-oxygen-argon detonations," *Phys. Fluids*, Vol. **17**, pp. 1547-1553.

BARTHEL, H.O., AND STREHLOW, R.A. [1966], "Wave propagation in 1-D reactive flows," *Phys. Fluids*, Vol. **9**, pp. 1896-1907.

BARTLMA, F. [1990], "The propagation of detonation waves in channels of varying cross section," *J. Fl. Mech.*, Vol. **218**, pp. 225-238.

BAZENHOVA, T.V., GVODZEVA, L.G., AND NETTLETON, M.G. [1984], "Unsteady interactions of shock waves," *Prog. Aerosp. Sci.*, Vol. **21**, pp. 249-331.

BDZIL, J.B., AND STEWART, D.S. [1989], "Modeling two-dimensional detonations with detonation shock dynamics," *Phys. Fluids, A*, Vol. **1**, pp. 1261-1267.

BEN-ARTZI, M. [1989] "The generalized Riemann problem for reactive flows," *J. Comp. Phys.*, Vol. **81**, pp. 70-101.

BEN-ARTZI, M., AND FALCOVITZ, J. [1986], "An upwind second-order scheme for compressible duct flows," *SIAM J. Sci. Stat. Comp.*, Vol. **7**, pp. 744-768.

BOURLIOUX, A. [1991], *Numerical Study of Unstable Detonations*, Ph.D. Thesis, Princeton University.

BOURLIOUX, A., AND MAJDA, A.J., AND ROYTBURD, V. [1991], "Theoretical and numerical structure for unstable one-dimensional detonations," *SIAM J. Appl. Math.*, Vol. **51**, pp. 303-343.

BOURLIOUX, A., AND MAJDA, A.J. [1992], "Theoretical and numerical structure for unstable two-dimensional detonations," *Combust. Flame*, Vol. **90**, pp. 211-229.

BUCKMASTER, J.D. [1992], "The structural stability of an oblique detonation wave," *Combust. Sci. Tech.*, Vol. **72**, pp. 283-296.

BUKIET, B.G., AND MENIKOFF R. [1992], "Detonations waves and the front tracking method," *Phys. Fluids, A*, Vol. **4**, pp. 2070-2081.

CAI, W. [1995], "High-order hybrid numerical simulations of two-dimensional detonation waves," *AIAA Journal*, Vol. **33**, pp. 1248-1255.

CAMBIER, J.L., ADELMAN, H., AND MENEES, G.P. [1989], "Numerical simulations of oblique detonations in supersonic combustion chambers," *AIAA J. Propul. Power*, Vol. **5**, pp. 483-491.

CHALABI, A. [1992], "Stable upwind schemes for hyperbolic conservation laws with source terms," *IMA J. Num. Anal.*, Vol. **12**, pp. 217-241.

CHEN, G., LEVERMORE, C., AND LIU, T.P. [1994] "Hyperbolic conservation laws with stiff relaxation terms and entropy," *Comm. Pure Appl. Math.*, Vol. **47**, pp. 787-830.

CHOI, Y.S., AND MAJDA, A.J. [1989], "Amplification of small-amplitude high-frequency waves in a reactive mixture," *SIAM Review*, Vol. **31**, pp. 401-427.

COLELLA, P., MAJDA, A.J., AND ROYTBURD, V. [1986], "Theoretical and numerical structure of reacting shock waves," *SIAM J. Sci. Stat. Comp.*, Vol. **7**, pp. 1059-1080.

COLELLA, P., AND WOODWARD P.R. [1984], "The PPM method for gas dynamic simulations," *J. Comp. Phys.*, Vol. **54**, pp. 174-201.

COURANT, R., AND HILBERT., D. [1963] *Methods of Mathematical Physics, Vol. II*, Wiley Interscience, New York.

CRANDALL, M.G., AND MAJDA, A.J. [1980], "Monotone difference approximations for scalar conservation laws," *Math. Comp.*, Vol. **34**, pp. 1-21.

DI PERNA, R.J., AND MAJDA A.J. [1985], "The validity of nonlinear geometric optics for weak solutions of conservation laws," *Comm. Math. Phys.*, Vol. **98**, pp. 313-347.

DOERING, W. [1943], "On detonation processes in gases," *Ann. Phys.*, Vol. **43**, pp. 421-436.

ENGQUIST, B., AND SJOGREEN, B. [1991], "Robust difference approximations of stiff inviscid detonation waves," *UCLA-CAM Report 91-03.*

ERPENBECK, J.J. [1964], "Stability of idealized one-reaction detonations," *Phys. Fluids*, Vol. **7**, pp. 684-696.

ERPENBECK, J.J. [1970], "Non-linear theory of unstable two-dimensional detonation," *Phys. Fluids*, Vol. **13**, pp. 2007-2026.

FICKETT, W., AND DAVIS, W.C. [1979], *Detonation*, U.C. Berkeley Press.

FICKETT, W., AND WOOD, W.W. [1966], "Flow calculation for pulsating one-dimensional detonation," *Phys. Fluids*, Vol. **9**, pp. 903-916.

GLENN, D.E., AND PRATT, D.T. [1988], "Numerical modeling of standing oblique detonation waves," *AIAA paper 88-0440.*

GLIMM, J., MARSHALL, G., AND PLOHR, B. [1984], "A generalized Riemann problem for quasi-one-dimensional gas flows," *Adv. Appl. Math.*, Vol. **5**, pp. 1-30.

GRIFFITHS, D.F., STUART, A.M., AND YEE, H.C. [1992], "Numerical wave propagation in an advection equation with a nonlinear source term," *SIAM J. Num. Anal.*, Vol. **29**, pp. 1244-1260.

GRISMER, M.J. [1994], *Numerical Simulations of Steady and Unsteady Oblique Detonation Phenomena with Application to Combustion*, Ph.D. Thesis, University of Notre Dame.

HARTEN, A., ENGQUIST, B., OSHER, S., AND CHAKRAVARTHY, S. [1987], "Uniformly high order accurate ENO schemes. III," *J. Comp. Phys.*, Vol. **71**, pp. 231-303.

HE, L.T., AND LEE, J.H.S. [1995], "The dynamical limit of one-dimensional detonations," *Phys. Fluids*, Vol. **7**, No. **5**, pp. 1151-1159.

KAPILA, A.K., MATKOWSKY, B.J., AND VAN HARTEN A. [1983], "An asymptotic theory of deflagrations and detonations. I. The steady solutions,"*SIAM J. Appl. Math.*, Vol. **43**, pp. 491-519.

KLEIN, R., AND MENIKOFF R. [1993], "The relation between curvature, rate state-dependence, and detonation velocity,"*SIAM J. Appl. Math.*, Vol. **53**, pp. 1401-1435.

KRUZKOV, S.N. [1970], "First order quasilinear equations in several dependent variables," *Math. Sbornik*, Vol. **123**, pp. 217-243.

LAPPAS, T., LEONARD, A., AND DIMOTAKIS, P.E. [1993], "An adaptive lagrangian method for computing 1-D reacting and non-reacting flows," *J. Comp. Phys.*, Vol. **104**, pp. 361-376.

LAPPAS, T., LEONARD, A., AND DIMOTAKIS, P.E. [1995], "Riemann invariant manifolds for the multidimensional Euler equations," under review by the *SIAM J. Sci. Comp.*

LAX, P. [1973], *Hyperbolic Systems of Conservation Laws and the Mathematical Theory of Shock Waves*, SIAM.

LAX, P. [1957], "Hyperbolic systems of Conservation laws II," *Comm. Pure Appl. Math.*, Vol. **10**, pp. 537-566.

LEE, H.I., AND STEWART, D.S. [1990], "Calculation of linear detonation instability: one-dimensional instability of plane detonation," *J. Fl. Mech.*, Vol. **206**, pp. 103-132.

LEFEBVRE, M.H., ORAN, E.S., KAILASANATH, K., AND VAN TIGGELEN, P.J. [1993], "Simulation of cellular structure in a detonation wave," *Prog. Aeronaut. Astronaut.*, Vol. **153**, pp. 64-77.

LE VEQUE, R.J. [1992], *Numerical Methods for Conservation Laws*, Birkhauser Verlag, Zurich.

LE VEQUE, R.J., AND SHYUE, K.M. [1995], "One-dimensional front tracking based on high resolution wave propagation mathods," *SIAM J. Sci. Comp.*, Vol. **16**, pp. 348-377.

LE VEQUE, R.J., AND YEE, H.C. [1990], "A study of numerical methods for hyperbolic conservation laws with stiff source terms," *J. Comp. Phys.*, Vol. **86**, pp. 187-209.

LI, C., KAILASANATH, K., AND ORAN, E.S. [1994], "Detonation structures behind oblique shocks," *Phys. Fluids*, Vol. **6**, pp. 1600-1611.

LIONS, P.L., AND SOUGANIDIS, P.E. [1995], "Convergence of MUSCL and filtered schemes for scalar conservation laws and Hamilton-Jacobi equations," *Math. Comp.*, Vol. **69**, pp. 441-470.

LIU, T.P. [1979], "Quasilinear hyperbolic systems," *Comm. Math. Phys.*, Vol. **68**, pp. 141-172.

LIU, T.P. [1987], "Hyperbolic conservation laws with relaxation," *Comm. Math. Phys.*, Vol. **108**, pp. 153-175.

MAJDA A.J. [1987], "Criteria for regular spacing of reacting Mach stems," *Proc. Natl. Acad. Sci. U.S.A.*, Vol. **84**, pp. 6011-6014.

MAJDA A.J., AND ROSALES R.R. [1984], "Resonantly interacting weakly nonlinear hyperbolic waves. I. A single space variable," *Studies Appl. Math.*, Vol. **71**, pp. 149-179.

MAJDA A.J., AND ROSALES R.R. [1987], "Nonlinear mean field - high frequency wave interactions in the induction zone," *SIAM J. Appl. Math.*, Vol. **47**, pp. 1017-1039.

MAJDA, A.J., AND ROYTBURD, V. [1990], "Numerical study of the mechanisms for initiation of reacting shock waves," *SIAM J. Sci. Stat. Comp.*, Vol. **11**, pp. 950-974.

MENIKOFF R., LACKNER, K.S., AND BUKIET, B.G. [1996], "Modeling flows with curved detonations waves," *Combust. Flame*, Vol. **104**, pp. 219-240.

NICOLIS, G. [1995], *Introduction to Nonlinear Science*, Cambridge University Press.

ORAN, E.S., AND BORIS, J.P. [1987], *Numerical Simulation of Reactive Flow*, Elsevier, New York.

ORAN, E.S., KAILASANATH, K., AND GUIRGUIS, R.H. [1988], "Numerical simulations of the development and structure of detonations," *Prog. Aeronaut. Astronaut.*, Vol. **114**, pp. 155-170.

OSHER, S., AND SETHIAN, J.A. [1988], "Fronts propagating with curvature dependant speed: algorithms based on Hamilton-Jacobi Formulations," *J. Comp. Phys.*, Vol. **79**, pp. 12-49.

PEMBER, R. [1993], "Numerical methods for hyperbolic conservation laws with stiff relaxation. I. spurious solutions," *SIAM J. Appl. Math.*, Vol. **53**, pp. 1293-1330.

PEMBER, R. [1993], "Numerical methods for hyperbolic conservation laws with stiff relaxation. II. higher-order Godunov methods," *SIAM J. Sci. Comp.*, Vol. **14**, pp. 824-859.

POWERS, J.M., AND STEWART, D.S. [1992], "Approximate solutions for oblique detonations in the hypersonic limit," *AIAA Journal*, Vol. **30**, pp. 726-736.

QUIRK, J.J. [1993], "Godunov-type schemes applied to detonation flows," *ICASE report No. 93-15.*

ROE, P.H. [1981], "Approximate Riemann solvers, parameter vectors, and difference schemes," *J. Comp. Phys.*, Vol. **43**, pp. 357-372.

ROE, P.H. [1986], "Characteristic-based schemes for the Euler equations," *Ann. Rev. Fl. Mech.*, Vol. **18**, pp. 337-365.

ROE, P.H. [1986], "Upwind differencing schemes for hyperbolic conservation laws with source terms," *Lecture Notes in Mathematics*, Vol. **1270**, C. Carasso, P. Raviart, D. Serre, editors, Springer Verlag, NY.

SCHOFFEL, S.U., AND EBERT, F. [1988], "Numerical Analyses concerning the spatial dynamics of an initially plane gaseous ZDN detonation," *Prog. Aeronaut. Astronaut.*, Vol. **114**, pp. 32-44.

SETHIAN, J.A. [1990], "Numerical algorithms for propagating interfaces: Hamilton-Jacobi equations and conservation laws," *J. Diff. Geom.*, Vol. **31**, pp. 131-161.

SHEPHERD, J.E. [1994], "Detonation waves and propulsion," *Combustion in high-speed flows* (editor J. Buckmaster *et al.*), pp. 373-420, Kluwer Academic Publishers.

SMOLLER, J. [1983], *Shock Waves and Reaction-Diffusion Equations*, Springer-Verlag, New York.

STEWART, D.S., AND BDZIL, J.B. [1988], "The shock dynamics of stable multidimensional detonation," *Combust. Flame*, Vol. **72**, pp. 311-323.

STRANG, G. [1968], "On the construction and comparison of difference schemes," *SIAM J. Num. Anal.*, Vol. **5**, pp. 506-517.

STREHLOW, R.A. [1970], "Multi-dimensional detonation wave structure," *Astronautica Acta.*, Vol. **15**, pp. 345-357.

STREHLOW, R.A., ADAMCZYK, A.A., AND STILES, R.J. [1972], "Transient studies of detonation waves," *Astronautica Acta.*, Vol. **17**, pp. 509-527.

STREHLOW, R.A., AND FERNANDEZ, F.D. [1972], "Transverse waves in detonations," *Combust. Flame*, Vol. **9**, pp. 109-119.

TANG, T., AND TENG, Z.H. [1995], "Error bounds for fractional step methods for conservation laws with source terms," *SIAM J. Num. Anal.*, Vol. **32**, pp. 110-127.

TAKI, S., AND FUJIWARA, T. [1973], "Numerical analysis of two-dimensional nonsteady detonations," *AIAA Journal*, Vol. **16**, pp. 73-85.

VAN LEER, B. [1977], "Towards the ultimate conservative difference scheme. IV. A new approach to numerical convection," *J. Comp. Phys.*, Vol. **23**, pp. 276-299.

VAN LEER, B. [1979], "Towards the ultimate conservative difference scheme. V. A second order sequel to Godunov's Method," *J. Comp. Phys.*, Vol. **32**, pp. 101-136.

VAN LEER, B. [1984], "On the relation between the upwind-differencing schemes of Godunov, Engquist-Osher and Roe," *SIAM J. Sci. Stat. Comp.*, Vol. **5**, pp. 1-20.

VON NEUMANN, J. [1942], "Theory of detonation waves," *John Von Neumann Collected Works*, Vol. **6**, Macmillan, New York.

WHITHAM, G. [1974], *Linear and Nonlinear Waves*, Wiley Interscience, New York.

WOODWARD P.R., AND COLELLA, P. [1984], "The numerical simulation of two-dimensional fluid flow with strong shocks," *J. Comp. Phys.*, Vol. **54**, pp. 115-173.

YEE, H.C. [1987], *A class of high-resolution explicit and implicit shock-capturing methods*, Von Karman Institute, Belgium.

ZELDOVICH, Y.B. [1960], "On the theory of the propagation of detonation in gaseous systems," (English Translation), *NACA TM 1261.*